MICROSTRUCTURAL ORIGINS OF STRAIN HETEROGENEITY IN FORMABILITY OF ALUMINUM ALLOYS

A THESIS SUBMITTED TO
THE GRADUATE SCHOOL OF NATURAL AND APPLIED SCIENCES
OF
MIDDLE EAST TECHNICAL UNIVERSITY

BY

BARAN GÜLER

IN PARTIAL FULFILLMENT OF THE REQUIREMENTS
FOR
THE DEGREE OF DOCTOR OF PHILOSOPHY
IN
METALLURGICAL AND MATERIALS ENGINEERING

DECEMBER 2019

Approval of the thesis:

MICROSTRUCTURAL ORIGINS OF STRAIN HETEROGENEITY IN FORMABILITY OF ALUMINUM ALLOYS

submitted by **BARAN GÜLER** in partial fulfillment of the requirements for the degree of **Doctor of Philosophy in Metallurgical and Materials Engineering Department, Middle East Technical University** by,

Prof. Dr. Halil Kalıpçılar
Dean, Graduate School of **Natural and Applied Sciences** _____

Prof. Dr. Cemil Hakan Gür
Head of Department, **Met. and Mat. Eng.** _____

Assoc. Prof. Dr. Mert Efe
Supervisor, **Met. and Mat. Eng., METU** _____

_____

Examining Committee Members:

Prof. Dr. Cemil Hakan Gür
Met. and Mat. Eng, METU _____

Assoc. Prof. Dr. Mert Efe
Met. and Mat. Eng., METU _____

Assist. Prof. Dr. Sezer Özerinç
Mechanical Engineering, METU _____

Assoc. Prof. Dr. C. Can Aydıner
Mechanical Engineering, Boğaziçi University _____

Assist. Prof. Dr. Eda Aydoğan Güngör
Integrated Manufacturing Research & Application Center, Sabancı University _____

Date: 27.12.2019

I hereby declare that all information in this document has been obtained and presented in accordance with academic rules and ethical conduct. I also declare that, as required by these rules and conduct, I have fully cited and referenced all material and results that are not original to this work.

Name, Surname: Baran Güler

Signature:

ABSTRACT

MICROSTRUCTURAL ORIGINS OF STRAIN HETEROGENEITY IN FORMABILITY OF ALUMINUM ALLOYS

Güler, Baran
Doctor of Philosophy, Metallurgical and Materials Engineering
Supervisor: Assoc. Prof. Dr. Mert Efe

December 2019, 106 pages

In forming of sheet metals, strain localizations and subsequent necking are generally induced by geometrical imperfections, such as local thickness variations. Microstructural heterogeneities also take role in strain localizations, yet their influence is neglected when concerning the macro-scale formability. This thesis investigated the effects of microstructural features on the strain localization behavior of aluminum alloys. A small-scale biaxial test device and sample were utilized for this purpose. The custom cruciform sample design and the thickness consistency provided by meticulous sample preparation suppressed necking and allowed deformation until fracture under a constant strain path. In the absence of local necking, determination of the true fracture limits were possible together with the forming limits measured by a method developed in this thesis. Multi-scale strain maps revealed the sources of strain localizations at the global scale as the strain heterogeneities at the microstructure scale, confirming that the localizations originating from the microstructural features could indeed limit the formability of the samples. Then, the microstructural features causing the strain heterogeneities were identified, and their effects were determined both qualitatively and quantitatively. The results showed that the major effect belonged to the orientation of grains followed by the grain size. Grain boundary misorientation had inconclusive effects on the strain distribution. Two separate models were

developed in this work in order to quantify the location and magnitude of strain heterogeneities. The models used global strain, grain size and orientation as the only parameters, which were easy to obtain by relatively simple characterization techniques. When compared with experiments performed at large strains and large field-of-views consisting of many grains, the models successfully predicted both the location of heterogeneities and the strain accumulated in them.

Keywords: Aluminum, Formability, Multi-scale, Strain Heterogeneity, Grain Orientations

ÖZ

ALÜMİNYUM ALAŞIMLARININ ŞEKİLLENDİRİLEBİLİRLİĞİNDE GERİNİM HETEROJENLİĞİNİN İÇYAPISAL KÖKENLERİ

Güler, Baran
Doktora, Metalurji ve Malzeme Mühendisliği
Tez Danışmanı: Doç. Dr. Mert Efe

Aralık 2019, 106 sayfa

Sac metallerin şekillendirilmesinde, gerinim yerelleşmeleri ve takip eden boyun verme, genellikle kalınlık farklılıkları gibi geometrik kusurlar sebebiyle oluşur. İçyapısal heterojenlikler de gerinim yerelleşmelerinde rol oynar, ancak bunların etkileri makro ölçekteki şekillendirilebilirlik düşünüldüğünde ihmal edilir. Bu tez, içyapı unsurlarının aluminyum alaşımlarının gerinim yerelleşme davranışı üzerine etkilerini incelemiştir. Bu amaç için küçük ölçekli bir eşeksenli test cihazı ve numunesi kullanılmıştır. Özel numune tasarımı ve titiz numune hazırlama sayesinde elde edilen kalınlıktaki tutarlılık, boyun vermeyi bastırmış ve numunenin sabit gerinim izi altında kırılana kadar deforme olmasın izin vermiştir. Boyun vermenin yokluğunda, gerçek kırılma limitlerinin belirlenmesi mümkün olmuş ve şekillendirme limitleri bu tezde geliştirilen bir yöntem ile ölçülmüştür. Çok ölçekli gerinim haritaları, global ölçekteki gerinim yerelleşmelerinin kaynağının içyapı ölçeğindeki gerinim heterojenliği olduğunu ortaya çıkartmış ve içyapı kaynaklı yerelleşmelerin de aslında şekillendirmeyi sınırlandırabileceğini doğrulamıştır. Sonrasında, gerinim heterojeniğinden sorumlu içyapı unsurları belirlenmiş ve etkileri nitel ve nicel olarak saptanmıştır. Sonuçlara göre, asıl etki tane yönelimlerine ait olup, bunu tane boyu tekip etmektedir. Tane sınır açılarının gerinim dağılımına etkisi yoktur. Gerinim heterojenliklerinin yeri ve büyüklüklerinin nitelendirilmesi için bu çalışmada iki farklı

model geliştirilmiştir. Modeller sadece global gerinim ve görece basit karakterizasyon teknikleri ile bulanan tane boyutu ve yönelimini parametre olarak kullanmıştır. Yüksek gerinim ve birçok tane içeren geniş görüş sahası altında yapılan deneyler ile karşılaştırıldığında, modeller gerinim heterojenliklerinin hem yerini, hem de bunlarda toplanan gerinimi başarı ile tahmin etmişlerdir.

Anahtar Kelimeler: Alüminyum, Şekillendirilebilirlik, Çok Ölçekli, Gerinim Heterojenliği, Tane Yönelimi

To my beloved family…

ACKNOWLEDGEMENTS

I feel so indebted to my advisor Assoc. Prof. Dr. Mert Efe for his nonstop support, faith on myself, encouragement, kindness, and approach on the problems that I encountered during this study. He had never stinted his academic knowledge and experience from me during my whole study. It would be impossible to complete without his guidance. I felt myself very confident knowing his support behind me.

I am also in a deep appreciation to Assoc. Prof. Dr. Tuncay Yalçınkaya and Dr. Süha Tirkeş who gave all that they got whenever I needed help. My friends and lab mates Berkay Bayramin, Kıvanç Alkan, Berk Aytuna, and Merve Çobanoğlu gave their mental and physical support all time. I especially thank to Erhan Özen for his sincere friendship during my undergraduate and graduate life. I am also grateful to Gizem Mumcu, Merve Öztürk, İlyas Bayrak, Umutcan Ertürk, Simge Tülbez, Zeynep Öztürk, Sena Okay, Semih Kurdoğlu, Abdurrahman Özdemir, Gözde Özdemir, Emir Dinçel and Elif Altındağ.

She is the one who entered my life and took my heart, Sarenur Sarı Güler. For today and future, I cannot imagine anything without her. I love you forever.

Last but not least, I owe to my father Necip Güler, my mother Sultan Güler and my sister Hazal Güler. They have never lost their faith and support on me. They have been my lovely supporters all my life who never expect anything in return.

TABLE OF CONTENTS

LIST OF TABLES

TABLES

LIST OF FIGURES

FIGURES

CHAPTER 1

INTRODUCTION

The formability is defined as to deform sheet metal into desired shape without local necking or fracture before which the heterogeneous deformation starts. For this purpose, the forming limit diagram (FLD) is widely used to evaluate the formability of sheet metals. It is a strain diagram, which can distinguish between safe points and necked or failed points. The transition from safe to failed points is defined by the forming limit curve (FLC) [1]. For experimental determination of FLCs, two main conventional biaxial tests are used, the out-of-plane stretching (e.g. Nakajima test) and the in-plane stretching (e.g. Marciniak test) [2]. However, there are some drawbacks of these conventional tests. The main drawbacks are the use of a high number of specimens with different geometry and the influence of friction originated from between the sample and the punch. Each geometry provides to reach various strain path. In addition, the generated friction may affect the forming limits.

Most importantly, the local neck formation is inevitable in the conventional tests due to the large sample dimensions, frictions effects, or the inconsistencies in the sample thickness. Therefore, the geometrical or mechanical constraints limit the sample formability, preventing a measure of direct material or microstructure effects on the global formability. Due to the local neck formation, these tests never reach the true fracture limits of the material under various strain paths as the stress state in the local neck is almost plane strain. Therefore, a typical FLC reflects both the material and geometrical effects and they can be highly sensitive to the external parameters that are not related to the sample material and its microstructure.

Suppressing local neck can provide to investigate true formability of the sheet metals depending on materials properties. The limits in formability are more often controlled

by localized necking, which is an undesirable surface defect, than fracture [3]. Necking is usually initiated by a geometrical heterogeneity of the material, which is a thickness variation [2]. Marciniak-Kuczynski model is widely used to predict forming limits, whose predictions depend on an initial geometrical imperfection [4]. In addition, there is an international standard ISO12004-2:2008 for FLC detection. However, it is not a precise standard to detect the onset of localized necking [3], [5]. Under equibiaxial tension, sheet metals may deform and fail without forming a local neck. In these cases, it is challenging to determine the forming limits by using the international standard and Marciniak-Kuczynski model since they are designed to detect the formability from a sharp, single local neck. Therefore, the geometrical imperfections determine the forming limits of the sheet materials and limit them.

Therefore the objectives of this thesis are: 1) suppression of the local neck in order to provide forming limits due to the material behavior instead of geometrical imperfections; 2) developing the relation between the microstructural features and the strain heterogeneity in forming of Aluminum alloys by investigating the strain localization behavior at multiple scales. The multi-scale observations are necessary to test the effects of strain heterogeneity at the micro-scale to the meso- and macro-scales. This way it is possible to establish the direct effects of microstructure or material related strain localizations to the global formability of the material. Aluminum 6061-T6 is selected as the test material due to its uniform microstructure and properties. In addition, the mechanical properties are also considered isotropic [6]. Therefore, the material related effects are minimized. Micro- and meso-scale are defined as at least two dimensions of the investigated region are less than 1.0 mm and in the range of 1-10 mm, respectively [7].

In order to achieve the first objective of the thesis, a cruciform test is developed in chapter 2 as an alternative test to characterize the formability. The main advantage of this test is that a unique geometry is sufficient to cover the whole FLD. By changing the load distribution on the axes, different strain paths can be obtained. Another benefit is that the test is frictionless, so the formability is determined without any influence of

friction [8]. However, the design of the cruciform specimen is crucial in this test. The center test region of the specimen must experience minimum shear strain, the maximum stress and strain values [9]. A successful cruciform design, which accumulates large strain in its test region, is introduced in this chapter. The small strain and premature fracture problems common to the cruciform tests are solved by optimizing the sample design and by meticulously controlling the manufacturing steps and surface finish. Strain analyses reveal a key mechanism responsibly for large strains and fracture at the center. This mechanism suppresses the local neck formation and allows uniform deformation under equibiaxial tension until fracture. In addition, a novel portable biaxial tensile test apparatus is introduced to conduct cruciform tests, which includes a custom-built optical microscope and high-resolution digital image correlation (DIC) equipment for in-plane and in-situ strain measurements. This chapter is reproduced from the studies of [10], [11]. In addition, the materials and methods part of this chapter is enriched by the study of [12].

In chapter three, the true forming limits are measured, as the cruciform test allowed deformation without the local necking. However, there has been no measurement method available in the literature for the absence of local necking. In addition, in this chapter, an alternative Marciniak-Kuczynski based thickness strain ratio method (TRM) is introduced to measure forming limits and fracture limits of the Aluminum 6061-T6 and a DC-04 steel. In this case, the DC-04 steel served as a ductile reference material compared to the relatively brittle aluminum alloy. The experimental forming and fracture limits obtained by the cruciform test are compared with those obtained by the standard Nakajima test containing sharp local necks in order to ensure the reliability of the measurement method. In addition, TRM method and the international standard are compared to each other. Therefore, the effects of neck suppression on the forming and fracture limits of both relatively brittle and ductile alloys are investigated. This chapter is reproduced from the study of [13].

In chapter four, the multi-scale deformation behavior of Al 6061-T6 alloy is investigated in order to establish the effect of microstructural features on the strain

distributions and localizations at the larger scale, i.e. meso-scale (test region) in this chapter. The hypothesis was the large-scale localizations originating from the microstructure level heterogeneities, as the geometrical parameters could no longer be the source of the localizations. Therefore, the aim was to correlate strain localizations at the micro-scale to the meso-scale. In the literature, the multi-scale investigations are conducted in different regions of the samples. However, the same region should be investigated to characterize strain localization behavior at both scales. For this purpose, a test procedure, which allows investigation of the same region of the sample after the same amount of loading, is introduced. The size difference of the investigated scales is in the order of 7 times. In addition, the size of the investigated regions at micro-scale is sufficient to show the micro-scale strain distribution at meso-scale.

After establishing the relationship between micro- and meso-scale localizations, the microstructural features, which take role in strain distribution, are investigated to fulfill the second objective of the thesis. The microstructural constituents can provide sources of deformation heterogeneity, which can cause premature localized deformation. The understanding of the role of various microstructures factors, i.e. grain structure, on strain localization is still incomplete in the literature. It is known that the crystallographic texture (e.g. the distribution of crystal orientations) is a major cause of deformation inhomogeneity, so it can strongly influence the mechanical properties of metals [14]. In addition to grain orientations, grain size takes role in the development of plastic deformation heterogeneities [15]. The prediction of strain distribution is based on numerical approaches, and they are relatively complex to use to comment strain heterogeneity. Despite of the improvements in numerical approaches, large inconsistences still exist between numerically predicted mechanical behavior and what is observed experimentally [16]. Also, the experimental investigations in the literature do not deal with the prediction of strain distribution. They are based on establishing the reasons of strain localization behavior. In addition, they are conducted in controlled microstructures and for small field-of-views containing only limited number of grains. The investigated global strains are also

small compared to the typical strains achieved in forming processes. In chapter five, the prediction of strain distribution by experimental investigations is aimed. Al 6061-T6 was examined to understand how microstructural parameters affect the strain distribution. It consisted of as-received microstructure having random texture, random grain size, and mostly high-angle grain boundaries, instead of a more controlled microstructure. The investigated field of views and strains were large. Therefore, the parameters affecting strain heterogeneity can be established in a more realistic approach. To predict strain distribution, two methods, which are strain localization indicator (SLI) method and strain localization magnitude (SLM) method, are developed and presented in this chapter. They were based on easy-to-measure, microstructural parameters. In conclusion, the reasons behind the heterogeneous deformation are discussed, the parameters that are responsible from the heterogeneous strain distribution are presented, and the strain distribution is quantified.

CHAPTER 2

LARGE STRAIN CRUCIFORM BIAXIAL TEST METHOD FOR IN-SITU FORMABILITY ANALYSIS OF SHEET SAMPLES

2.1. Introduction

The forming abilities of materials can be tested under different loading conditions such as uniaxial tension, equibiaxial tension, plane strain, pure shear, etc [2]. Although uniaxial tension is most common testing method, it may underestimate the formability in a practical forming operation while multi-axial deformation analyses in metal materials best represent the real sheet forming behaviour [17]. Bulge test, biaxial tensile test, Marciniak test and Nakajima test can access large strains and multi-axial loading paths compared to the uniaxial tension. However, these methods other than the biaxial tensile test have significant limitations such as bending effect, friction effect, non-homogeneous material flow, presence of early necking, out-of-plane deformation, large-scale application etc. In cruciform biaxial tension testing, cruciform shaped sample enables collection of the stresses at the centre of the specimen [8]. On the other hand, achieving large stresses and strains at the centre remains to be an issue among various designs reported in the literature, which tend to be large and complex. At that point, due to the various cruciform designs existing, the international standard ISO 16842:2014 standardize cruciform biaxial tension test [9]. However, the shape in this standard is not useful for achieving large strain since high strain is not obtained at test region in cruciform biaxial testing.

Large strain capability and strain path flexibility of cruciform biaxial tests are useful for small-scale (microstructure scale) testing of materials which have deformation mechanisms sensitive to their unique microstructural features. Studies focusing on local deformation behaviour of lightweight metals such as aluminium, magnesium and

titanium alloys have shown that micro-scale deformation alters the macro-scale behaviour [18]–[20]. As a result, these materials may have complex forming behaviour compared to regular steels and their forming ability should be studied at the small-scale [21]. At that point, the design indicated in the standard is not suitable for micro-scale investigation due to large dimensions (240 mm in length). In this chapter, a portable and easy to use biaxial test apparatus, which is suitable for both meso-scale and micro-scale testing, and the successful cruciform design are introduced.

2.2. Materials and Methods

2.2.1. Biaxial Test Apparatus

The test mechanism, as shown in Fig. 2.1. (upper body of the apparatus), is designed and manufactured in collaboration with UTEST Company (OSTIM, Ankara, Turkey). It has changeable arms and load cells attached to each arm in order to achieve various loading paths. The whole apparatus is designed to be portable and can be integrated to any simple uniaxial, bending or compression universal test machine, in this case to a Shimadzu Bending Test Machine (10 kN capacity). When compression load is applied, this apparatus distribute the load to four arms with respect to the angle between the arm and vertical axis. Each axis of the loading mechanism moves independently on a rail and they are all connected to load cells. Horizontal load on each axis can be controlled by adjusting the angle between the horizontal axis and vertical arms that are connected to the test machine, as $F_{on\ axis} = (F_{machine} \times tan\theta)/4$. In equibiaxial condition, load difference between each horizontal arm is less than 100 N. This is achieved by placing the cruciform sample in the apparatus and applying 15-25 N pre-load to each axis by tightening the screws connecting the horizontal axis and the vertical arms with equal length. This way each arm is connected to the axis at a fixed distance from the sample center, making θ equal for each axis. Only tensile stresses and strains are possible which corresponds to the right side of the forming limit diagram (FLD). The apparatus can be modified for compressive stresses in order to explore the left side of FLD.
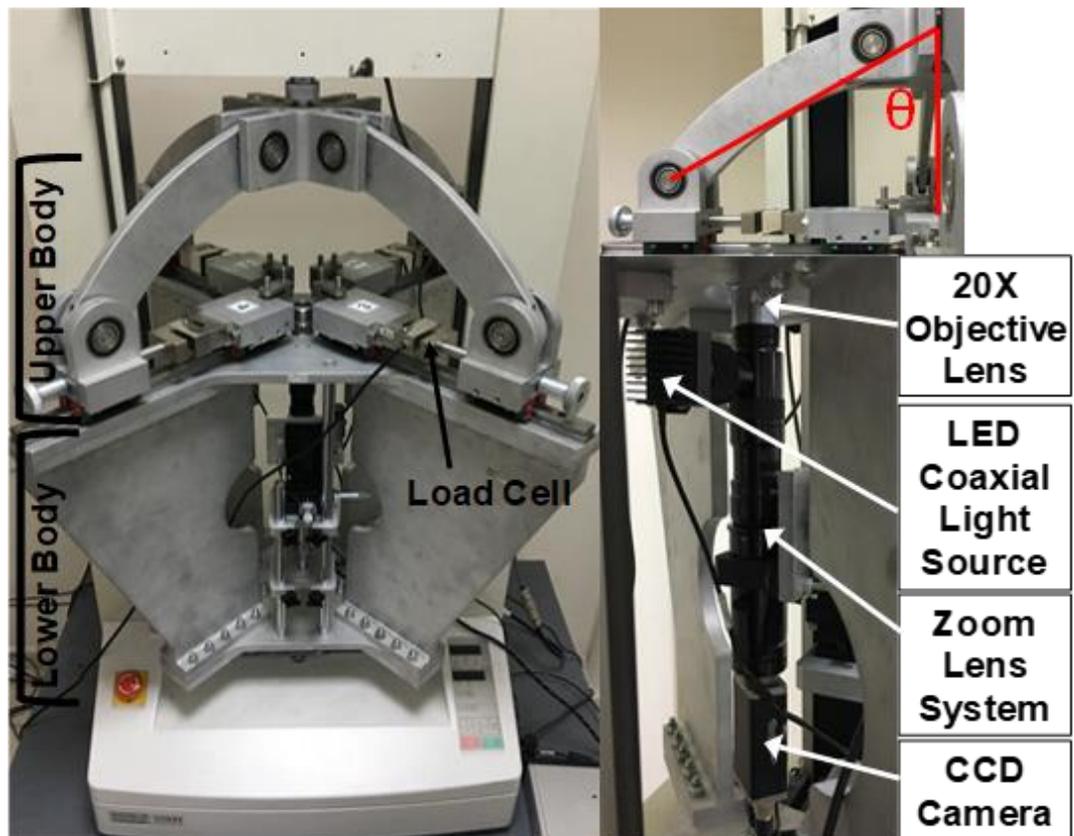
Figure 2.1. Biaxial test setup.

2.2.2. Digital Imaging & Correlation Setup

The lower body of the apparatus houses the imaging unit. The imaging unit consists of Basler piA2400 - 17gm (5 MP, 2/3" Sony ICX625 CCD sensor) camera and Navitar UltraZoom 6000 lens including 2X adapter and a coaxial LED illumination. The maximum resolution of the camera is 2448 x 2050 pixels at 17 frames per second with a shutter speed of 1/100,000. Overall magnification range is between 1.40 - 9.00X for meso-scale configuration, and 14X - 91X for micro-scale configuration that includes the 20X objective lens. To observe whole test region (2 mm in diameter), the macro-scale imaging configuration was set to 3X magnification resulting 2.9 x 2.2 mm^2 as

the field of view. The imaging setup can also be configured for the microstructure scale analysis by changing the lens settings.

The random speckle pattern correlation necessary for the correlation was prepared by spraying a black paint solution on the test region. Paint solution contained 30% of acrylic paint and 70% of acetone, and sprayed with Bad Sector BD-130 air brush operating at 45 psi pressure with 10 cm distance from the sample surface. This process resulted in randomly distributed pattern with ~ 20 µm size black dots (speckles).

2D DIC technique was used to determine the strain values. For correlation, an open source MATLAB based software named as Ncorr v1.2 [22] was used. Incremental method was applied to conduct DIC. When pattern deterioration was visually noticed between any two images, the images were selected and correlated among the images were captured during tests, corresponding to 1 fps at a deformation rate of 1 mm/min. The meso-scale DIC analysis of biaxial tests had a subset size (radius) and step size of 80 and 10 pixels, respectively, at a spatial resolution of 0.0012 mm/pixel.

The maximum strain error calculated by rigid body translation was 0.14%. Theoretically, rigid body translations should yield no strain. Therefore, strain after the translation must be the error from pattern preparation (speckle pattern), optical system (imaging), and correlation algorithm [23]. Ncorr's correlation algorithm error was calculated to be 10^{-13} [22]. Similarly, the error from the optical system should be relatively low [23]. Therefore, speckle pattern produces most of the strain error, which was reduced to lower values by optimizing the spraying pressure, distance and solution, which resulted in sharper and smaller speckles, which are apart from each other. Pattern contrast was also improved by adjusting the lighting conditions. The outcome strain was Green-Lagrangian. Then, true strains were calculated by means of following equation:

$$\varepsilon = \ln(\sqrt{2E + 1}) \hspace{3cm} (2.1.)$$

where E and ε are Green-Lagrangian and true strains, respectively [24].

10

2.2.3. Sample Material

Aluminum 6061-T6 was selected as the test material. In addition, it has uniform microstructure and properties, minimizing the material related effects on deformation. The 2 mm thick sheet purchased from Aleris Aluminum; Duffel, Belgium, had a grain size of 58 ± 15 µm and hardness of 108 ± 4 kg/mm^2. The material has 0.11 as strain hardening exponent in their rolling direction. Table 2.1 documents the average tensile properties of the sheet. Tensile tests were conducted in an Instron 5582 universal tensile test machine with extension controlled of 3 mm/min rate and strain data were measured by a video extensometer. At least seven samples were laser cut parallel to the rolling direction and dimensions were based on ASTM E8. Except the strain hardening exponent, all properties were determined from engineering stress-strain curves.

Table 2.1. *Mechanical Properties of 6061-T6 Aluminum Alloy*

Mechanical Properties	M
Tensile Stress at Yield (Offset 0.2 %) (MPa)	270 ± 1
Maximum Tensile Stress (MPa)	329 ± 0.3
Tensile Strain at Break (%)	16.5 ± 1
Strain Hardening Exponent	0.115 ± 0.001
Microhardness (kg/mm^2)	108 ± 4

Figure 2.2. shows the representative true stress-strain curve used for determining the hardening exponent by means of power law ($\sigma = K\varepsilon^n$). The figure was retrieved from the study of [12].
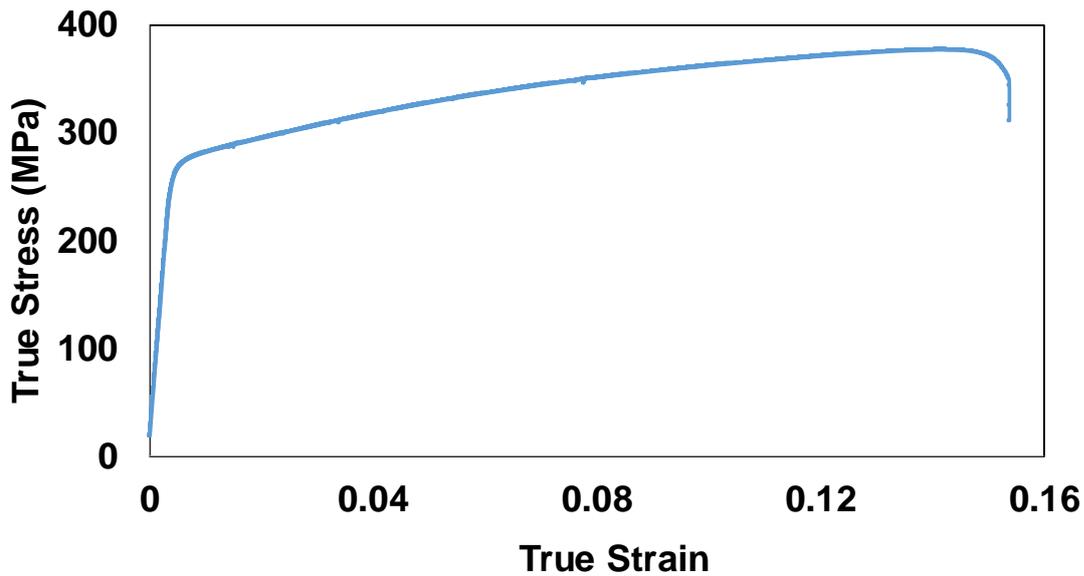
Figure 2.2. Representative true stress-strain curve of Aluminum 6061-T6 alloy.

2.3. Cruciform Sample Design

To have a successful in-plane biaxial test, the design of cruciform specimen should satisfy the following criteria: maximum stress and strain should be located in the test region i.e. center of the specimen and shear stress should be zero in this region [25]. Failure should take place inside the test region. In addition, manufacturing of the specimen should be economical.

In addition to these, the specimen should be relatively small-scale for the investigation of micro-mechanical behavior during deforming. In other words, the dimensions of test region should be smaller than the field of view of the imaging setup that allows DIC at the microstructure scale. Otherwise, some grains or microstructural features can move out of the field of view of the imaging system during deformation, preventing DIC analysis for large strains that are typically observed before the fracture. In addition, for proper and focused imaging, the test region should be flat. Lastly, when constructing FLC, the specimen should meet all these criteria stated above under the different loading ratios.

12
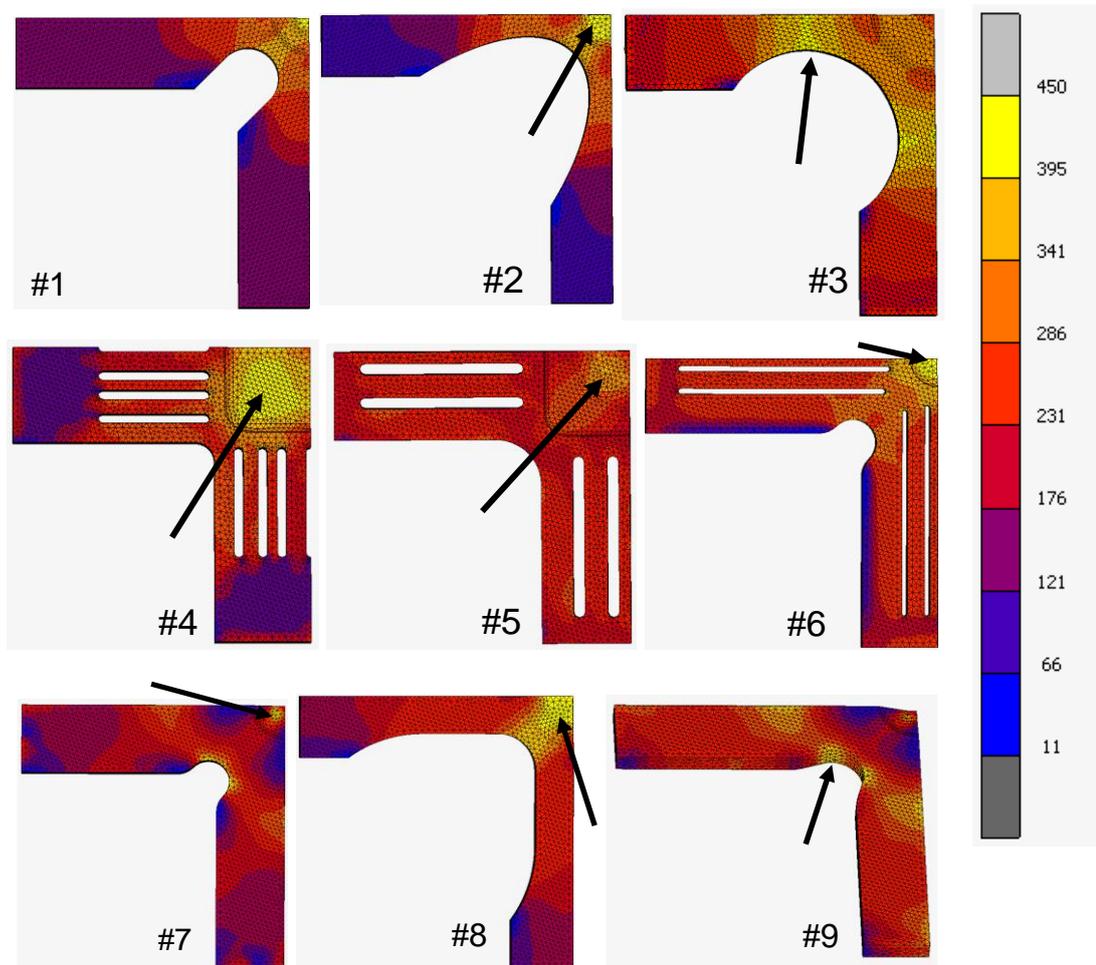
Figure 2.3. FEA results of various cruciform design. The numbers correspond to sample design numbers in Table 2.2.

The most suitable design satisfying the above criteria was decided using nonlinear Finite Element Analysis (FEA). Figure 2.3. shows the nine designs selected from literature. Elastic-Plastic Isotropic module in MSC Marc 2014.2 was used to map the distribution of the equivalent stresses and plastic strains. The yield criterion and hardening rule were selected as von Mises and isotropic, respectively. The true stress-strain data for plasticity analysis were obtained from the tensile test. Due to the symmetry, 1/8 of the specimens was modeled with 0.25 mm quadratic tetrahedral type

mesh. The mesh size got finer (0.1 mm) at the test region. The FEA included nine designs available in the literature. As these designs have relatively large dimensions, they were scaled down to 85 mm in length and 2 mm in thickness to fit them in the testing setup. All the design features and proportions were kept constant, but the center thickness was reduced from 2 mm to 0.5 mm by adding a flat-base pit at the sample center. The flat-base pit ensures in-plane deformation and a proper 2D-DIC analysis.
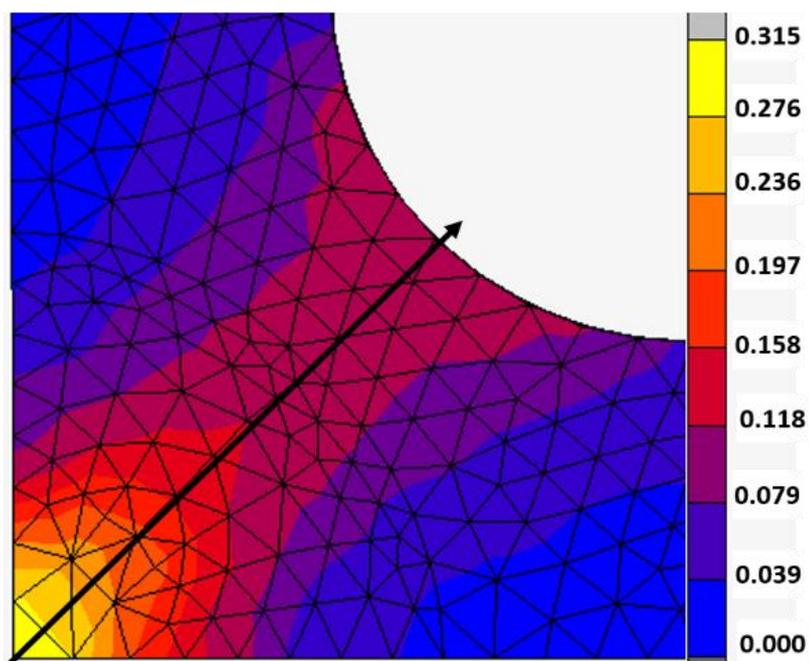
Figure 2.4. FEA result of the cruciform sample with respect to the total equivalent plastic strain.

Table 2.2. lists the locations of maximum stress concentrations for each design shown in Fig. 2.3. Among all the nine designs, the Design 1 is the most promising.

Table 2.2. *Locations of maximum equivalent stresses in FEA of various cruciform design*

Sample Design [Reference]	*The Location of Maximum Stress*
1 [26]	Center
2 [27]	Edge of the pit
3 [28]	Arm
4 [29]	Edge of the pit
5 [30]	Edge of the pit
6-without slits [31]	Edge of the pit
7-with slits [31]	Near the center
8 [32]	Edge of the pit
9 [33]	Arm

Figure 2.4. shows the FEA results of the cruciform sample where maximum total equivalent plastic strain is obtained at the center. Figure 2.5. illustrates the total equivalent plastic strain distribution from the center to the corner of the sample.
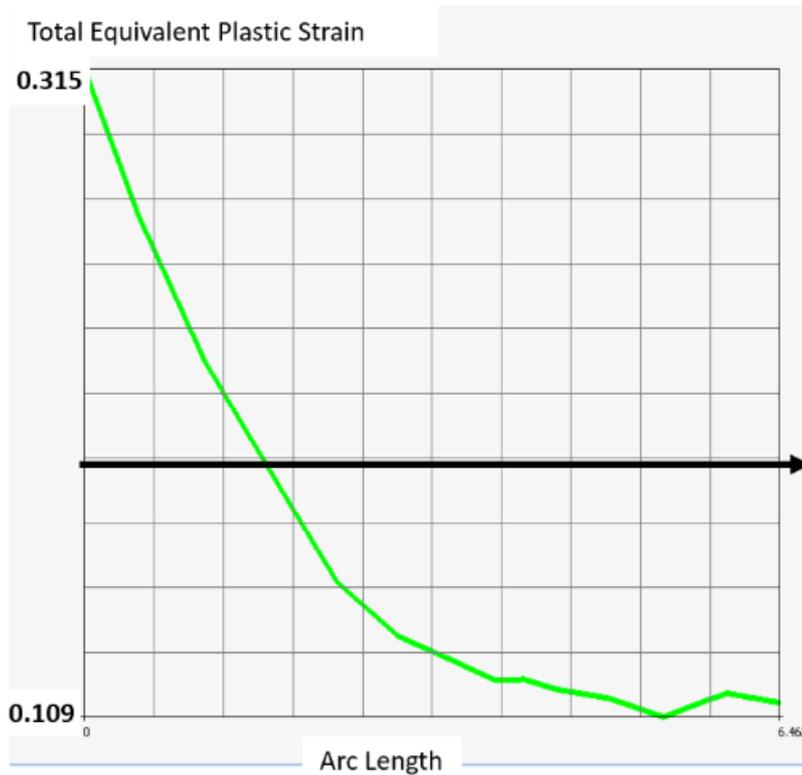
Figure 2.5. Distribution of total equivalent plastic strain from center to corner.

The cruciform sample design (Design 1) shown in Fig. 2.6. was originated from [26]. Further improvements were conducted to obtain maximum strain at the centre. The pit region shown in Fig. 2.6. was drilled by means of a CNC milling machine, resulting in good surface finish and smooth test region. The roughness of 2 mm test region was measured as Ra ≈ 2 µm while the as-received sheet has smaller than 0.4 µm as Ra. Surface roughness of the machined pits was measured by Mitutoyo Surftest SJ-400. As the test regions of the samples were a few millimeters away from the edges, laser cutting did not alter the test results. The final dimensions and the geometry of the cruciform sample was illustrated in Fig. 2.6. Therefore, this design of cruciform sample was used for whole thesis.

16
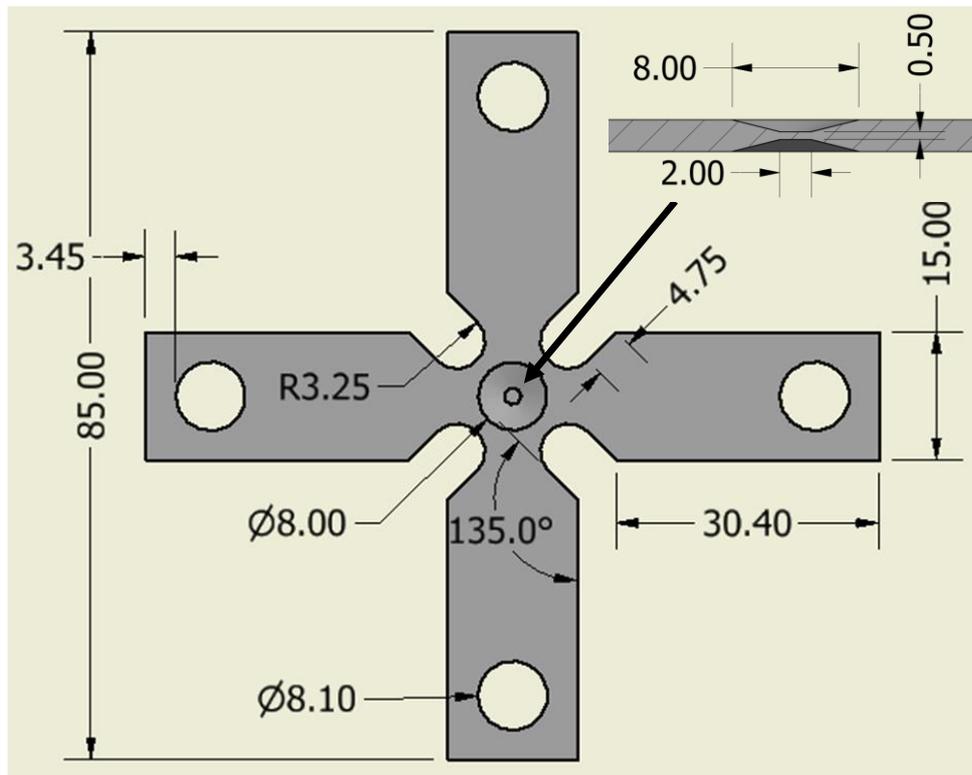
Figure 2.6. Cruciform sample and pit design resulting in center fracture. Dimensions are in mm.

2.4. Obtaining Large Strain at the Center

To obtain large strain at the center, the design of the cruciform sample and the pit take an important role [8]. The most important parameter in the pit design is the thickness reduction ratio, which increases the chances of center fracture [34]. Single reduction for simple manufacturing was preferred, and the maximum reduction was 75% corresponding to 0.5 mm thickness. Centre region became delicate and fragile below 0.5 mm thickness. Since a flat and smooth base is necessary for imaging and 2D-DIC, a bowl-shaped profiles are not suitable for our application. Instead, the tapered profile in Fig. 2.6. was selected and optimized with regards to results of (FEA). Two symmetrical pits were machined on opposite sides of the sample resulting a constant thickness of 0.5 mm at the center. First, the end-mill (2 mm end diameter) made exact to the pit dimensions was used. However, the surface finish of the pit machined in just

17

one step was not acceptable as the center was slightly thicker (~ 40 µm) than the edges resulting that some samples failed from the edges. This a common problem indicated in the literature due to the poor machining of the pit [34]. The smooth surface finish, uniform thickness were achieved by circulating the additional smaller diameter (1 mm) end-mill within the pit. Eventually, the samples failed or cracked from the center due to achieving uniform thickness. Besides the pit design, accurate and precise machining was equally important in obtaining strain localization at the center by achieving superior surface finish.

As center fracture was possible in the sample with tapered profile pit, the strain analysis was conducted in the test region. Figure 2.7. shows the distribution of the principal strains just before the fracture. The justification of the localized large strain at the center is the two diagonal bands present in the strain maps [12]. These bands origin from the unique geometry and deformation characteristics of the cruciform samples can be seen in the results. The bands linked the opposite diagonal corners and cross each other at the center. There was also shear deformation and inhomogeneous localized areas along the bands while the shear strains approached to zero at the center where two bands intersected each other providing relatively uniform deformation. As the shear strain was not zero, the whole pit region should not be considered as the test region even if the median true strains were balanced under equibiaxial tension test. The true equibiaxial condition was achieved at the center within a circular area having 1 mm diameter and this location was selected as the test area shown in Fig. 2.7. since shear strain should be minimum under equibiaxial tension [35]. The principal strains were maximum at the 1 mm-diameter test region while the shear strains were approximately zero. Median true principal strains in this region were calculated as ε_1 = 0.16 and ε_2 = 0.14 for Al 6061-T6, which results in equivalent strain $(\bar{\varepsilon})$ of 0.3. The equivalent strain was calculated by the following equation:

$$\bar{\varepsilon} = \sqrt{\frac{2}{3}\{\varepsilon_1^2 + \varepsilon_2^2 + \varepsilon_3^2\}} \tag{2.2.}$$

For Aluminum, $(\bar{\varepsilon})/n$ ratio reached 3. Therefore, the two intersecting strain bands maximized the principal and equivalent strains at the center, and promoted fracture at the same location. Outside the bands, the strains were lower and close to the strain hardening exponent of the material.
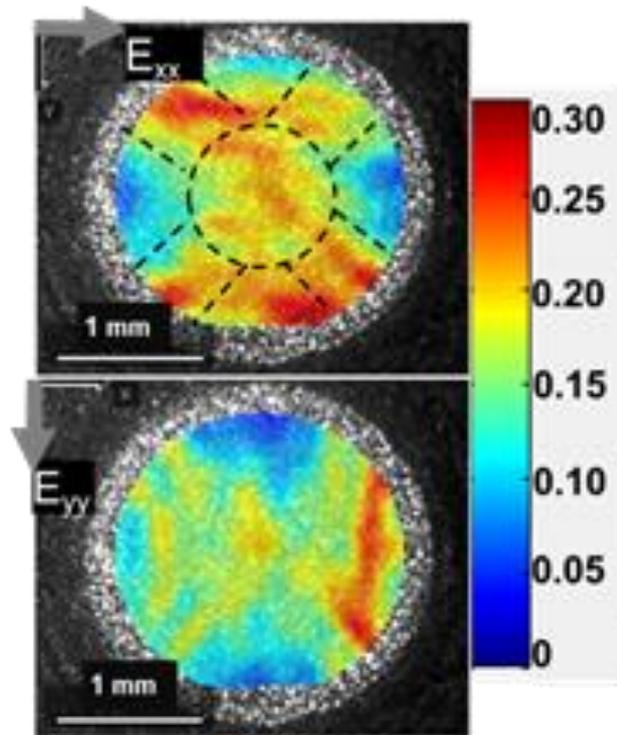
Figure 2.7. DIC Results of Al 6061-T6 up to fracture. The upper results for E_{xx} while the below for E_{yy}. The strain bands are shown as dashed lines.

The strain bands may originate from the corners. Together with the pit, the corners may deform uniformly until the overall strain reaches n. After this, necks form at all corners and strain bands connect them. As strain bands intersect each other at the center, this region continues to deform under equibiaxial tension and reaches large equivalent strain. Strain localizations are concentrated in the strain bands and the center, while the rest of the sample remains no deformed. Indeed any cruciform

geometry can develop this type of strain distribution, as the stress concentration at the corners is unavoidable. In our case, the strain bands were distinct due to the small-scale of the samples, where the width of the strain bands is nearly 1 mm, equal to the diameter of the test region. This mechanism was investigated in detail in the study of [12].

2.5. Conclusion

Cruciform biaxial tests are increasingly becoming popular for testing the formability of sheet metals as they achieve frictionless, in-plane, multi-axial stress states with a single sample geometry. However, premature fracture of the samples during testing prevents large strain deformation necessary for the formability analysis. In this chapter, the miniature successful cruciform design (few mm test region) optimized by using finite element analysis, and a test setup were introduced to achieve center fracture and large uniform strains. With its excellent surface finish and optimized geometry, the sample deformed with diagonal strain bands intersecting at the test region. These bands prevented local necking and concentrated the strains at the sample center. Imaging and strain analysis during testing confirmed the uniform strain distributions and the center fracture were possible for various strain paths ranging from plane-strain to equibiaxial tension. Moreover, the sample deformed without deviating from the predetermined strain ratio at all test conditions, allowing formability analysis under large strains. Thus, these features of the cruciform test were demonstrated for Aluminum 6061-T6 alloy.

CHAPTER 3

FORMING AND FRACTURE LIMITS OF SHEET METALS DEFORMING WITHOUT A LOCAL NECK

3.1. Introduction

Sheet metals are subjected to multi-axial or biaxial strain paths during forming operations and fail mostly by local necking followed by fracture [36]. Conventional tests measuring the forming limits of the materials have been designed to detect the onset of local necking under the multi-axial strain paths. Tests such as Marciniak, Nakajima, and bulge test employ different sample geometries to reach various predetermined ratios of principal strains (ε_1 and ε_2). This initial strain ratio gets disturbed at the onset of the local neck and quickly reaches to the plane-strain condition ($\varepsilon_1 >> \varepsilon_2$) inside the neck [37]. For ideal formability, strain distributions should be uniform across the deformation area with the fixed ratio of principal strains [37]. The forming limit, therefore, is the point where there is significant deviation from the predetermined strain ratio. When the deviation happens in a sharp local neck, it is easy to detect, and there is an international standard ISO12004-2:2008 for reporting of the forming limiting curves (FLC).

On the other hand, non-uniform strain distributions and multiple local necks can sometimes be observed during deformation due to the material properties [38] and the process parameters [39]. The study of [40] indicated that for materials showing non-homogeneous deformation, the international standard leads to invalid evaluations and strain rate based (time dependent) methods were introduced as alternatives to overcome this problem. Also, this study compared several strain based methods with the ISO method and concluded that the linear best fit method based on the research of [41] was the most successful among them with regards to accuracy and stability. In

these methods, an abrupt increase in the thickness direction strain rate ($\dot{\varepsilon}_3$) signals the onset of local necking while the evolution of major strain rate ($\dot{\varepsilon}_1$) was also used to detect the onset of local necking. The study of [5] indicated that the noise originated from DIC (Digital Image Correlation) measurement had significant effect on the strain rate calculations and they were user-dependent. To overcome these drawbacks, they proposed a user independent thickness-control method recommended for non-homogeneous deformation.

Determination of forming limits from the onset of necking is also challenging when the fracture occurs without the formation of an obvious neck. Materials with relatively low formability (some aluminum alloys) [42] and complex microstructures (advanced high strength steels) may fail by fracture before localized necking [43]. While there is a significant difference between fracture strain curves and forming limit curves of ductile metals [44], these curves approach each other for materials with low strain hardening exponent, especially near the equibiaxial condition, resulting in fracture without necking [42]. Micro formed foils with large grain size also show brittle behavior. As the grain size approaches to the foil thickness, heterogeneous strain localizations lead to random fracture events [7]. In addition to the material related conditions, necking can be suppressed during bending, stretch flanging and incremental forming of complex geometries [45]. The test material fails from the strain localized spots instead of developing a sharp, single neck and the ISO method for determining the forming limit cannot be applied [46]. Plotting fracture limit curves instead of FLC can be another alternative, but strain localizations start well before the fracture [47].

This chapter demonstrates a test and an M-K based thickness strain ratio method (shortened as thickness-ratio method-TRM throughout the thesis) for the right side of the FLD (from plane-strain to equibiaxial condition) in sheets deforming without an obvious local neck. In-plane biaxial test (cruciform) is chosen as the method due to its advantages over the conventional biaxial tests. There is no punch in the cruciform test, and it utilizes a single sample design for a wide range of strain ratios. The in-plane

deformation is suitable for mapping the strain distributions with a 2D-DIC. Recently, the test has been used to determine the forming and fracture limits of aluminum alloys [9]. The authors were able to reach high strains with their design and concluded that the test is suitable for constructing FLC. Parallel to their results, the cruciform test used in this chapter was also able to reach large strains [12]. More importantly, the local necking was suppressed due to the unique sample geometry and deformation conditions [12]. Therefore, the test should be ideal for simulating and examining deformations with strain localizations instead of the local necks. To support this hypothesis, a relatively brittle Al 6061-T6 alloy and a high formability DC-04 steel are chosen as the sample materials and the experimental forming and fracture limits with the standard Nakajima test and the ISO method are compared each other. Therefore, the effects of neck suppression on the forming and fracture limits of both relatively brittle and ductile alloys are investigated.

3.2. Materials and Methods

3.2.1. Sample Materials

Aluminum 6061-T6 and DC-04 steel were selected as the sample materials having relatively lower and higher formability (work hardening index), respectively. In addition, they have uniform microstructures and properties, minimizing the material related effects on the limiting strains. The details of Aluminum material are indicated in chapter two. The 2 mm thick DC-04 steel sheet purchased from Erdemir, Turkey, was interstitial-free and designed for high formability applications. It had a grain size of 39 ± 8 µm and hardness of 255 ± 5 kg/mm^2. The mechanical properties of these materials (Table 1) were obtained by tensile test based on the ASTM E8 standard. The details are indicated in chapter two. All properties indicated in Table 3.1. were calculated from the engineering stress-strain curve obtained by the tests, except for strain hardening exponent, which was calculated using power law from the true stress-strain curve. The mechanical properties of Aluminum 6061-T6 are once more shown to compare the DC-04 steel.

Table 3.1. *Mechanical properties of Al 6061-T6 and DC-04 steel*

Mechanical Properties	*Al 6061-T6*	*DC-04*
Yield Stress (Offset 0.2 %) (MPa)	270 ± 1	171 ± 2
Maximum Tensile Stress (MPa)	329 ± 0.3	287 ± 0.4
Tensile Strain at Break (%)	16.5 ± 1	45.6 ± 1
Strain Hardening Exponent	0.115 ± 0.001	0.210 ± 0.002

3.2.2. Cruciform Sample Design and Manufacturing

The international standard ISO 16842:2014 aims to standardize the cruciform test since various cruciform designs exist in the literature. However, the study of [9] indicated that the design in this standard is not useful for determining the forming limit strains since it fails prematurely from the arms, preventing the accumulation of high strains in the test region, so the measured formability values may not represent the real forming behavior. For a viable design, maximum stress and strain should be obtained at the specimen center, followed by the fracture at the same region as well as stress and strain distribution should be uniform and shear stresses should be minimal [25]. To satisfy these criteria, the successful design is determined and its detail is indicated in chapter 2.

3.2.3. Biaxial Test Setup

The details of biaxial test setup are indicated in chapter two. In this chapter, five different test conditions were conducted by using arms with varying lengths, fixing the angle for each arm pair. These conditions were ranging from equibiaxial tension to plane-strain, which allowed the determination of the limiting strains on the right side of the forming limit diagram (FLD). To obtain the desired ratio of minor strain to major strain for isotropic and von-Mises type materials, the load ratio was adjusted according to the following equation:

$$\propto = \frac{(2 * \beta + 1)}{(2 + \beta)} \tag{3.1.}$$

where α equals to the load ratio between the axes and β equals to the ratio of minor to major strain. To obtain β as 0 (plane-strain condition), 0.3, 0.5, 0.8 and 1 (equibiaxial condition), the load ratio between the axes should be adjusted as 0.5, 0.7, 0.8, 0.93 and 1, respectively.

3.2.4. Nakajima Test Setup

Nakajima test was conducted according to the ISO 12004-2:2008 standard at The Metal Forming Center of Excellence located in Atılım University, Ankara, Turkey. Zwick/Roell BUP 600kN machine was used with 100 mm in diameter punch. Four different test conditions were performed for the right side of FLD. Strains were measured by 3D DIC with GOM Aramis 4M. The design of specimens and test parameters were adjusted according to the standard. Polyurethane was used as lubricant material. The study of [48] indicated the advantages of this lubricant material as: increasing the forming limits and providing better deformation proportionality.

3.3. Results and Discussion

3.3.1. Strain Evolution in Cruciform Test

Figure 3.1. maps the strain distribution across the test region of the aluminum samples at five different strain ratios ranging from plane-strain to equibiaxial tension. Strain maps obtained just before fracture are devoid of local necking at β ratios 0.3, 0.5, 0.8 and 1. There are strain localization regions instead of a neck and video recordings show the crack and failure initiation at these regions. Only the plane-strain condition leads to a local neck that is perpendicular to the major strain (ε_l) direction. Except for this condition, the major and minor strains seem to accumulate along two diagonal bands crossing at the center of the sample. These bands are especially clear at the maps for $\beta = 0.3$ and $\beta = 1$ (Fig. 3.1. – dashed lines). In previous chapter, the unique geometry and deformation characteristics of the cruciform samples were identified as

the origins of these bands [12]. Corners of the sample develop necking due to the uniaxial stress state at these locations. The bands form due to the necking and connect the opposite, necked corners. As the bands are diagonal to the principal strain directions (i.e., the arms of the cruciform sample), major strain cannot accumulate along a perpendicular path that is typical in local necks. Both principal strains accumulate along the bands simultaneously. There is also shear deformation along the bands, but the shear strains approach to zero where two bands intersected each other. This location was selected as the test area and had a diameter of approximately 1 mm [12]. A similar test region is visible in the current results (Fig. 3.1 –dashed line). While the strain distributions along the bands are inhomogeneous and accompanied by the localized areas, strain distributions are relatively uniform at the 1-mm-diameter sample center.
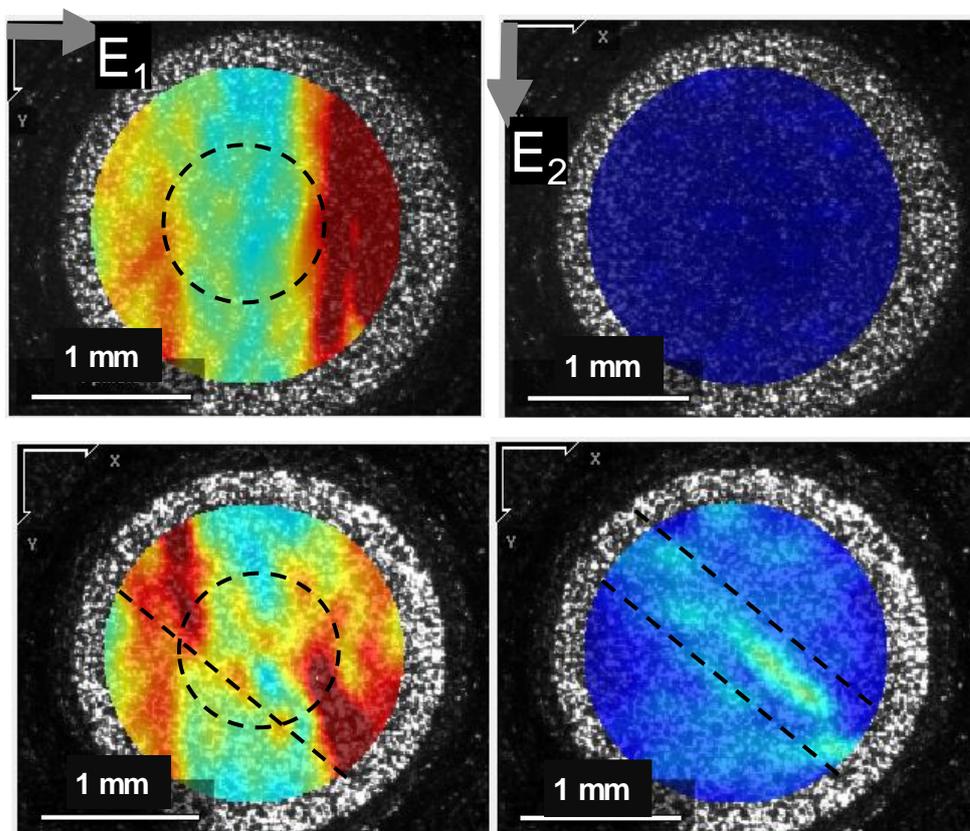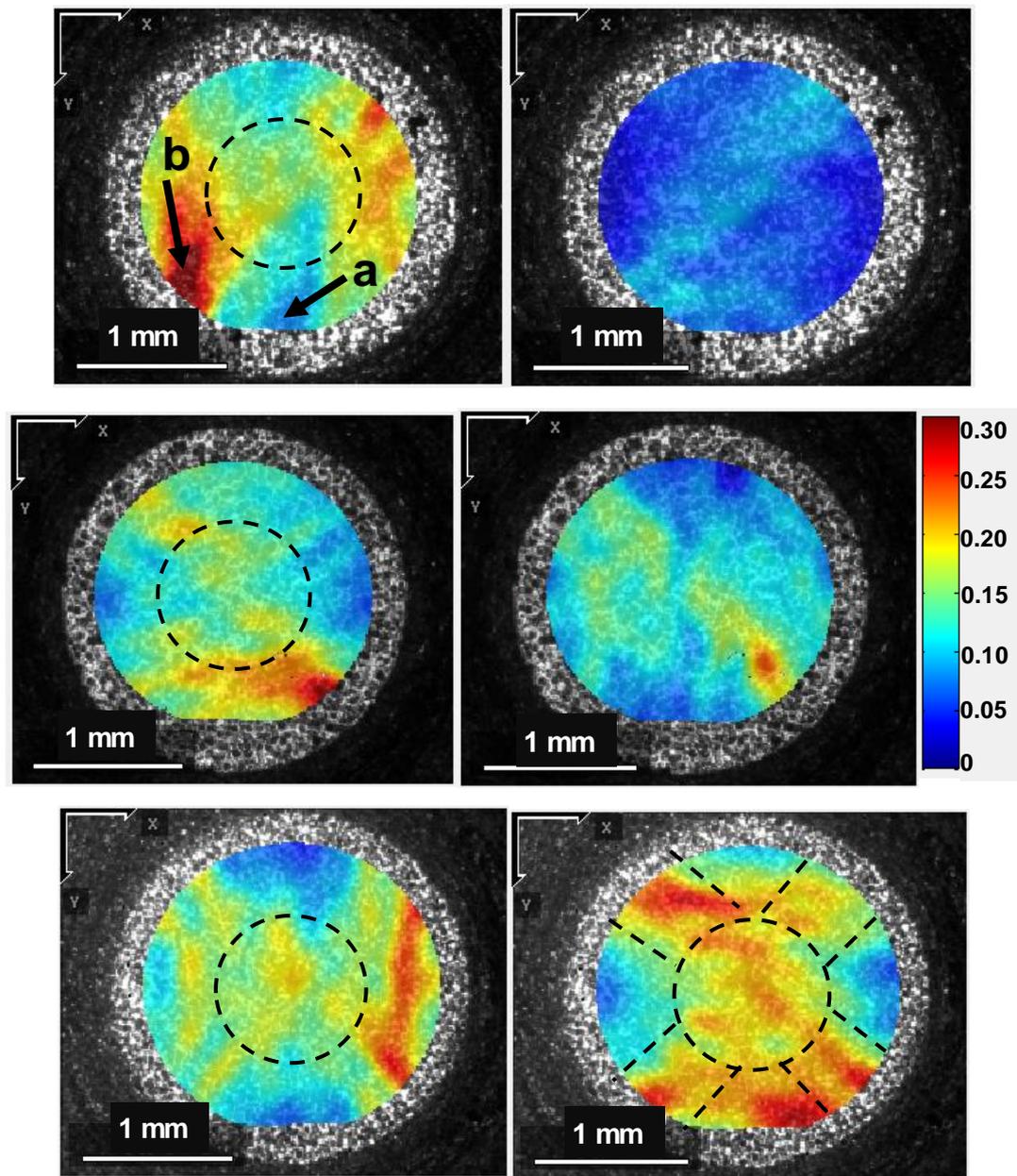
Figure 3.1. Distribution of major (left) and minor (right) strains before fracture in Al 6061-T6 cruciform samples tested at β = 0, 0.3, 0.5, 0.8 and 1 (from top to bottom). Diagonal strain bands are evident especially at β = 1 and intersect each other at the 1-mm-diameter sample center. Regions collecting the maximum (b) and minimum (a) thickness strains are shown on the maps.

Similar to the aluminum samples, continuous local necks are absent in the steel samples tested at various strain ratios, except *β* = 0 (Fig. 3.2.). The diagonal bands are

more evident and sharper at β ratios 0.3, 0.8 and 1, as strains accumulate along the bands. Strain accumulation along the bands is inhomogeneous, leading to the localized spots. In some test conditions ($\beta = 0.5$ and 1) one band is more dominant compared to the other, but the dominant band appears to be random. Again, the strain distributions at the sample center seem to be uniform. As expected from a highly ductile and formable material, steel samples reach substantially higher strains than the aluminum.
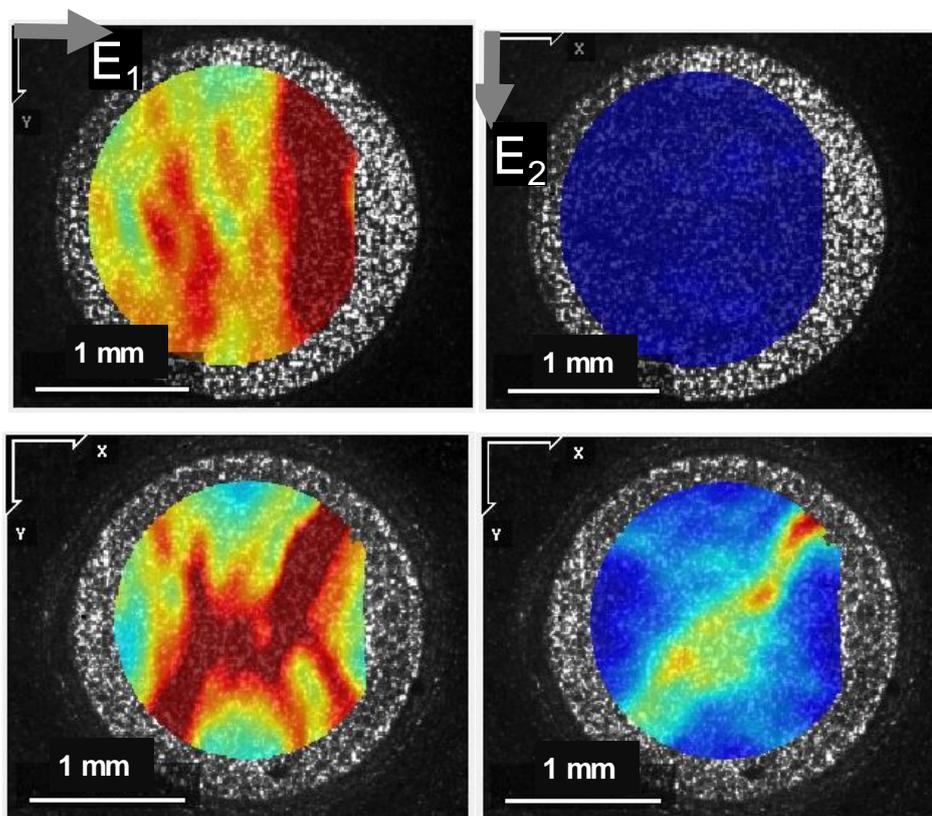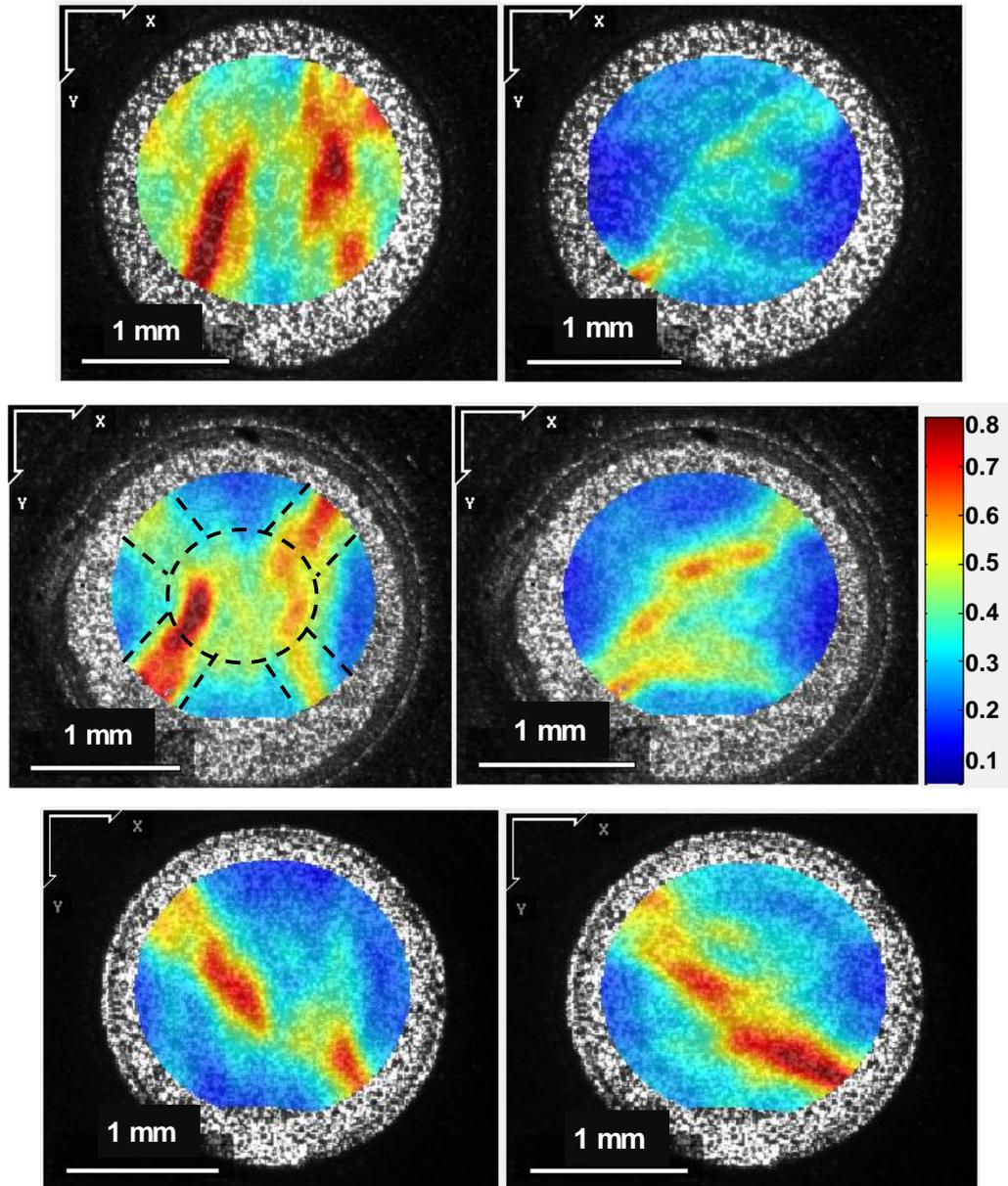
Figure 3.2. Distribution of major (left) and minor (right) strains before fracture in DC-04 steel cruciform samples tested at β = 0, 0.3, 0.5, 0.8 and 1 (from top to bottom). Diagonal strain bands are evident at all ratios, except β = 0.

In theory, plastic instabilities in the form of necks should not be observed in isotropic materials deforming under positive biaxial strains (right side of FLD) at constant stress and strain ratios [37]. On the other hand, the variations in sheet thickness due to

manufacturing, and internal inconsistencies in grain size, texture, inclusions or gaps lead to the local necking [4]. The local necks are more common in ductile materials, and the $d\varepsilon_2/d\varepsilon_1$ ratio dramatically decreases and reaches to approximately zero until the fracture within the sharp, local neck [37]. Therefore, $d\varepsilon_2/d\varepsilon_1$ ratio within the strain-localized regions should be an indicator to classify them as local necks. The evolution of $\varepsilon_2/\varepsilon_1$ ratio during testing is plotted for five testing conditions in Fig. 3.3. The values of the true major and minor strains are the averages over the 1-mm area centered on the localization regions where the equivalent strains are the maximum. The purpose of averaging the strain over an area is to eliminate local disturbances in the strains. Both materials deform with the predetermined strain ratio until the fracture without significant deviations. The deviations at the very beginning of the test quickly diminish, and the strains increase linearly, resulting in a constant ratio. There is no sudden increase in the major strain as the test progresses and the initial, preset strain ratios remain undisturbed until the fracture, proving the lack of local necking. This is especially important for the DC-04 steel, which is known to develop necks before the fracture. While the absolute values of the β can sometimes deviate from the target β (e.g., $\beta = 0$ and 1 for the steel), the strain ratio remains fixed after the test reaches steady state.
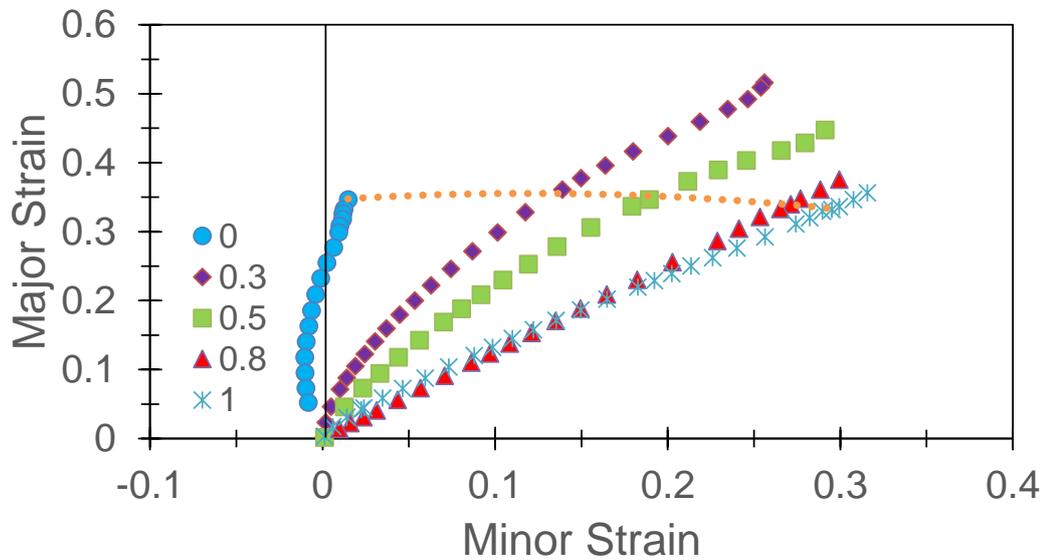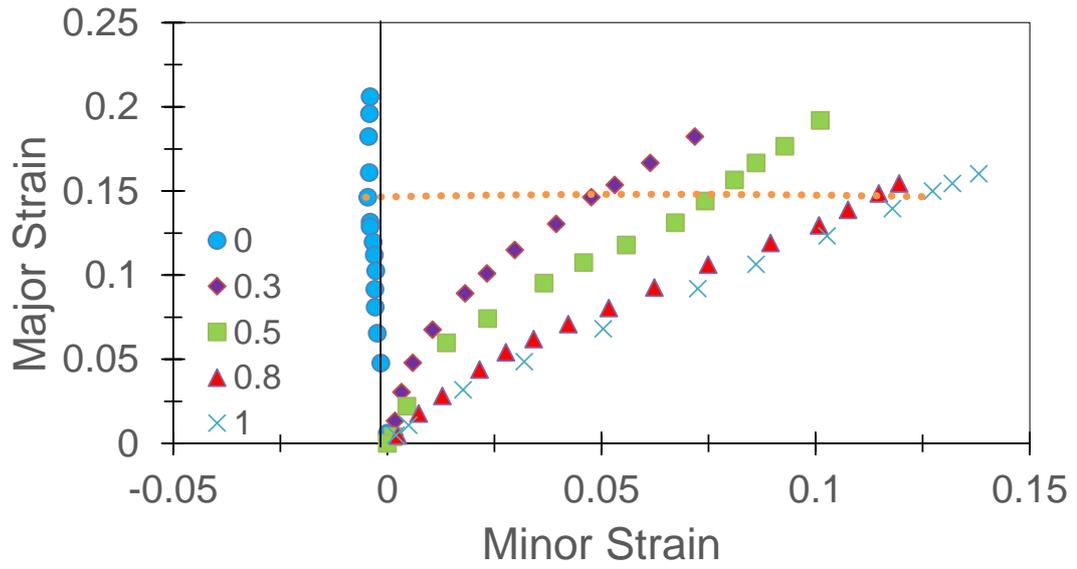
Figure 3.3. Evolution of major and minor strains in the 1-mm area centered on the localization of Al 6061-T6 (top) and DC-04 steel (bottom) samples. The preset strain ratios are again preserved until fracture. Dashed lines are the forming limits obtained by the TRM.

3.3.2. Forming Limits with and without Local Necking

The ISO standard and strain rate methods for FLC detection are sensitive to the increase in major strain over the minor. They are designed to capture this increase to determine the onset of necking. When applied to the Nakajima test, the ISO method

determines the forming limits from the local necks by the line method (Fig. 3.4.). To compare the forming limits obtained in both tests, the ISO method was implemented to the cruciform results. Due to the lack of local neck, the strain localization regions were evaluated. Similar to the Nakajima test, the image before fracture was recorded and five lines were drawn perpendicular to the localization region and strain data was obtained throughout these lines (Fig. 3.4.). The major and minor strains were determined by the polynomial fit performed on the strain data through the lines. Figure 3.8. compares the forming limits obtained for both tests. The ISO method is clearly not suitable to the cases without local necking as there is a large mismatch in the limiting strains. Only the equibiaxial condition results in similar strain but the deviations increase as the strain ratios approach to the plane-strain, where the local neck formation is the easiest in the Nakajima. Forming limits in the cruciform tests resemble fracture behavior rather than forming.
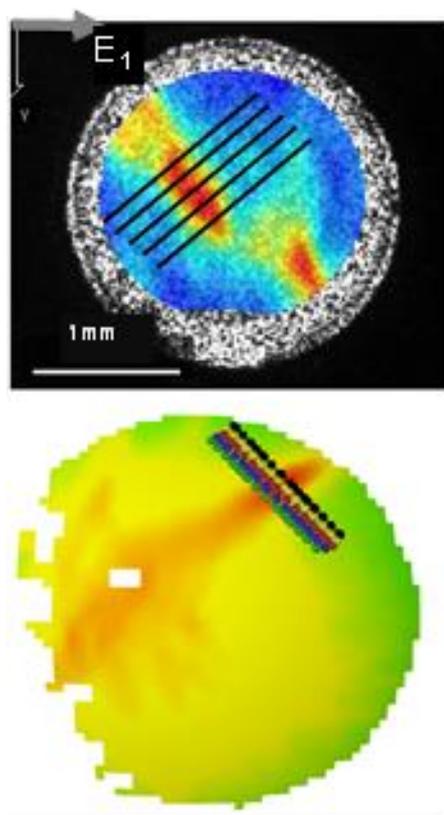
Figure 3.4. Application of the ISO standard to DC-04 steel at equibiaxial.

32

As an alternative to the ISO method, M-K model can be applied for determining forming limits but further improvements are needed for conditions without the local neck so, the further improvements were conducted and on the M-K model, and there are some differences between the M-K model and TRM. In a treatise of the classical M-K model, the increment of the plastic thickness strain ratio between the local neck and the neighboring regions (($\Delta\varepsilon_3^p$)^{neck}/($\Delta\varepsilon_3^p$)^{neighbor}) can give the intensity of the localization and enable the detection of the forming limits [49]. The ratio has to reach a critical value for severe thinning within the neck, and the major and minor strains at this value become the forming limits [49]. In practice, the critical value ranges from 7 [50] to 10 [49].

When applied to the local necks, the M-K model compares the strain within the neck and the immediate neighbors. As the necks are severe localization regions, there is a sharp contrast between the neck and the adjacent areas. In the cruciform test, the maximum strain gradually decreases from the localized regions to the surroundings. Therefore, TRM compares between the regions accumulating the maximum ($\Delta\varepsilon_3^b$) and minimum ($\Delta\varepsilon_3^a$) thickness strains ($\varepsilon_1 + \varepsilon_2 = \varepsilon_3$) throughout the whole test region which should represent the severity of localizations more accurately (Fig. 3.1.). In addition, the increment of the total thickness strain ratio is used for the localizations instead of the plastic thickness strain ratio. Figure 3.5. shows the change in ($\Delta\varepsilon_3^b$)/ ($\Delta\varepsilon_3^a$) during the cruciform test. The ratio is relatively stable at the beginning and exponentially increases as the localization becomes severe. The critical parameter is selected as ($\Delta\varepsilon_3^b$)/($\Delta\varepsilon_3^a$) $\approx$ 7 for severe localizations and the corresponding forming limits. Thus, while the original M-K model was originally developed for the local necks, TRM is suitable to measure the severity of any localization or instability. In other words, TRM could be applied both deformation with or without local neck since it investigates the critical level of strain localization whether in the local neck or not.
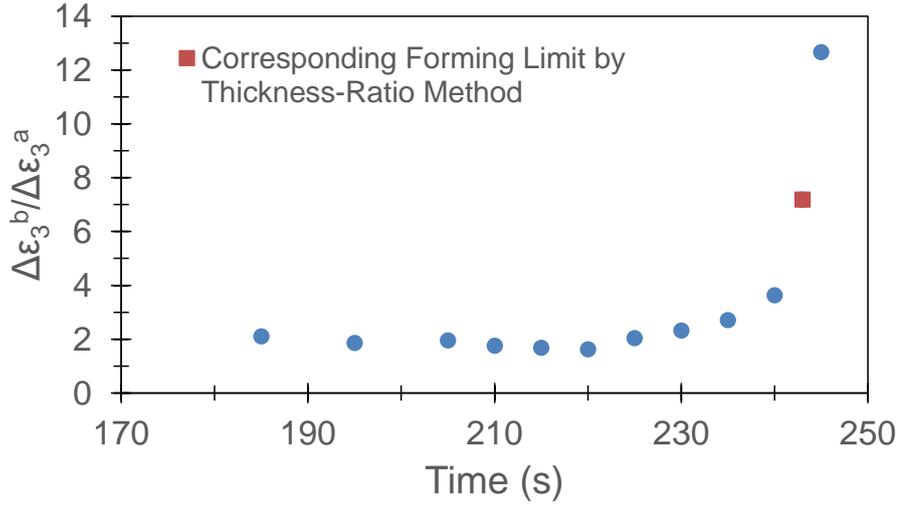
Figure 3.5. Forming limits of Al 6061-T6 at β=0.8 by TRM.

For the cruciform test, the limiting strains were determined from the strain maps at the critical thickness-ratio (Fig. 3.5. – red square). The principal strains were again averaged over the 1-mm area centered at the maximum equivalent strains (Fig. 3.1.), to eliminate microstructure or DIC error related excessive local deformations. This also enabled a fair comparison to the macro-scale local necks developing in the Nakajima test. The dashed lines in Fig. 3.3. represent the forming limits of the test materials at various *β*. The thinning of the sample is uniform until the critical thickness-ratio. After this point, strain localizations become severe and independent of their location, i.e., outside or inside the sample center, they will disturb the thickness uniformity. The major and minor strains inside the center continue to increase with the fixed ratio until the sample fails from the localized region (Fig. 3.3.). Due to its higher strain hardening ability and strain rate sensitivity, the steel accumulates higher strains than aluminum after its forming limit.

For the Nakajima test, the critical parameter was again selected as $(\Delta\varepsilon_3^b)/(\Delta\varepsilon_3^a) \approx 7$ for severe localizations and the corresponding forming limit. In this case, ε_3^b was the maximum strain in the local neck, and ε_3^a was the minimum strain elsewhere in the

sample. The maximum strain was averaged over few data points to eliminate errors from the DIC measurements. Figure 3.6. compares the forming limits obtained by the TRM. Forming limits almost overlap in both tests, with minor deviations (~ 15%) at the strain ratios close to the plane-strain. Although the surface finish of the specimens used for the cruciform test is worse than the sheet used for the Nakajima test, similar forming limit curves are obtained. The limiting strains at smaller β are slightly higher in the cruciform test, as the suppression of local neck becomes more important for these strain paths. Overall, TRM results in smaller forming limits compared to the ISO method. The ISO determines the forming limits just before fracture, whereas TRM determines them in such way that severe localization takes place in a particular region compared to the other locations in the sample. Therefore, the limits determined by the TRM are not FLCs, but rather a conservative estimate for uniform deformation. It applies to the cases with or without local necks for the both type of materials. The thickness control method developed by the study of [5] also results in lower limits compared to the ISO method but is shown to be universally applicable to the cases with multiple local necks.
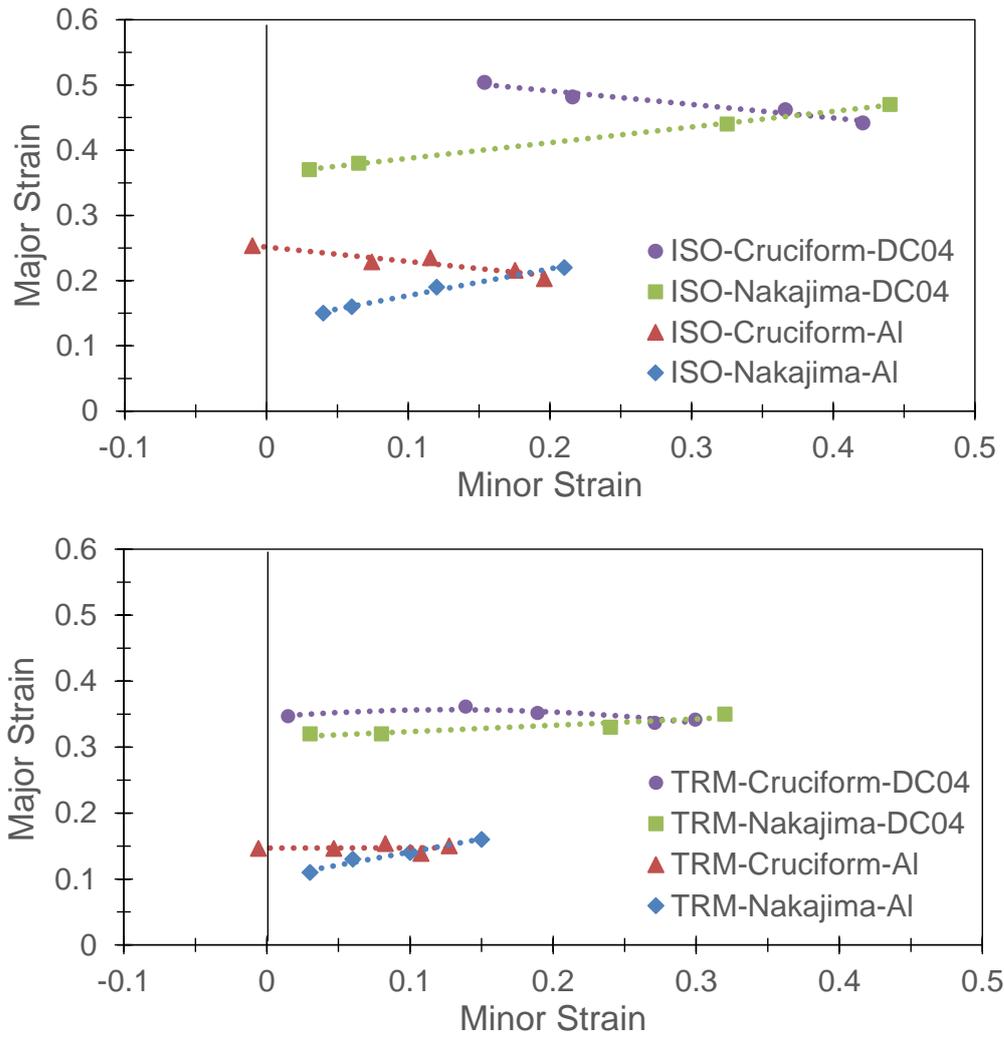
Figure 3.6. Comparison of forming limits of Al 6061-T6 and DC-04 steel using the ISO method (top) and TRM (bottom).

3.3.3. Fracture Limits with and without Local Necking

A rather universal method in establishing the limits in forming is to measure the fracture strains. Unlike the FLCs, the study of [51] indicated that fracture strain is a material property. The study of [52] showed that it depends on the strain path and the stress triaxiality ratio ($\sigma_H/\bar{\sigma}$) but it is insensitive to the geometrical imperfections in the material that can lead to the instabilities like local necking. Assuming the $\sigma_H/\bar{\sigma}$

and β remaining constant during the deformation, the study of [51] derived a constant damage parameter as a function of the anisotropy ratio (r) and the fracture strains:

$$D_{critical} = \int_0^{\bar{\varepsilon}_f} \frac{\sigma_H}{\bar{\sigma}} d\bar{\varepsilon} = \int_0^{\varepsilon_{1f}} \frac{(1+r)}{3}\left(\frac{\beta+1}{\beta}\right) d\varepsilon_1 = \frac{(1+r)}{3}(\varepsilon_{1f} + \varepsilon_{2f}). \qquad (3.2.)$$

According to the study of [52], the material also fails at a constant thickness strain, leading to a straight fracture line with a slope of -1 in the $\varepsilon_1\varepsilon_2$ space, since $\varepsilon_{1f} + \varepsilon_{2f} = -\varepsilon_{3f}$. In a later study, the study of [51] showed that this slope is shown to be valid for the tensile mode fracture (i.e., right side of the FLD) under linear strain paths (i.e., β is constant during deformation).

The strain ratios are linear within the 1-mm test area in the cruciform test. To confirm whether they remain constant until fracture, strain evolution plots were redrawn for the maximum points in the test area. This time the plots were drawn backwards by recording the frame before the crack initiation and rewinding to the initial frame. The cracks were detected by in-situ imaging of the test area. The corresponding frames for maximum strains were one image and two images before the fracture for aluminum alloy and steel, respectively. The exact location of the crack was marked and the strains were averaged over few data points at the exact crack location, instead of averaging over the whole area. Figure 3.7. confirms the linear strain evolution in both materials before cracking. Only, the path for $\beta = 0$ in the steel is missing, due to premature fracture at the arms of the sample. The dashed lines connecting the maximum points of various strain ratios in Fig. 3.7. correspond to the fracture strains.
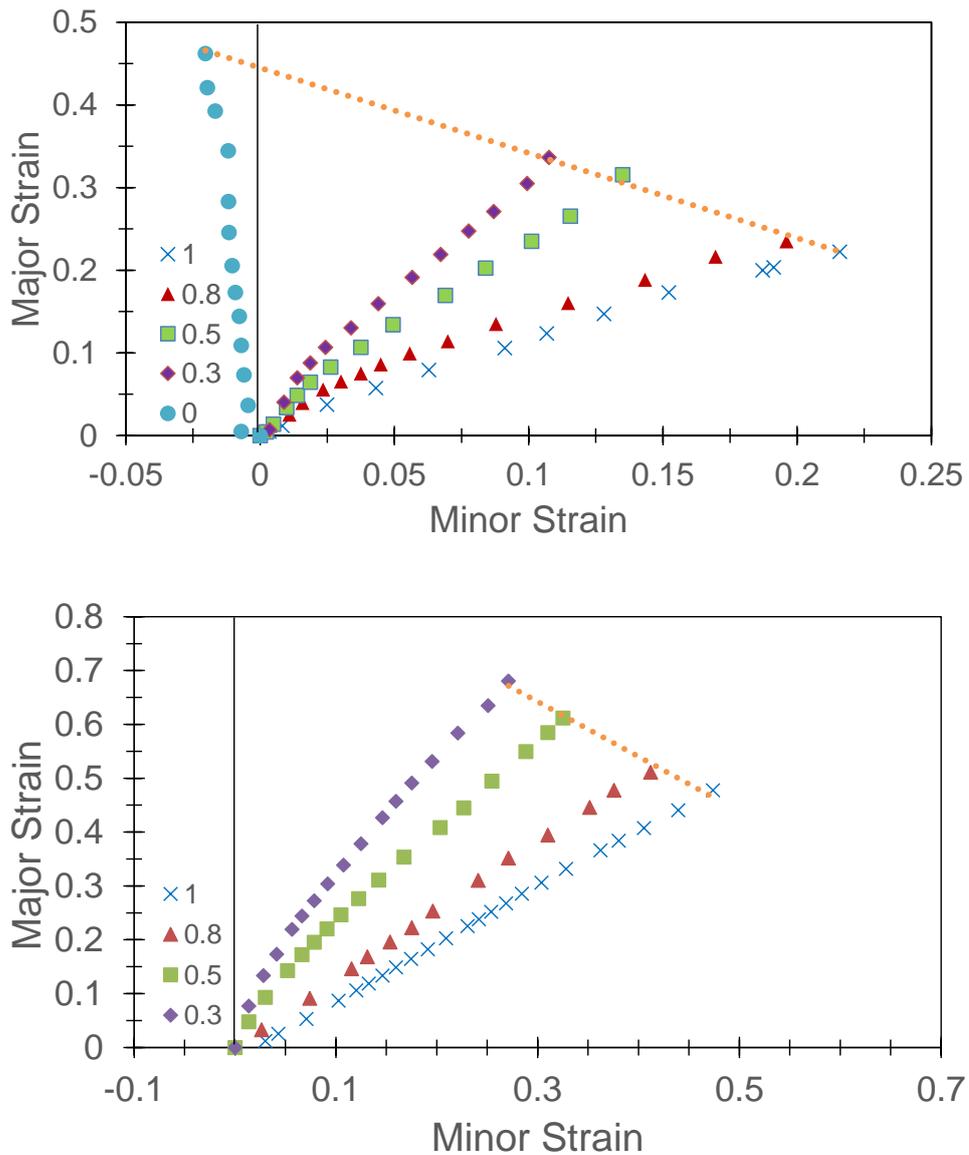
Figure 3.7. Evolution of major and minor strains in the localization regions of Al 6061-T6 (top) and DC-04 steel (bottom) samples. The preset strain ratios are preserved until fracture without a significant increase of major over the minor strain. Dashed lines are the fracture limits.

When the same procedure was applied to the Nakajima test, strain evolutions resulted in non-linear strain paths as expected. It was still possible to measure the fracture strains in the in-plane and thickness directions with the help of 3D-DIC. As the measured thickness strain was confirmed to be the sum of the in-plane strains, the in-

plane strains are reported for comparison with the cruciform strains (Fig. 3.8.). The fracture strains in the cruciform are higher and only the equibiaxial ratio yields in somewhat similar strains to the Nakajima. The fracture limits in cruciform also follow a straight line with a slope of -0.98 for aluminum and -0.96 in steel, as predicted by Equation 3.2. However, the slopes of the fracture lines are far away from -1 in Nakajima, approaching to nearly 0 in aluminum. This shows the inapplicability of Equation 3.2. to the cases with local necks. It is hard to measure reliable fracture strains in the Nakajima as the local necks result in an abrupt change in the ratios. Determination of fracture limits become also challenging in Nakajima for relatively brittle materials like aluminum (Fig. 3.8.), as the sheet cracks soon after the local necking.
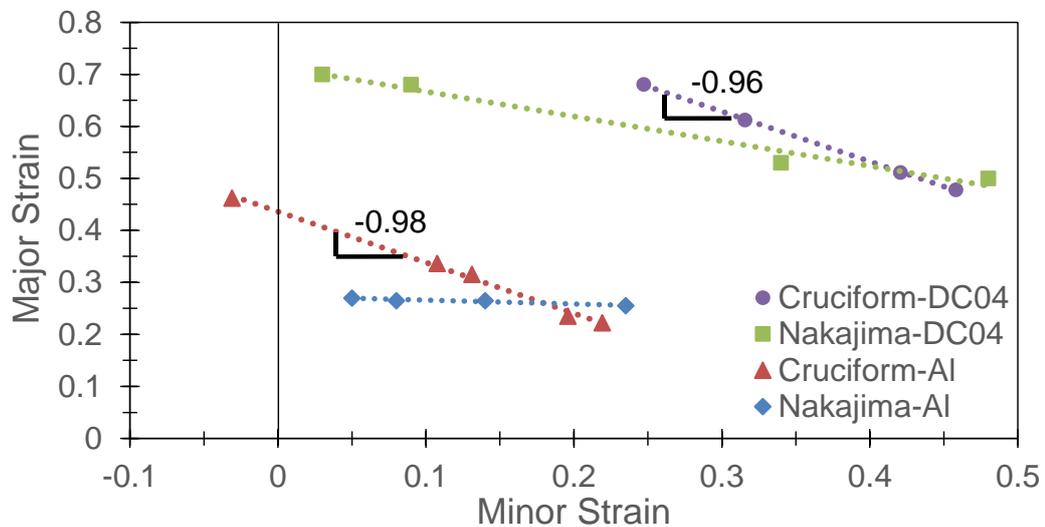
Figure 3.8. Comparison of fracture limit curves of Al 6061-T6 and DC-04 steel with regards to Cruciform and Nakajima tests.

The straight fracture lines obtained in the cruciform test yields constant thickness strains independent of the strain path (Table 3.2.). This is parallel to the predictions of Equation 3.2., but it may seem to contradict the stress triaxiality dependence of the

fracture strains. When the in-plane strains are converted to the equivalent strain with the following equation:

$$\bar{\varepsilon} = \sqrt{\frac{2}{3}\{\varepsilon_1^2 + \varepsilon_2^2 + [-(\varepsilon_1 + \varepsilon_2)]^2\}} \tag{3.3.}$$

triaxiality dependence becomes apparent as indicated in [53] and Table 3.2. This proves the feasibility of the cruciform test in measuring the actual fracture strains of both materials. Such relations do not hold in the Nakajima test due to the nonlinear strain paths.

Table 3.2. *Fracture Strains of Al 6061-T6 and DC-04 Steel*

β	Triaxiality Ratio	Al 6061-T6		DC-04 steel	
		Eq. Strain	Thickness Strain	Eq. Strain	Thickness Strain
0	0.577	0.52	0.43		
0.3	0.638	0.46	0.44	0.96	0.93
0.5	0.655	0.46	0.45	0.94	0.93
0.8	0.665	0.43	0.43	0.93	0.93
1	0.667	0.44	0.44	0.94	0.94

3.4. Conclusion

The cruciform biaxial tension test was shown as an alternative to the Nakajima test when determining the forming and fracture strains of the materials deforming without a local neck. Suppression of local necking in the cruciform test was possible due to the unique deformation characteristics and sample geometry. The cruciform design led to the diagonal strain bands intersecting at the sample center and allowed the test region to deform without any deviations from the preset principal strain ratio. Strain localizations occured along the strain bands due to the defects in the material. Contrary to the plane-strain deformation in the local necks, the preset strain ratio did not change in the localized regions.

When applied to both tests, the ISO method failed to measure the forming limits in the absence of local necking. As an alternative, a method (TRM) was developed to determine the intensity of the localizations. The ratio of thickness strains in the regions having the maximum and minimum equivalent strains reached to a critical value and limits the formability of materials due to severe thinning in the localization regions. The TRM was applicable to both tests (i.e., two types of instabilities) and both materials. While the limits were lower than the FLCs obtained by the ISO method, they were useful as universal estimates for uniform deformation.

The suppression of local necking benefited the measurement of fracture strains. The linear strain ratios in the cruciform test resulted in constant thickness strains independent of the strain paths, as suggested by the damage criterion. Moreover, equivalent strains before fracture were consistent with the $\bar{\varepsilon}_f$ $vs.$ $\sigma_H/\bar{\sigma}$ relations. Development of local necking in the Nakajima test prevented these measurements. The measured fracture strains were far lower than the actual fracture strains, especially for a relatively brittle material like aluminum.

Overall, the above listed features of the cruciform test could be useful for investigations of the material behavior under certain strains paths and large strains. It was possible to reach the actual fracture limits in the cruciform test without deviating from the target strain ratio. The test material likely developed the localizations due to the inconsistencies in the microstructure as opposed to the geometrical imperfections. This might reveal the relationship between the microstructure and the forming behavior under large strains, which could be especially useful for materials with complex microstructures (e.g., lightweight alloys, dual-phase steels).

CHAPTER 4

GRAIN-SCALE HETEROGENEITIES CONTROLLING THE MACRO-SCALE STRAIN LOCALIZATIONS

4.1. Introduction

Polycrystalline metals often exhibit non-uniform deformation behavior, which can be observed at different length scales. For macro-scale, non-uniform strain localizations are usually related to the variation in thickness or other geometrical instabilities that result in necking [37]. However, for meso-scale or micro-scale, strain localizations are related to the microstructural imperfections that lead to the non-uniform deformation. Heterogeneous microstructures are responsible for non-uniform strain localization at these scales. Some of the most critical features of a heterogeneous microstructure are crystallographic texture, grain size, and shape, etc. [54]. Thus, it is essential to know the relation of accommodated macroscopic strain with the grain-scale strain distribution [55].

Researchers study the effect of these microstructural features on macro- or meso-scale strain localizations using multi-scale models due to the difficulty of experimental investigations [56]. Multi-scale models are presented to bridge the micro-scale strain distribution to the macro- or meso-scale strain distribution [57]. Computational homogenization approaches, which are the methods of multi-scale models, are mostly used since they consider complex microstructural features and evolving microstructures, etc. [58]. In this method, the microstructure of the material is regarded in a Representative Volume element (RVE) [59]. RVE is a confined model of the microstructure, which consists of grains separated by the grain boundaries with relevant microstructural details. These details are morphology, constituent material properties, presumed damage initiation and evolution mechanisms, voids, inclusions,

cracks, different phases, etc. [60]. There are some studies using RVE to see the effects of aforementioned micro-scale parameters on macro-scale behaviors such as failure initiation [61], stress and strain distribution [59], formability [62], and location of strain localization band [56].

On the other hand, an experimental study, which is about the relation of strain distribution at different scales, is deficient in the literature. The experimental studies at multi-scale strain measurements have been done so far do not focus on the same regions of the sample. Both macro- and micro-scale observations are conducted in different regions of the sample due to the usage of two setups of imaging. Therefore, they compare the strain localization behavior in different regions, and each region represents a different scale [19], [20], [63]. Therefore, the strain localization behavior of a given region of the sample has not been investigated at different scales. In this chapter, the strain distribution in the same region is investigated at both micro- and meso-scales in order to bridge both scales and to test the qualitative and quantitative effects of micro-scale strain heterogeneities on the macro-scale localizations.

4.2. Materials and Methods

The test setup, the properties of Aluminum 6061-T6, the cruciform design, and imaging setup were stated in chapter two. In addition to meso-scale DIC, the micro-scale DIC is conducted. The corresponding field of views was obtained as 2.9 x 2.2 mm^2 at 3X magnification and as 440 x 330 µm^2 at 20X magnification for meso-scale and micro-scale investigations, respectively. The images were captured with 1 fps for meso-scale and 5 fps for micro-scale at a deformation rate of 0.5 mm/min. Some images were selected for incremental type DIC analysis, which had a subset size (radius due to circular subset) and step size of 80 and 10 pixels, respectively. The spatial resolution was obtained as 1.2 µm/pixel and 0.18 µm/pixel for meso-scale and micro-scale, respectively. Therefore, at least two subsets were located in a grain. The maximum strain error calculated by rigid body translation was 0.14% and 0.18% for meso-scale and micro-scale, respectively.

The pit region was electro-polished and electro-etched with Struers Lectropol-5 device, and the solution used was Struers A2 (90 ml distilled water, 730 ml ethanol, 100 ml butoxyethanol, and 78 ml perchloric acid). Electro-polishing and electro-etching parameters were 38 Volts for 30 seconds and 18 Volts for 10 seconds, respectively. After the process, a proper pattern was obtained for both meso-scale and micro-scale investigations.

The test procedure is illustrated in Fig. 4.1., and it was conducted in five steps; Step I: first-stage of deformation at meso-scale, where the testing started with stretching of the sample until apparent plastic deformation had occurred. Then, the DIC technique was applied. According to the meso-scale DIC results, the region to be examined at the micro-scale was determined. This region, shown in Fig. 1(b) as a rectangle, consisted of two sub-regions, with one region having strain localization. In other words, the left side of the region accumulated large strain while the right side of the region accumulated considerably lower strain. A distinct transition of strain distribution separates the sub-regions. The dimensions of these sub-regions were determined by precise measurements. Step II: Objective change to zoom-in to the selected region-of-interest (ROI). The test was paused during this step. Step III: second-stage of deformation at micro-scale, where the ROI was examined at micro-scale and deformed further until apparent deformation was observed. Step IV: Objective change for zoom-out. The test was paused during this step. Step V: Test was stopped and the difference in the patterns represents the second-stage of deformation at the meso-scale. To sum up, the sample was deformed in two-stages, where the meso-scale analysis was done for both stages and the micro-scale analysis was done for the second stage only. Thus, the required images of both scales were obtained for DIC from the same region. There were two different deformation stages (Stage I and III), and the total deformation was up to 0.077 true strain. Overall, four tests were conducted; two of them were under uniaxial strain path and the other two were under equibiaxial strain path.
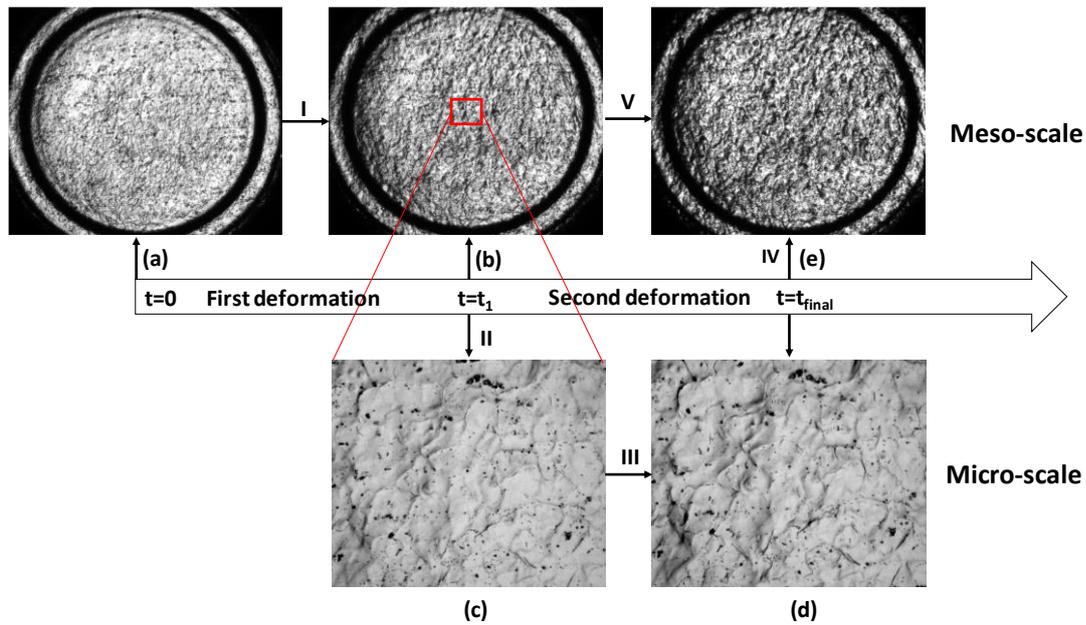
Figure 4.1. Illustration of the test procedure: (a) undeformed specimen before the test, (b) first-stage of deformation at meso-scale, (c) micro-scale region-of-interest after the first-stage, (d) second-stage of deformation at micro-scale, (e) meso-scale after the second-stage.

4.3. Results and Discussion

The experiment results of both micro- and meso-scales are shown in Fig. 4.2. and 4.3. for uniaxial tension and equibiaxial tension conditions, respectively. The strain values of all tests are calculated as the mean true strains and listed in Table 4.1. The specimens for the four tests are named as 'Uni-1, Uni-2' and 'Bi-1 and Bi-2' according to the loading condition. The former represents uniaxial tension condition, and the latter represents equibiaxial tension condition.

In the macro-scale result of Uni-1, the left part of the ROI accumulates more strain than the right one, resulting in a strain localization at the end of the test. Similarly, at the micro-scale, left part of the ROI contains more strain-localized spots compared to the right part. As the test progresses, grain-scale heterogeneities concentrate to the left part of the ROI, leading to the strain contrast at the end of the test. Based on these visual observations, it is apparent that the micro-scale heterogeneities have some

46

effect on both initiation and development of the strain-localized regions at the global scale. To reach quantitative conclusions, the amount of strain accumulated at the meso-scale is found by subtracting the mean strain at Step IV from Step I. The accumulated strain at the meso-scale is then compared with the mean strain at the end of Step III, which is strain accumulated at the micro-scale. The values nearly equal at each part of the ROI at both scales (Table 4.1.), proving that the strain heterogeneities at the micro-scale are reflecting themselves at the global scale almost identically. These heterogeneities are originating mostly from local orientation differences between the grains and they are the sources for large-scale strain localizations.
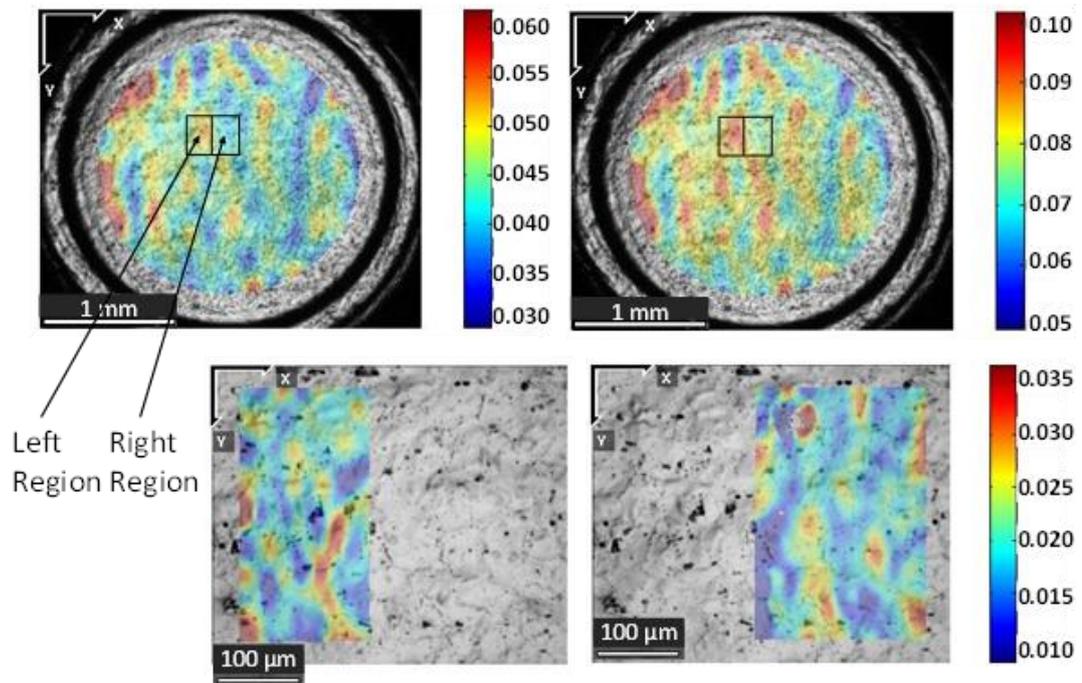
Figure 4.2. Multi-scale DIC results of Uni-1 sample under uniaxial tension. Upper left image is the strain analysis at the meso-scale for the Step I. The sub-regions are separated by a line in the rectangular box. Upper right image is the strain analysis at the meso-scale for Step V. Lower images are the strain analysis at the micro-scale for Step III.

When each test is considered separately, the largest and lowest deviations between the accumulated strains at each scale are 0.6 % and 0.1 % as true strain, respectively. The

maximum calculated strain error is 0.18%, and this value can be significant in such a low strain. In order to show that the strain distributions observed at both scales are consistent with each other, the ratio of the strain accumulated in each part of the ROI are calculated and compared for each scale (Table 4.1.). The ratio shows the amount of strain localization in the ROI, as one part of the ROI always accumulates more strain than the other. The ratio is remarkably consistent at each scale for all the tests (Table 4.1.). The deviation between the ratios of the strain values at micro- and meso-scale is about 6%. This result confirms the grain-scale strain distributions as the sources of strain-localizations at both scales since the strain localization is defined as the ratio of strains between two neighboring regions.

In equibiaxial condition results, shown in Fig. 4.3., the same trend is observed. According to these results, there are two apparent regions, where one accumulates larger strain while the other accumulates lower strain. This distribution can also be observed at both scales. In this case, the strain distribution is more homogenous in each part of ROI at the meso-scale, yet the strain localizations are evident at the micro-scale. This shows the strain localizations are still present at the grain-level even if they are not apparent at the larger scale. In other words, one should consider micro-scale features such as grain size distribution, crystallographic texture, type and behavior of grain boundaries, precipitates, second-phase particles, etc. while considering strengthening and hardening mechanisms when meso-scale strain distributions are desired to be investigated.
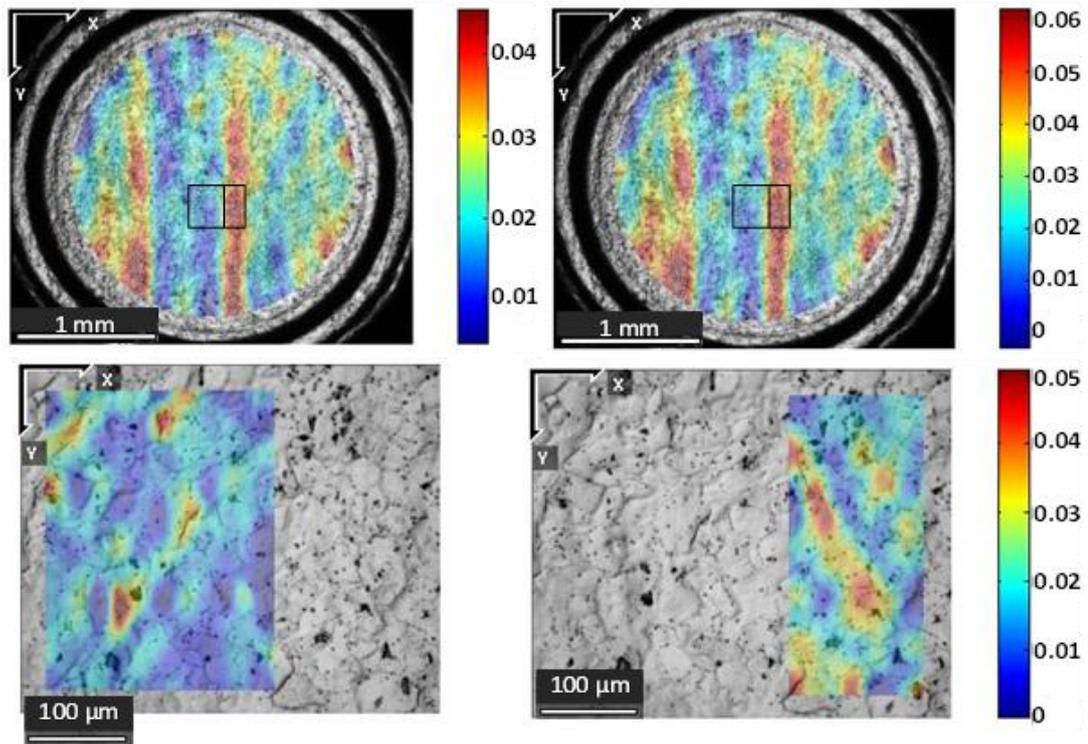
Figure 4.3. Multi-scale DIC results of Bi-1 sample under equibiaxial tension. Upper left image is the strain analysis at the meso-scale for the Step I. The sub-regions are separated by a line in the rectangular box. Upper right image is the strain analysis at the meso-scale for Step V. Lower images are the strain analysis at the micro-scale for Step III.

The size of sub-regions at micro-scale should be representative to observe the same strain distribution at meso-scale. When comparing the experimental and numerical studies in the literature conducted on RVE so far, one can see the former one is limited in quantity. There should be an optimal size of RVE, and it depends on the microstructure of materials and grain size. The size determination of RVE for aluminum alloys has not been conducted experimentally, yet. On the other hand, RVE size can be determined experimentally for other metals such as 170 µm for low carbon steel, 100 µm for titanium [20], [63]. In these studies, the number of grains located to one edge of the RVE is 8.85 and 3, respectively. The total number of grains is 694 and 27, respectively. The number of grains in RVE is important to determine the size, and there is a strong connection between the grain size and the size of RVE since RVE

must contain sufficient information about the microstructure. In this chapter, the number of grains in the sub-regions is calculated for micro-scale results. The calculation is conducted according to the following equation:

$$N = \left(\frac{R}{\delta}\right)^{3}$$
(4.1.)

where N is the number of grains, R is the window size and δ is the grain size [63].

The investigated region at micro-scale is rectangular, not square. Therefore, the comparison is conducted according to the number of grains located on one of the edges of RVE. The number of grains located on the two edges of the investigated region is listed in Table 4.1. The first number indicates the number of grain located on the shortest edge of the rectangular region while the second number indicates on the longest edge of it. The smallest size contains 2.5 to 5.2 grains, while the largest one contains 4.7 to 6.2 grains. Since there is no RVE size determination experimented for aluminum alloys, a direct comparison cannot be made. However, such number of grains can be assumed as small for the critical RVE size. Despite of this small amount of grains, the strain distribution of both scales is close to each other. Thus, this quantity of grains or the size of RVE provide sufficient information to observe the micro-scale strain localization behavior at the meso-scale.

Table 4.1. *Strain values at both scales under uniaxial and equibiaxial tension conditions (values are true strain in percentage)*

	Step I (meso-scale)		Step IV (meso-scale)		Difference in meso-scale values		Step III (micro-scale)		The ratio of the strain values		Number of grains on the edge of the ROI	
	Left	Right	Left	Right	Left	Right	Left	Right	Meso	Micro	Left	Right
Uni-1	4.9	3.9	7.7	6.3	2.8	2.4	2.2	1.9	0.857	0.864	2.8-6.2	3.8-6.2
Uni-2	1.3	3.0	2.8	5.3	1.5	2.3	1.3	1.9	0.652	0.684	2.5-5.9	3.4-5.9
Bi-1	1.0	3.6	1.6	5.0	0.6	1.4	1.0	2.0	0.423	0.500	4.7-6.2	2.8-6.2
Bi-2	1.7	2.9	3.4	4.9	1.7	2.0	1.6	1.8	0.850	0.889	2.5-5.2	3.5-5.2

4.4. Conclusion

In this chapter, strain distributions at multiple-scales were investigated in the same region of an aluminum sheet. The region of interest was imaged and analyzed at two scales with 7x difference in magnification and resolution. The ROI at the meso-scale was chosen in a way that it contained strain localization. The origin of this localization was confirmed to be microstructure features and strain localized spots through the micro-scale analysis. Moreover, the amount of mean strains and the intensity of strain localizations were remarkably similar at each scale, showing a quantitative relation between two scales as well as the qualitative match. These results highlighted the importance of grain-scale features controlling the non-homogeneous strain distribution behavior at the larger, global scales.

CHAPTER 5

MICROSTRUCTURAL ORIGINS OF STRAIN HETEROGENEITY AND STRAIN DISTRIBUTION PREDICTION

5.1. Introduction

The formability of sheet metals is not only related to macro-scale mechanical properties and boundary conditions but also related to the microstructure of the metals. Macro-scale deformation heterogeneities are generally related to the microstructure of the metal [64]. Therefore, the microstructural features have an essential role of deformation heterogeneity since the local strain distribution can be heterogeneous in a macro-scale homogeneous polycrystal deformation. Researchers investigate how the distribution of grains and the interactions between them affect the deformation behavior. Grain size affects the deformation [65], [66] according to the Hall-Petch equation [67], [68]. These studies investigate the effect of the average grain size of polycrystalline metals on deformation behavior. The heterogeneous grain size distribution in polycrystalline metals result in heterogeneous deformation. In the study of [64], a large grain in an aluminum oligocrystal localizes the large strain, and this softening is explained by the Hall-Petch effect. It is explained that this grain has a relatively low amount of grain boundaries in order to serve as barriers for dislocation motion, so there is a lack of constraining effect from dislocation motion. However, a decrease in grain size increases dislocation density resulting in large strain accumulation [69], [70]. Grain boundaries have non-negligible effects on formability while they accumulate the larger strain mostly during deformation [54], [55]. Another study indicates that orientation mismatch between the grains causes stress concentration near the grain boundaries [71]. Triple junctions existing in the polycrystalline microstructure may accumulate the largest strain among the grain boundaries [15]. The increase in the fraction of triple junction increases the ductility

and decreases the strength of metals [72]. Some researches also focused on the role of grain boundaries on strain heterogeneity. The high-angle grain boundaries in bicrystals induce dislocation pile-ups and accumulate dislocations in front of grain boundaries, which result in local hardening leading to strain heterogeneity [73], [74]. However, in most of the random textured polycrystalline metals, 90% of grain boundaries existed as the high-angle boundaries [75], so the effect of grain boundary misorientation become negligible. According to the study of [76], there is no correlation between grain boundary region hardening and angle of boundaries (grain to grain misorientation) in polycrystalline aluminum. Moreover, there is no effect of morphological orientation of grain boundaries with respect to the external loading direction on strain heterogeneity [77].

Slip transmission takes a role in strain heterogeneity. The grain boundaries allowing slip transmission contribute to strain localization on both sides of the grain boundary while, on the contrary case, strain localizes to one side of grain boundaries [78], [79]. In addition to the intergranular misorientation effects, the intragranular misorientation has effects on strain heterogeneity. The intragranular misorientation has an effect on the deformation homogeneity of polycrystalline metals on the condition that the investigated number of grains is small [80]. Besides, their effects decrease when the number of grains increases.

The other parameter affecting heterogeneous deformation behavior is neighbor grains. However, the orientation of the grain has a more significant effect than the neighbor grains on heterogeneity [81]. Another study shows that neighbor grains do not seem to have a strong influence on the deformation behavior of an individual grain [82]. Thus, the grain orientation is the critical parameter for the dislocation structure, causing the strain distribution, while grain boundary and grain size are the minor parameters affecting it [83].

The crystallographic texture of the grains affects the strain localization directly [14]. Distribution of grains with different orientations with respect to loading direction can

provide heterogeneity in deformation [84]. There are some classical orientation based models to predict the heterogeneity, such as the Sachs, Taylor, and self-consistent models. These models are commonly used in numerical analysis named crystal plasticity finite element analysis (CPFEA). The principal considerations of these models are the initial orientation of grains and its effects on active slip systems and lattice rotations [85]. In the Sachs model, the accumulated stress in each grain is assumed as the same and equal to the external stress. In addition, one slip system (the slip system with the maximum Schmid factor [86]) is required to accommodate plastic strain in face-centered cubic crystals (FCC) [87]. It is assumed that this model is only suitable for single crystals under uniaxial tension [88]. On the other hand, in the Taylor model, the accumulated strain in each grain is assumed as the same and equal to the external strain [89]. Moreover, in FCC, 5 of the 12 slip systems are required to accommodate plastic strain. In the self-consistent model, the constraint of neighboring grains is taken into account, and 3-4 active slip systems are required to produce plastic strain [90]. There are also some crystallographic models, mainly based on the Taylor model [91]. Some of them are the viscoplastic self-consistent (VPSC) [92] and the advanced lamel (ALAMEL) [93] models. There are some conflicting studies about the success of these models. To illustrate, according to the study of [94], the most successful model for crystal plasticity for polycrystals is indicated as the Taylor model. However, the study of [82] shows that the Taylor model is successful in predicting average deformation, yet failed to predict local deformation behavior in the individual grain. According to the study of [95], aluminum multicrystal obeys neither the Sachs nor the Taylor model.

Most of the researches mentioned above are conducted numerically, which use a more controlled microstructure, such as having a low number of grains and large grain size with a high fraction of low-angle boundaries. It is not common in a typical polycrystal having a randomly textured microstructure. For instance, the results of bicrystals cannot be directly compared with the investigations in polycrystals [96]. Therefore, experimental investigations are essential to comment on the heterogeneity of strain

localization during deformation. Some researches mentioned above are conducted both numerically and experimentally to compare the results obtained by both approaches. However, the prediction of CPFEA does not match the experimental results [15]. The experimental investigations mostly focus on single features in the microstructure. The study of [14], [97] investigate the relationship between strain localization and grain orientations, while the study of [98] examines the effect of the mean grain size on strain distribution. In addition, the relationship between surface roughening due to local deformation and Taylor factors is observed [15]. The study of [99] show that the relation between the location of fracture nucleation and individual grain orientations. The relationship between lattice rotation and strain distribution is also observed [85], [100]. The study of [80] investigate the effect of intragranular misorientation on deformation behavior, and it is concluded that this effect is considered for polycrystals where the number of grains is small. The relationship between deforming behavior at grain boundaries and grain-to-grain misorientation or lattice rotation is examined by the study of [76], and any correlation between them is not found. On the other hand, the study of [95] examines many parameters, which are grain orientation, the number of activated slip systems, and grain boundary interactions, to comment on strain distribution, but these parameters are investigated in a microstructure consisting of few grains. The common deficiencies in the experimental investigations are considering single features and few grains to examine. In addition, these studies includes only comments on strain distribution behavior. The hypothesis of this chapter is the outcomes from the examination of the reasons behind the strain heterogeneity can be used to predict strain distribution by contributing two methods, named as strain localization indicator (SLI) method and strain localization magnitude (SLM) method. They are generated by the parameters of Schmid factor and grain size. Microstructures used in this thesis are the actual microstructure of a typical Aluminum alloy having a large number of grains, randomly distributed grain size and texture. Thus, in this chapter, experimental investigations are conducted under uniaxial tension to predict strain localization with both qualitatively and

quantitatively. The reasons behind the heterogeneity in strain distribution are established.

5.2. Materials and Methods

The test setup, the properties of Aluminum 6061-T6, and the cruciform design were stated in chapter two. The sample preparation and the DIC parameters for both meso-scale and micro-scale investigations were indicated in chapter four.

The samples were deformed under uniaxial tension. The test setup provided the uniaxial tension condition, where minor strain, ε_2 equals to minus major strain multiplied by Poisson's ratio (0.33) of the material, $-(v^*\varepsilon_1)$ [101]. The meso-scale DIC result was shown in Fig. 5.1., where major and minor true strain values were 31.92% and -11.27%, respectively. The test procedure has two steps. The first one was deforming the sample, and the last one was mapping the orientation of the grains. First of all, the sample was attached to the test apparatus (Fig. 5.2a), and deformed up to a certain deformation pattern (up to 1-2 % strain) that can be observable. This pattern was examined by a meso-scale camera setup (Fig. 5.2b). Then, the test was paused. One of the strain localization region was determined using DIC result, and the micro-scale camera setup was arranged to focus on this region (Fig. 5.2c). After that, the test was continued up to another observation of apparent deformation (Fig. 5.2d). Finally, the DIC was conducted to the micro-scale regions. The test is terminated when the desired results having random strain distribution were achieved by DIC. The field of view of the meso- and micro-scale investigations are 2.9 x 2.2 mm^2 and 440 x 330 μm^2, respectively. The local strain values were calculated by the DIC technique, but the global strain was calculated as true strain by the difference between the diameter of the undeformed and deformed pit regions. Meso-scale image of the whole pit was taken before and after the deformation, and the diameter of the pit was measured at both stages. Thus, the global strain was calculated, and all strain values in this chapter were calculated as true strain. The global strains were 10.92%, 15.50%, 9.55%, 10.03%, and 9.42% for Uni-1, Uni-2, Uni-3, Uni-4, and Uni-5, respectively.
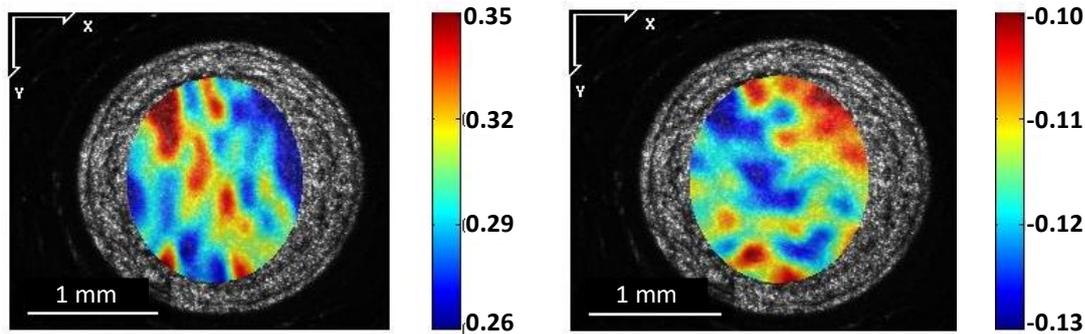
Figure 5.1. The meso-scale DIC test results of major strain (left) and minor strain (right) under uniaxial tension.

In the second step, the sample was unattached from the test setup and was prepared for Electron Back Scatter Diffraction (EBSD) to obtain orientation mapping (Fig. 5.2e). The sample was electro-polished to obtain a proper and flat region for achieving a successful EBSD result. Before that, four indents were applied to the corner of the investigated microstructure to understand the region to be examined after polishing. These indents were applied to a certain distance from the investigated microstructure so that the grains in the microstructure were not damaged. They were still slightly observable after electro-polishing. The electro-polishing was conducted briefly in order not to remove significant parts of uppermost grains of the microstructure, but it was sufficient for diffraction. After obtaining diffraction results, the grain to grain identification was conducted to the microstructure investigated by DIC and EBSD. Finally, the orientation map of the grains was obtained to compare the relation of strain localization with orientation. Now, one can obtain the strain distribution on a grain, and the orientation (Euler angles) of it.
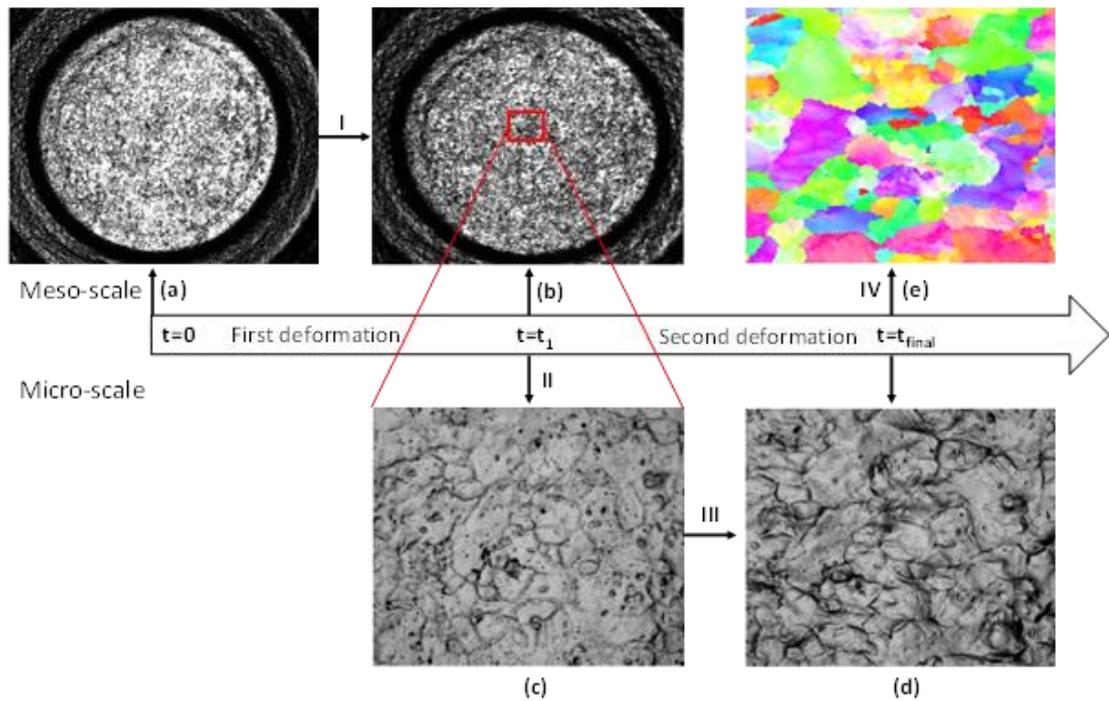
Figure 5.2. Illustration of the test procedure. Undeformed sample (a) was deformed at meso-scale (b) then, the one of the large localization region (red rectangular box) was selected and this rectangular box was further investigated at micro-scale (c). After that, the sample was deformed once more at micro-scale (d). Lastly, the orientation mapping was conducted to this investigated region. The numbers showed the steps in order.

After electro-polishing, the sample was put into NOVA FEI Scanning Electron Microscope via EBSD attachment. The working distance was arranged to 10 mm. The voltage and the spot size were selected as 25 kV and 5.5, respectively. The step size was adjusted 2 microns during diffraction. After diffraction, OIM Analysis software was used for post-processing. Small-sized regions of bad data points, below 5 microns, and data points having less than 0.1 confidence index were eliminated to obtain proper orientation results of each grain. The origins of these bad data points were incapable of obtaining good data points during diffraction since the polishing process was not conducted strongly in order not to remove significant parts of uppermost grains from the surface. Therefore, there were some bad data points needed to be cleaned. The confidence indexes of all five EBSD results were obtained as about 0.29, and the

values were close to each other. After cleaning the results, calculated Euler angles of each grain were exported. Schmid factors of each 12 slip systems were calculated in each grain with respect to the loading direction [86]. Therefore, the orientation and direction of each grain can be obtained using Bunge-Euler angles [102], [103]. The equations used for calculating these parameters were indicated in the Appendices section.

5.3. Results and Discussion

There are five tests conducted under uniaxial tension and four tests conducted under equibiaxial tension. Initially, uniaxial tension test results are investigated. Figure 5.3. shows the micro-DIC and Inverse Pole Figure (IPF) results of uniaxial tension. Strain distribution of all tests is heterogeneous so, they are suitable to investigate the reason for heterogeneous strain distribution. Grain boundary localization is examined, and the localization is observed inside of some grains, which are small-sized and neighbor of these boundaries. The average true strain values calculated by DIC are 8.77%, 13.12%, 7.16%, 8.36%, and 8.50% for the tests named as Uni-1, Uni-2, Uni-3, Uni-4 and Uni-5, respectively so, there is sufficient plastic deformation to investigate.
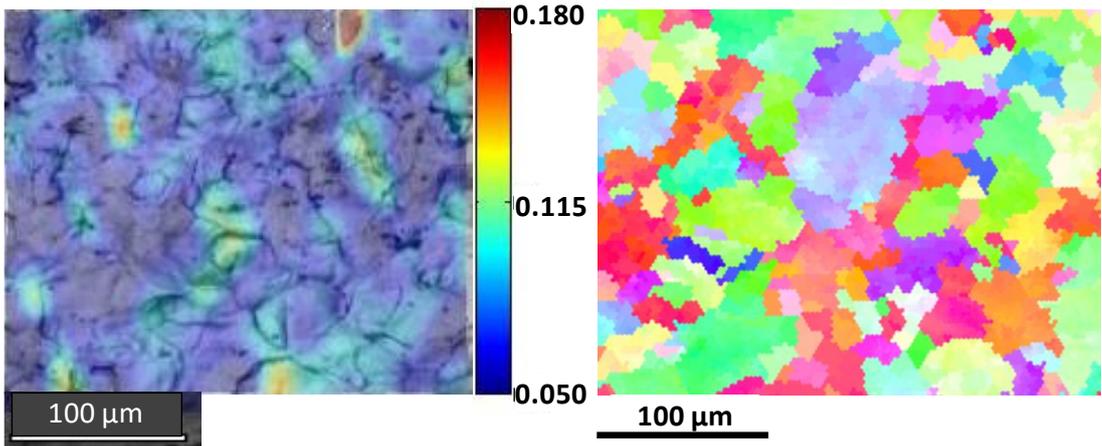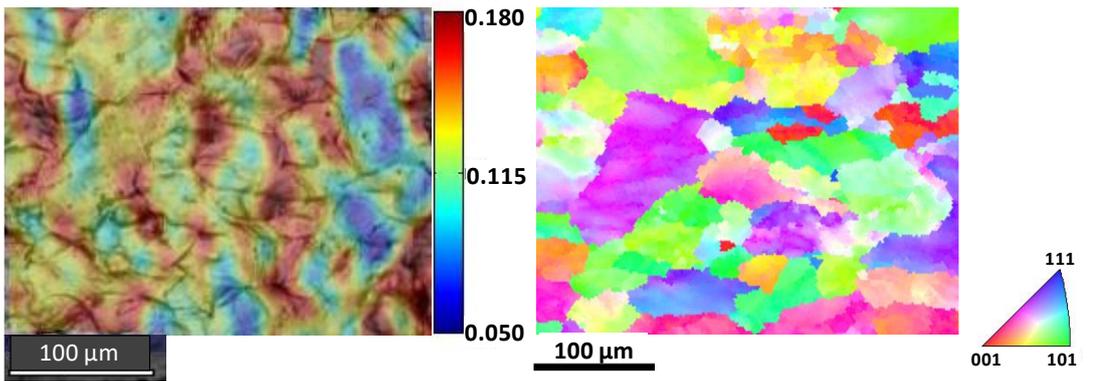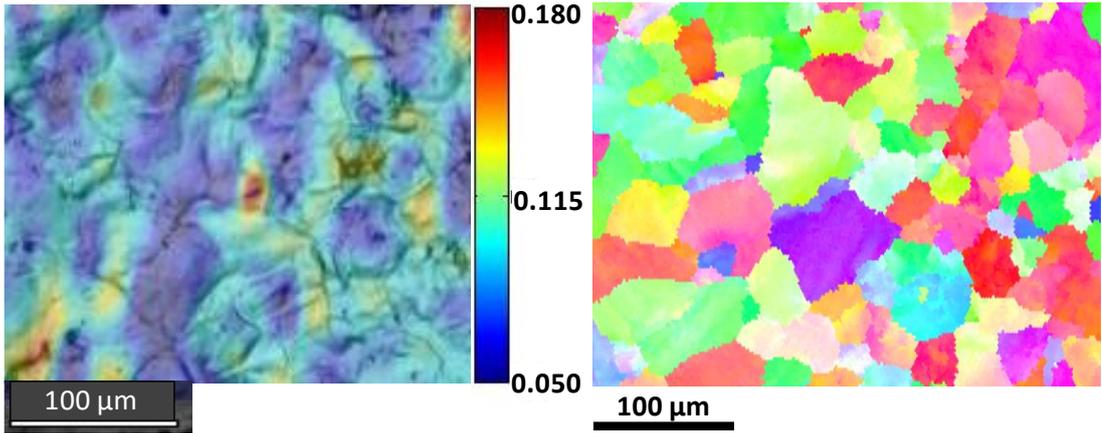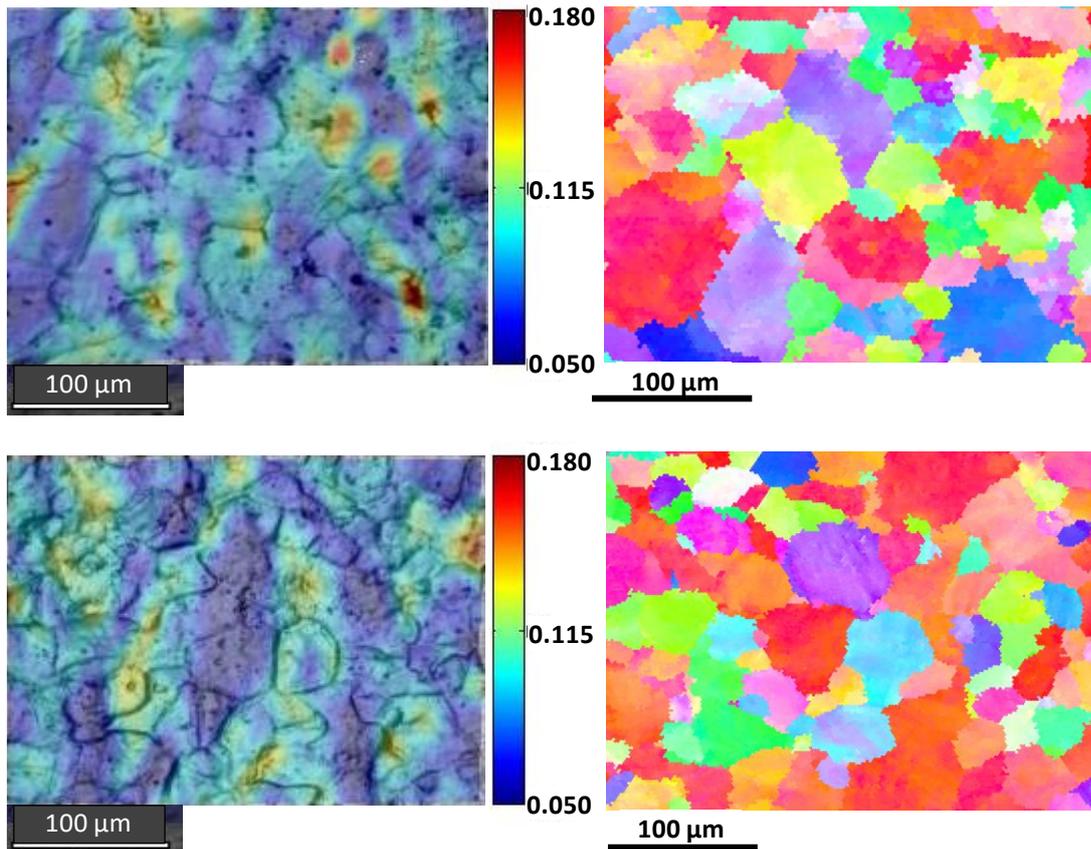
Figure 5.3. DIC results (left) and EBSD results (right) of Uni-1, Uni-2, Uni-3, Uni-4, and Uni-5 shown from top to bottom, respectively. The color indicates the crystallographic orientation of the grains with respect to the normal axis.

In deformation behavior of uniaxial tension, dislocations move through the boundaries where boundaries act as obstacles. In theory, dislocations occur in the activated slip systems, and they move until they meet an obstacle, which prevents the movement. In the case of the absence of obstacles in a grain, this motion occurs until dislocation pile-ups, which take place at grain boundaries [104]. Precipitation hardening in Aluminum alloys may prevent this movement inside of the grain [105]. However, precipitates are distributed uniformly in the material used in this thesis since the hardness of the material is constant throughout the material. Precipitation hardening does not show any evidence on further development since the hardness of the material has not changed for years. Thus, as expected, grain boundary localization is dominant

62

in this chapter. In addition to grain boundary localization, some grains accumulate large strain. They are small-sized and neighbors of these boundaries. The reason for grain localization is that the size of these grains is too small (about half of the average grain size), and strain localization in the vicinity of grain boundaries covers the significant region in these grains.
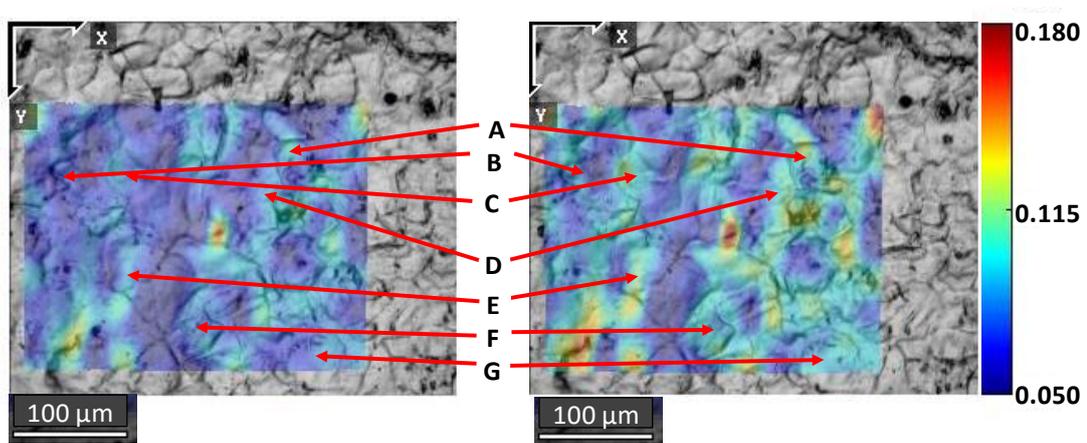
Figure 5.4. Evolution of strain accumulated band from grain boundary to grain interior. The left figure is early stage of the deformation while, the right one is final stage of the deformation. The mean true strain is 7.38% and 8.77%, respectively.

The localization process may take place in the following order. Firstly, the slip systems are activated inside of grains, and dislocations on these slip systems move. Secondly, dislocations move until they meet some obstacles, which are grain boundaries due to the lack of precipitation. Thirdly, dislocation pile-ups occur at the grain boundaries with the increase in the deformation. The possibility of slip transmission is not an issue since high-angle grain boundaries are majority. A slip passing into another grain becomes more difficult as the crystallographic misorientation increases. For high-angle grain boundaries, dislocations may tend to pile up at grain boundaries [101]. Therefore, passing into another grain is difficult, and this possibility is not likely to occur. After that, dislocation density increases in the vicinity of grain boundaries, and strain localizes to grain boundaries that form the strain localization band. Then, the

width of the localization band increases. Finally, both grain boundaries and small-sized grain localization are observed if the sample is deformed sufficiently. Thus, small grains accumulate larger strain in the microstructure having randomly distributed grain size. This observation is the exact opposite of the Hall-Petch approach. In the Hall-Petch equation, the grain size is rather considered as uniform, and samples having smaller grains are harder to deform. However, nonuniform grain size distribution in a polycrystal may have an inverse effect. This phenomenon of strain localization may take place in a shorter period for those small-size grains (roughly below average grain size).

Table 5.1. *Comparison of the increase in true strain values obtained from corresponding regions*

Region	*The Left Image*	*The Right Image*	*The Difference in Strain Values*
A	9.32%	11.41%	2.09%
B	6.96%	8.84%	1.88%
C	7.42%	9.48%	2.06%
D	7.92%	9.95%	2.03%
E	8.72%	11.02%	2.30%
F	7.45%	9.25%	1.80%
G	6.85%	9.10%	2.25%

The red arrows in Fig. 5.4. shows some grains where the strain band expands from the grain boundary to the grain interior. In the left image, the grain boundary localization and further localization through the grain interior can be seen in these regions. In the right image, one can observe that the strain localizes to the grain interior after the increase in the deformation. The size of grains located in the regions indicated as A, B, C, D, E, F, and G are various from 30 to 43 microns. The mean true strain of these results are 7.38% and 8.77%. The accumulated true strain values for these results in the regions located inside of the grain (showed by the end of the arrows) are indicated

in Table 5.1. The strain accumulated inside these grains increases more than the increase in average strain (1.39%). Thus, one can say that strain localization at the grain boundary can expand to grain inside with an increase in deformation.
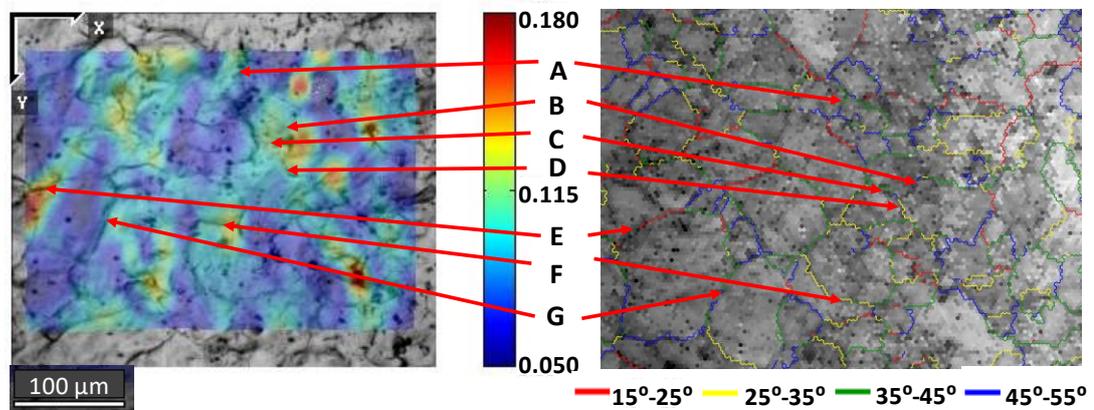
Figure 5.5. DIC result (left) and corresponding grain boundary angles (right) of the test named as Uni-4.

The material is a typical as-received polycrystalline Aluminum alloy, in which the inter-grain misorientation effects should be minimum since grain boundaries of high-angle are majority. As expected, the misorientation angle or grain boundary angle does not affect the strain localization behavior. Figure 5.5. shows the DIC results, and grain boundary angles of the test named as Uni-4. Table 5.2. shows some strain values localized at grain boundaries and corresponding grain boundary angle values. There is no correlation between the strain localization and the grain boundary angle. Region E and C accumulate almost the same strain, but there is a significant difference between the corresponding grain boundary angles, which are 16.1° and 56.6°, respectively. In addition, the minimum (Region G) and maximum (Region B) true strain values are observed at the grain boundaries having close grain boundary angles, which are 33.8° and 30.1°, respectively. Thus, the parameter of grain boundary angle is not considered to predict strain distribution.

Table 5.2. Comparison of grain boundary angles with true strain accumulated at corresponding grain boundaries

Region	Grain Boundary Angle	True Strain
A	44.3º	10.78%
B	30.1º	14.15%
C	56.6º	13.43%
D	39.3º	11.05%
E	16.1º	13.20%
F	30.8º	12.58%
G	33.8º	9.30%

Before examining the relation between strain localization and grain orientation, the change in grain orientation during deformation should be considered. The deformation behavior of the grains may change during the deformation since their orientation may change due to the rotation of grains [106]. Some studies investigate the effect of orientation change on deformation behavior [100], [107], [108]. These studies deform the samples at different deformation levels, so this effect varies from study to study. Each orientation is exposed to different orientation gradient [107]. To illustrate, the Goss orientation {011}⟨001⟩ does not rotate while the S orientation {123}⟨634⟩ causes orientation gradient during deformation. There is an obvious correlation between orientation change and deformation, but grain orientation changes are limited during deformation. The average orientation change is stated as 0.5° per 1% deformation strain in polycrystalline aluminum [109]. The average value of grain orientation change is 4° at 7.4% global tensile strain for FCC copper in the study of [100]. In another study, the average rotation of the tensile direction of the grains in FCC aluminum alloy is 2° at 6% tensile strain, which is less than the above studies [110]. It can be assumed that the grain orientation change is limited since the deformation is not large in this chapter. Therefore, it may not affect the family of orientation and direction. In addition, it is believed that the final grain orientation is responsible for

final strain localization behavior. In other words, grain orientation and strain localization should be compared with each other at the same time interval. In this chapter, final grain orientations are considered to investigate the relation between them and strain localization.

Strain tends to localize grain boundaries, but essentially the grains neighboring these boundaries take a role in the localization behavior. Orientations of these grains are rather specific family orientations such as $\langle 100 \rangle$ and $\langle 101 \rangle$. This result is expected since the Schmid factors of these orientations are large, and there are some studies, in which the relationship between strain localization and grain orientation is established. The Cube $\{001\}\langle 100 \rangle$ and Goss orientations accumulate large plastic strain [111]. In addition, an experimental study shows that grains close to $\langle 101 \rangle$ direction accumulate large local strains while the grains close to $\langle 112 \rangle$ usually accumulate low strains [97]. Figure 5.6. shows the IPF results with respect to the loading direction, and one can say that grains with red and green colors can be seen more in the localization region. These red and green colors match the $\langle 100 \rangle$ and $\langle 101 \rangle$ orientations, respectively. In addition, grains with $\langle 012 \rangle$ and $\langle 013 \rangle$ orientations can be seen in the localization region. However, the grains of these orientations can also accumulate low strain considering their grain size. Thus, any comment on strain localization with regards to grain orientations is not enough to explain the heterogeneity in strain distribution. The parameter of grain size should be considered as well.
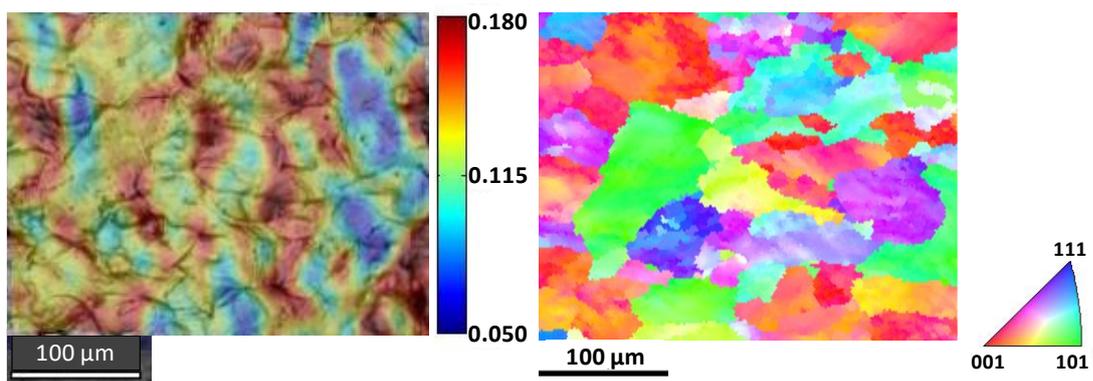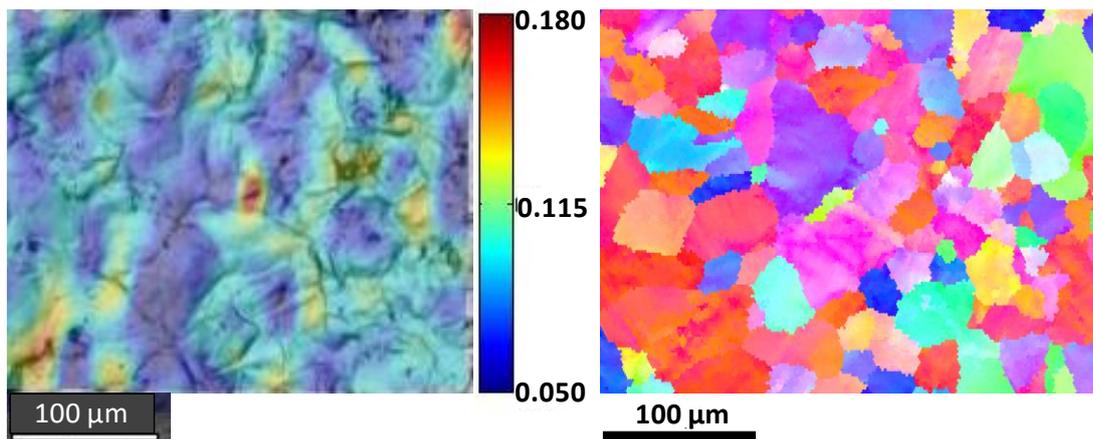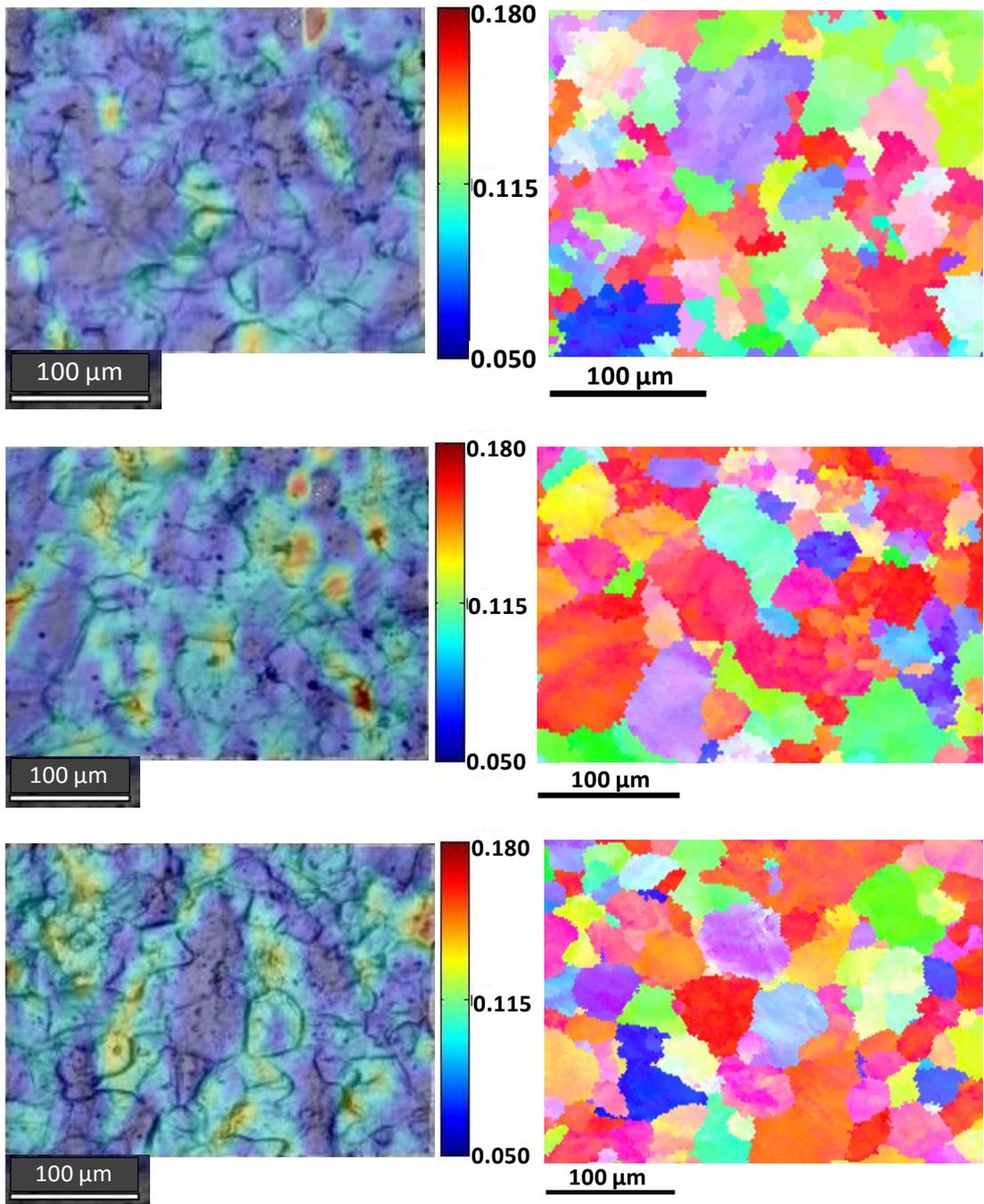
Figure 5.6. DIC results (left) and EBSD results of Uni-1, Uni-2, Uni-3, Uni-4, Uni-5 shown as from top to bottom, respectively. The EBSD results show the crystallographic orientation of the grains with respect to loading axis.

Strain localization tends to $\langle 001 \rangle$ direction according to the Sachs and the Taylor model since the Schmid factor is large, and the Taylor factor is low for this direction. Strain localization does not tend to $\langle 111 \rangle$ direction according to both models. However, there is a conflict for $\langle 101 \rangle$ direction. The origin of this discrepancy is that their approaches are different from each other. The Sachs model assumes that the stress distribution is the same along all grains, and its value equals to global stress. The strain distribution varies from grain to grain [87]. The Taylor model assumes that strain distribution is the same along all grains, and its value equals to global strain. The stress distribution varies from grain to grain [89]. The Sachs model is identified as suitable for the prediction of deformation behavior of single crystals, while the Taylor model is identified as suitable for polycrystalline metals [88]. On the other hand, both approaches are simplified models by considering assumptions of strain or stress homogeneity in a polycrystal, so they are not completely suitable for considering the mechanical interactions among crystals in a polycrystal [96]. This thesis concentrates on only heterogeneity of strain distribution in the microstructure. Each grain is investigated one by one to comment on strain localization behavior. Therefore, in this chapter, the Taylor model is not considered since there is not any investigation about stress distribution. In addition, both test regions and related microstructures are relatively small than the size which is needed for the success of the Taylor model in the prediction of deformation heterogeneity. The Taylor model can also be used for prediction of yield strength of polycrystals. The yield strength of material approximately equals to yield strength of an individual grain multiplied by average Taylor factor of all grains, which equals to 3. Therefore, this model is rather good at considering large-scale samples. Instead, the Sachs model is considered in this chapter since only the heterogeneity in strain distribution is considered, and a small part of the test region is examined. In this chapter, each grain is investigated one by one, so the suitability of this model on single crystals can be extended to polycrystals. Thus, the Schmid factor is primarily considered to predict the strain heterogeneity.

The grain level inhomogeneity is related to the effects of grain size and crystal orientations [16]. Crystal orientation with regards to loading direction determines the slip systems to be activated. Activation of these slip systems affects the strain localization behavior. The global loading increases the number of activated slip systems and dislocation density in a grain, so accumulated strain in related grain increases [112]. Thus, the number of activated slip systems with their Schmid factors and grain size are assumed as the main parameters that affect the strain localization. They are used to predict localization behavior in a typical FCC polycrystal in this chapter.

In the Sachs model, one activated slip system is responsible for deformation, but this assumption is made for a single crystal. According to von Mises, 5 independent slip systems are needed to deform a grain [113]. The Taylor model consists of the same condition where 5 of the 12 slip systems are required to produce plastic strain in FCC crystals. Apart from these classical approaches, there are some studies about the number of activated slip systems needed for deformation [98], [99], [114]. For polycrystals, two or more activated slip systems are required to generate deformation [114]. It is also observed that a few slip systems are activated simultaneously in each grain [98]. The study of [99] investigates that only two slip systems become apparent up to the deformation, which is 31.2% engineering strain. The primary and the secondary slip systems become apparent at 0.3% and 2% strain, respectively. Another study observes that almost all of the activated slip systems are slip systems with the largest Schmid factors [108]. In this chapter, it is considered that two slip systems with the largest value of the Schmid factor are activated during deformation. However, their activations take place at different deformation. The slip system having the largest Schmid factor is activated at early stage of deformation compared to the slip system having the second largest Schmid factor. The former contributes to more strain accumulation. To measure the effect of each slip system, the average value of the Schmid factor in an FCC polycrystal consisting of entirely random distribution of grain orientation is assumed as a reference point. This value is calculated as 0.446

[115]. It is believed that the slip systems having larger Schmid factors may assist to larger strain localization than average strain.

In this chapter, it is observed that the parameters of grain size and Schmid factor have a relation with strain localization. Table 5.3. shows this relation between strain localization and these two parameters individually, and the data is obtained from some of the grains in the result of Uni-2. In this table, grains, numbered from 1 to 4, have nearly equal grain size, and increase in Schmid factor values increases accumulated strain. The same relation exists between the grain-5 and grain-6. On the other hand, grain-5 has slip systems with slightly larger Schmid factors than grain-4 does. However, grain-4 accumulates larger strain than grain-5 since the former is nearly half of the latter in size. In addition, grain-2 and grain-3 have equal grain size and nearly equal the slip system with maximum Schmid factor. However, grain-3 accumulates more strain than grain-2 does thanks to the slip system with second maximum Schmid factor.

Table 5.3. *Relations between accumulated true strain with both Schmid factor and grain size*

Grain Number	Schmid Factor (max)	Schmid Factor (2nd max)	Grain size (μm)	Accumulated True Strain
1	0.439	0.417	40	0.168
2	0.479	0.389	39	0.170
3	0.470	0.450	40	0.180
4	0.485	0.460	35	0.185
5	0.490	0.490	62	0.162
6	0.463	0.424	60	0.145

Therefore, SLI method is contributed to predict the location of the accumulated large or small strain by using these parameters. The SLI method consists of the Equation 5.1., which is formed empirically by using the strain distribution results of 102 grains.

The reference values, which are the average values, are considered for both parameters. The deviation from the reference values is added to the Equation 5.1. The effect of this deviation for grain size is considered as inverse of the Hall-Petch approach. The parameter of grain size effect is the square root of the average grain size (58 microns), which is divided by the square root of the grain size of the investigated grain. The second parameter used in the Equation 5.1. is considered as two sub-parameters, which are the maximum and the second maximum Schmid factors. Both Schmid factors are divided individually by the average Schmid factor in FCC polycrystal, which is 0.446. Thus, there are three values calculated and added to equation which is:

$$N = \frac{\sqrt{\frac{d_{ave}}{d}} + \frac{m_{max}}{m_{ave}} + \frac{m_{2nd}}{m_{ave}}}{3} \qquad (5.1.)$$

where d is the size of the grain, d_{ave} is the average grain size, m_{max} is the maximum Schmid factor, m_{2nd} is the second maximum Schmid factor, m_{ave} is the average Schmid factor, and N is the parameter deciding whether the investigated grain may accumulate large or low strain. If N is larger than unity (with two decimal places), this grain tends to accumulate large strain, which is larger than the average strain. On the other hand, if N is lower than unity, this grain tends to accumulate low strain, which is lower than the average strain. The large or low strain localization region can be located either grain interiors or at the boundaries of grains. In both cases, these localization regions include grains and the parameters stated above are calculated according to these grains. To understand the working principle of the SLI method, if there is a large strain localization region at a grain boundary neighboring two grains; one can calculate the N parameter for one of these grains or both grains. Both calculations can provide the required information. Figure 5.7. shows the working principle of the N parameter. The N parameter of the grain named as grain-A is lower than the unity, so this grain accumulates low strain. On the other hand, both grain-B and grain-C accumulate large strain since the N parameters of these grains is larger

than the unity. Therefore, strain is localized to grain boundaries neighboring these grains. In addition, the grain size of grain-C is lower than the average grain size, which result in grain interior localization. However, the grain size of grain-B is larger than the average grain size, so, strain is not localized to the whole grain interior.
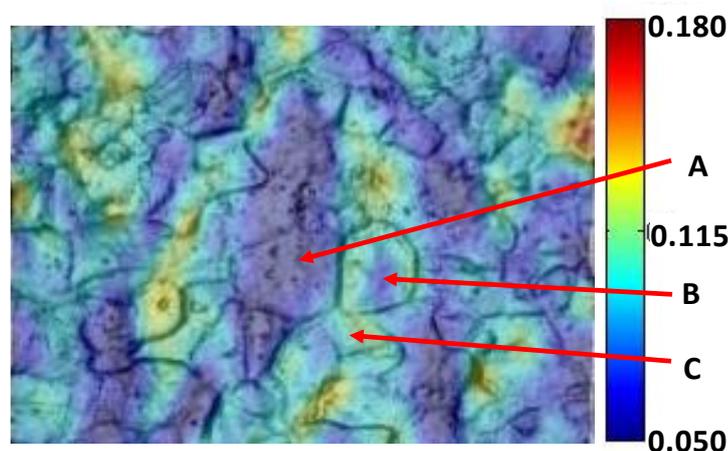
Figure 5.7. The working principle of the N parameter.

After determining the large and low strain accumulated regions, the accumulated strain values of corresponding regions are predicted. This is the second method, SLM, is contributed to predict the values of accumulated strain. The SLM method consists of the Equation 5.2., which is formed empirically by using the strain distribution results of 102 grains. The accumulated large strain values (above the average strain) are predicted successfully, while there are some deviations in the prediction of the accumulated low strain values (below the average strain). Therefore, the large strain values, which result in strain heterogeneity, are conducted. To predict the large strain values, two maximum Schmid factors, and the grain size are considered once again. Each grain is considered as an entire region, and the predicted strain values can be observed or measured inside of anywhere in corresponding grain during deformation. Before the deformation, one can predict the grain accumulating large strain by using

the SLI method and the value of it by using the SLM method. The exact location of this large strain spot cannot be predicted. However, the approximate location of these spots can be provided. In general, strain localization at grain boundaries is very common. When two neighboring grains are predicted as large strain spots, one can conclude that the grain boundary, which neighbors of these grains, accumulates the large strain. In addition, if a grain is small-sized, large strain is expected to localize to the grain interior. This approximation can be reasonable since only two parameters are considered in the SLI method. The SLI method provides to predict whether a grain is responsible for a large strain spot or not, by simple calculations. Therefore, in the case of predicting the amount of strain heterogeneity or rough location of large strain, both methods can be used. Thus, one can predict the strain heterogeneity in a microstructure and the values of accumulated large strain successfully. The only required parameters are the Schmid factor obtained by EBSD analysis and grain size measured by an optical image easily. The equation used in the SLM method for the prediction of values of accumulated large strain indicated as follows:

$$\varepsilon = \varepsilon_G \left((1 + (m_{max} - m_{ave}))(1 + (m_{2nd} - m_{ave})) \sqrt{\sqrt{\frac{d_{ave}}{d}}} \right) \quad (5.2.)$$

where ε is the predicted strain, ε_G is the global strain, m_{max} is the maximum Schmid factor, m_{2nd} is the second maximum Schmid factor, m_{ave} is the average Schmid factor, d is the size of the corresponding grain, d_{ave} is the average grain size. The parameter of grain size is calculated as square root of that used in the parameter N in the Equation 5.2. Both maximum and second maximum Schmid factors are considered in the Equation 5.2. The average values of the Schmid factor and grain size are used as reference values to determine the expected true strain. Global strain is used as the reference strain parameter in the Equation 5.2. The mean strain calculated by DIC is not used since it corresponds to the mean strain of a particular area, while the global strain corresponds to the mean strain of the whole test region. The global strain is

calculated as true strain to compare with DIC results of experiments in which strain distribution is calculated as true strain.
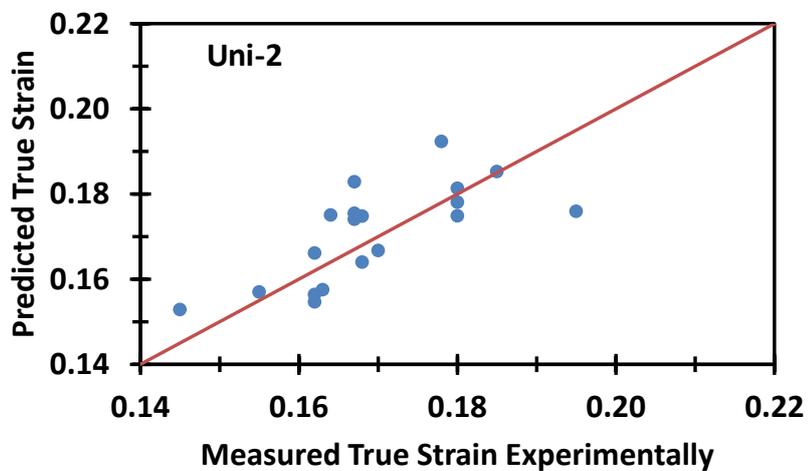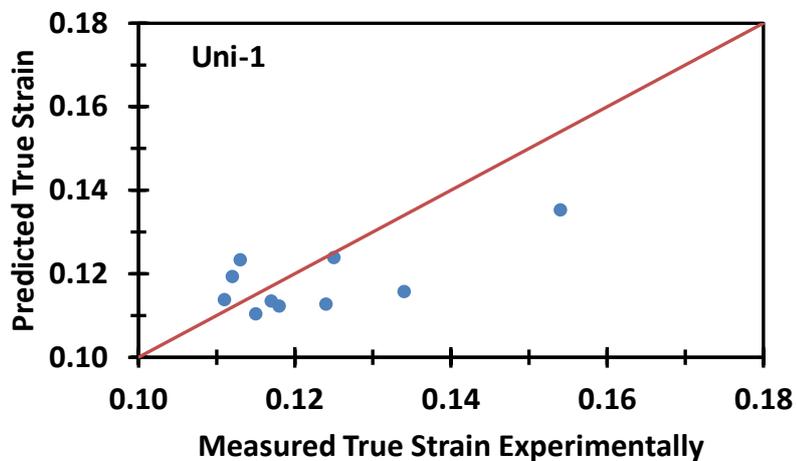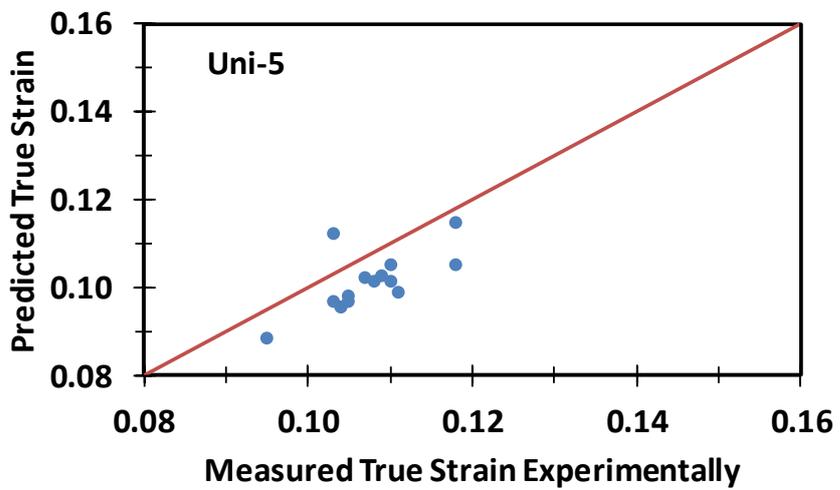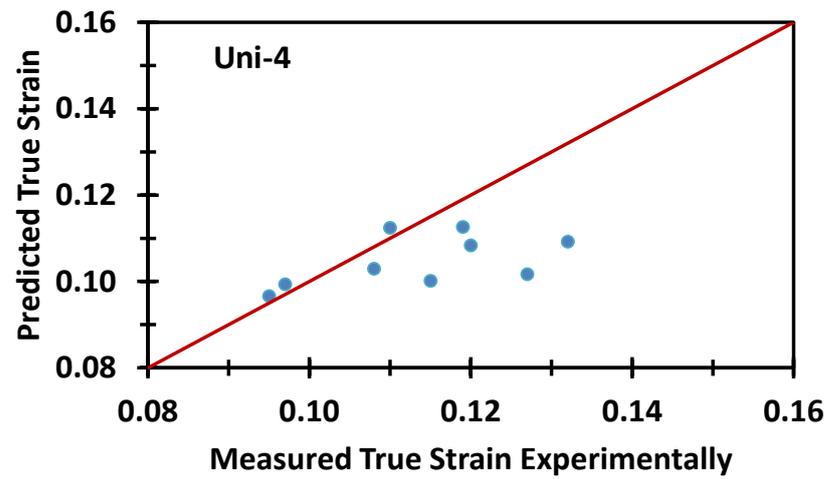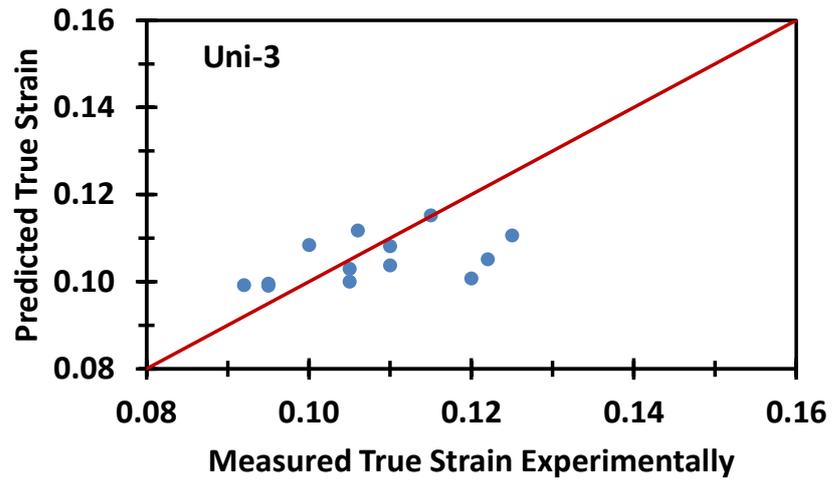
Figure 5.8. Measured and predicted true strain values of each test. The red line has a slope of unity.

Figure 5.8. shows the predicted true strain values and the actual ones of each test. The red line has a slope of unity. The predicted and the actual strain values are close to each other. Table 5.4. indicates the deviation between these predicted and actual true strain values. In addition, the success of the parameter of N, used in the SLI method, is indicated in Table 5.4. The parameter of N predicts the large or small strain regions with the success of over 90.5%. The mean of success is nearly 94%. The mean deviation between the predicted and actual large strain is varied from 4.1% to 8.4% using the SLM method. Therefore, considering all 102 grains in total, the predicted strain is about 6.5% different from the actual strain.

Table 5.4. *The deviation between predicted strain using the SLM method and strain measured experimentally and the success of the N parameter*

	Number of grains providing data	The success of N parameter	Max. deviation between predicted and actual strain (for above mean strain)	Mean of deviation between predicted and actual strain (for above mean strain)
Uni-1	19	97.4%	13.6%	6.5%
Uni-2	27	92.6%	9.8%	4.1%
Uni-3	20	95.0%	16.0%	6.6%
Uni-4	15	93.3%	19.8%	8.4%
Uni-5	21	90.5%	10.8%	6.8%

5.4. Conclusion

In this chapter, the reasons for strain heterogeneities were investigated in a polycrystalline, which was randomly textured FCC Aluminum alloy by considering grain orientation, grain size, and grain boundary angle. The samples had grains with randomly distributed orientation and size, so these parameters could be examined in a realistic microstructure. The grain boundary angle did not have any effects on strain heterogeneity since grain boundaries of high-angle were majority. The grain

orientation and the grain size were the dominant parameters causing strain heterogeneities. The result showed that the Schmid factor had an essential influence on strain localization. Grains with slip systems having larger Schmid factor with respect to the loading direction accumulated larger strain. In addition, grains with a smaller size accumulated large strain. The localization band expanded from grain boundary to grain interior with an increase in deformation. For small-size grains, large strain localization was observed since this mechanism occurred earlier. Therefore, for those small-size grains, larger strain localization at grain boundary or grain interior could be observed earlier, and it tended to accumulate larger strain with an increase in deformation. Thus, only with the parameters of Schmid factor and grain size, it was determined whether a grain accumulated large or low strain by using the SLI method contributed in this chapter. In addition, the SLM method was developed to calculate the magnitude of large strain (larger than mean strain). These parameters were simply obtained by using basic characterization techniques, which were EBSD providing Euler angles for calculating the Schmid factor and optical image providing grain size. As a result, in a randomly textured FCC polycrystalline material, it could be experimentally obtained whether each grain accumulated large or small strain by using the SLI method. Moreoever, the magnitude of strain accumulated at high spots could be calculated by using the SLM method.

CHAPTER 6

SUMMARY AND FUTURE WORKS

This thesis explained microstructural origins of strain localizations and instabilities that control the formability of the aluminum alloys. This was achieved through suppression of local necks and other geometric instabilities that typically limit the formability of the sheet metals. The true forming limits and the direct effect of microstructural features on the formability were identified with suppression of the local necks.

In order to measure the forming limits and analyze the formability of the samples in-situ, a portable biaxial test apparatus was demonstrated in this thesis. It was capable of testing miniature cruciform samples under biaxial stress states. In-situ strain analysis at the microstructure scale was possible with the custom-made microscope and 2D-DIC system integrated to the apparatus. A successful cruciform sample design was achieved with the help of FEA. Test results showed that the nonlinear FEA simulations of maximum effective stresses were quite successful in predicting the fracture locations of the samples. The small strain and premature fracture problems common to the cruciform tests were solved by optimizing the pit geometry and carefully controlling the manufacturing steps and surface finish. The flat and smooth test region resulted in center fracture and allowed in-plane deformation and 2D-DIC. Strain maps showed two strain bands intersecting at the center. The strain bands started to form at the corners when strain reached the strain hardening exponent, and allowed the center to be deformed under equibiaxial tension without significant shear strains. As the strain bands suppressed the formation of the local necks, the effective strain at the center reached to the fracture strain of the material.

The cruciform biaxial tension test was then shown as an alternative to the Nakajima test in determining the forming and fracture strains of the materials deforming without a local neck. In the absence of local necking, an alternative method, TRM, was

developed to determine the intensity of the localizations. The ratio of thickness strains in the regions having the maximum and minimum equivalent strains reached to a critical value and limited the formability of materials due to severe thinning in the localization regions. The TRM was applicable to both cruciform and Nakajima tests. In addition, the suppression of local necking benefited the measurement of fracture strains. The linear strain ratios in the cruciform test resulted in constant thickness strains independent of the strain paths. Thus, the cruciform test could be useful for investigations of the material behavior under certain strains paths and large strains. It was possible to reach the actual fracture limits in the cruciform test without deviating from the target strain ratio.

In order to verify that the test material developed the localizations due to the inconsistencies in the microstructure as opposed to the geometrical imperfections, multi-scale strain distribution was investigated in the same region of the sample and with the same amount of deformation. The region of interest was divided into two sub-regions accumulating minimum and maximum amount of strain, thereby a localization. Strain distribution at each sub-region was identical for both micro- and meso-scales. Besides, the size of investigated sub-regions was sufficient to show the micro-scale strain distribution at the meso-scale. Thus, the grain-scale parameters causing the non-homogeneous strain distribution took a role in meso-scale strain distribution and should be considered in studies conducted at the meso-scale.

After establishing the relationship between micro- and meso-scale localizations, the microstructural features, which take role in strain distribution, were investigated. The reasons for strain heterogeneities were investigated in Al 6061-T6, which was a randomly textured FCC polycrystal, by considering grain orientation, grain size, and grain boundary angle as the main microstructural features. The grain boundary angle did not have a significant effect on the strain heterogeneity since the grain boundaries of high-angle are the majority. The grain orientation and the grain size were the dominant parameters causing strain heterogeneities. Grains with slip systems having larger Schmid factor with respect to the loading direction accumulated larger strain.

In addition, grains with a smaller size accumulated large strain. For those small-size grains, larger strain localization at the grain boundary or grain interior could be observed earlier, and it tended to accumulate larger strain with an increase in deformation. Thus, only with the parameters of Schmid factor and grain size, it was determined whether a grain accumulated large or low strain by using the SLI method. In addition, the magnitude of large strain (larger than mean strain) was calculated with the SLM. These parameters were simply obtained by using basic characterization techniques, which were EBSD orientation maps providing Euler angles for calculation of the Schmid factor and optical images providing the grain size. As a result, in a randomly textured FCC polycrystalline metal, the SLI method was developed to identify whether each grain accumulated large or small strain. Moreover, the SLM method was contributed to calculate the magnitude of strain accumulated at high spots in this thesis.

In conclusion, this thesis developed the relation between the microstructural features and the strain heterogeneity at multiple scales in forming of aluminum. In the absence of local necking, or any other geometric instability, microstructural features were dominant in the formability of Al 6061-T6 since the micro-scale strain heterogeneity was matched to the meso-scale strain heterogeneity. The effects of grain orientation and grain size on the strain homogeneity were established. With the SLI and SLM methods introduced in this thesis, it was possible to characterize the microstructure-induced strain heterogeneity both qualitatively and quantitatively though the usage of simple EBSD and optical microscopy tools.

There are some future works recommended beyond this thesis. For investigations of meso-scale strain heterogeneity, the TRM could be applied to more brittle metals than Aluminum 6061-T6 in order to verify whether this method is applicable to any alloy. For investigations of the micro-scale heterogeneity, the coefficients in the equations of the SLI and the SLM methods can be modified to increase the accuracy of the methods. These methods can be applied to other strain path conditions, especially equibiaxial tension and plane strain, to verify that they are applicable to other strain

paths. In order to do that, a definition for the relationship between Schmid factors and the given stress state is needed. Therefore, the Schmid factors can be obtained for any given strain path. Then, the SLI and SLM methods can be applied under equibiaxial tension to verify them that they are successful for other strain path conditions. If necessary, they can be modified for other strain paths.

REFERENCES

[1] L. Leotoing, D. Guines, I. Zidane, and E. Ragneau, "Cruciform shape benefits for experimental and numerical evaluation of sheet metal formability," *J. Mater. Process. Technol.*, vol. 213, no. 6, pp. 856–863, 2013.

[2] D. Banabic, *Sheet metal forming processes*. Berlin: Springer-Verlag, 2010.

[3] P. D. Wu, S. R. MacEwen, D. J. Lloyd, and K. W. Neale, "A mesoscopic approach for predicting sheet metal formability," *Model. Simul. Mater. Sci. Eng.*, vol. 12, no. 3, pp. 511–527, 2004.

[4] Z. Marciniak and K. Kuczynski, "Limit strains in the processes of stretch-forming sheet metal," *J. Mech. Sci.*, vol. 9, pp. 609–620, 1967.

[5] D. Vysochinskiy, T. Coudert, O. S. Hopperstad, O. G. Lademo, and A. Reyes, "Experimental detection of forming limit strains on samples with multiple local necks," *J. Mater. Process. Technol.*, vol. 227, pp. 216–226, 2016.

[6] *Properties and Selection: Nonferrous Alloys and Special-Purpose Materials, ASM Handbook Vol.2*. ASM International, 1990.

[7] L. F. Peng, Z. T. Xu, M. W. Fu, and X. M. Lai, "Forming limit of sheet metals in meso-scale plastic forming by using different failure criteria," *Int. J. Mech. Sci.*, vol. 120, no. November 2016, pp. 190–203, 2017.

[8] A. Hannon and P. Tiernan, "A review of planar biaxial tensile test systems for sheet metal," *J. Mater. Process. Technol.*, vol. 198, no. 1–3, pp. 1–13, 2008.

[9] X. Song, L. Leotoing, D. Guines, and E. Ragneau, "Investigation of the forming limit strains at fracture of AA5086 sheets using an in-plane biaxial tensile test," *Engineering Fracture Mechanics*, vol. 163. pp. 130–140, 2016.

[10] B. Güler and M. Efe, "Large Strain Cruciform Biaxial Testing for FLC Detection," in *AIP Conference Proceedings*, 2017, vol. 020018.

[11] B. Güler, K. Alkan, and M. Efe, "Formability analysis of sheet metals by cruciform testing," in *IOP Conf. Series: Journal of Physics: Conf. Series*, 2017.

[12] Y. Seymen, B. Güler, and M. Efe, "Large Strain and Small-Scale Biaxial Testing of Sheet Metals," *Exp. Mech.*, vol. 56, no. 9, pp. 1519–1530, 2016.

[13] B. Güler and M. Efe, "Forming and fracture limits of sheet metals deforming without a local neck," *J. Mater. Process. Technol.*, vol. 252, no. October 2017, pp. 477–484, 2018.

[14] A. W. Mello, A. Nicolas, R. A. Lebensohn, and M. D. Sangid, "Effect of

microstructure on strain localization in a 7050 aluminum alloy: Comparison of experiments and modeling for various textures," *Mater. Sci. Eng. A*, vol. 661, pp. 187–197, 2016.

[15] M. R. Stoudt, L. E. Levine, A. Creuziger, and J. B. Hubbard, "The fundamental relationships between grain orientation, deformation-induced surface roughness and strain localization in an aluminum alloy," *Mater. Sci. Eng. A*, vol. 530, no. 1, pp. 107–116, 2011.

[16] X. H. Hu, M. Jain, D. S. Wilkinson, and R. K. Mishra, "Microstructure-based finite element analysis of strain localization behavior in AA5754 aluminum sheet," *Acta Mater.*, vol. 56, no. 13, pp. 3187–3201, 2008.

[17] D. Li and A. K. Ghosh, "Biaxial warm forming behavior of aluminum sheet alloys," *J. Mater. Process. Technol.*, vol. 145, no. 3, pp. 281–293, 2004.

[18] W. Tong, "Strain characterization of propagative deformation bands," *J. Mech. Phys. Solids*, vol. 46, no. 10, pp. 2087–2102, 1998.

[19] C. C. Aydiner and M. A. Telemez, "Multiscale deformation heterogeneity in twinning magnesium investigated with in situ image correlation," *Int. J. Plast.*, vol. 56, pp. 203–218, 2014.

[20] C. Efstathiou, H. Sehitoglu, and J. Lambros, "Multiscale strain measurements of plastically deforming polycrystalline titanium: Role of deformation heterogeneities," *Int. J. Plast.*, vol. 26, no. 1, pp. 93–106, 2010.

[21] M. Kleiner, M. Geiger, and A. Klaus, "Manufacturing of lightweight components by metal forming," *CIRP Ann. - Manuf. Technol.*, vol. 52, no. 2, pp. 521–542, 2003.

[22] J. Blaber, B. Adair, and A. Antoniou, "Ncorr: Open-Source 2D Digital Image Correlation Matlab Software," *Exp. Mech.*, vol. 55, no. 6, pp. 1105–1122, 2015.

[23] B. Pan, K. Qian, H. Xie, and A. Asundi, "Two-dimensional digital image correlation for in-plane displacement and strain measurement : a review," vol. 062001.

[24] R. Sowerby, E. Chu, and J. L. Duncan, "Determination of large strains in metalforming," *J. Strain Anal. Eng. Des.*, vol. 17, no. 2, pp. 95–101, 1982.

[25] N. Deng, T. Kuwabara, and Y. P. Korkolis, "Cruciform Specimen Design and Verification for Constitutive Identification of Anisotropic Sheets," *Exp. Mech.*, vol. 55, no. 6, pp. 1005–1022, 2015.

[26] F. Abu-Farha, L. G. Hector, and M. Khraisheh, "Cruciform-shaped specimens for elevated temperature biaxial testing of lightweight materials," *Jom*, vol. 61, no. 8, pp. 48–56, 2009.

[27] R. A. Cláudio, I. Guelho, L. Reis, M. Freitas, B. Li, and J. F. A. Madeira,

"Optimization of cruciform specimen for a low capacity biaxial testing machines," in *10th International Conference of Multiaxial Fatigue Fracture*, 2013.

[28] A. Ghiotti, S. Bruschi, and P. Bariani, "Determination of yield locus of sheet metal at elevated temperatures: A novel concept for experimental set-up," *Key Eng. Mater.*, vol. 344, pp. 97–104, 2007.

[29] D. E. Green, K. W. Neale, S. R. MacEwen, A. Makinde, and R. Perrin, "Experimental investigation of the biaxial behaviour of an aluminum sheet," *Int. J. Plast.*, vol. 20, no. 8–9, pp. 1677–1706, 2004.

[30] I. Zidane, D. Guines, L. Léotoing, and E. Ragneau, "Development of an in-plane biaxial test for forming limit curve (FLC) characterization of metallic sheets," *Meas. Sci. Technol.*, vol. 21, no. 5, p. 055701, 2010.

[31] W. Liu, D. Guines, L. Leotoing, and E. Ragneau, "Identification of sheet metal hardening for large strains with an in-plane biaxial tensile test and a dedicated cross specimen," *Int. J. Mech. Sci.*, vol. 101–102, pp. 387–398, 2015.

[32] C. C. Tasan, J. P. M. Hoefnagels, G. Quaak, and M. G. D. Geers, "In-plane biaxial loading of sheet metal until fracture," *Soc. Exp. Mech. - 11th Int. Congr. Exhib. Exp. Appl. Mech. 2008*, vol. 4, pp. 1729–1736, 2008.

[33] J. S. Welsh and D. F. Adams, "An experimental investigation of the biaxial strength of IM6/3501-6 carbon/epoxy cross-ply laminates using cruciform specimens," *Compos. - Part A Appl. Sci. Manuf.*, vol. 33, no. 6, pp. 829–839, 2002.

[34] C. C. Tasan, M. J. P. Hoefnagels, E. C. A. Dekkers, and M. G. D. Geers, "Multi-Axial Deformation Setup for Microscopic Testing of Sheet Metal to Fracture," pp. 669–678, 2012.

[35] J. Hu, Z. Marciniak, and J. Duncan, *Mechanics of Sheet Metal Forming*. London, 1992.

[36] W. M. Johnston, D. S. Dawicke, and W. D. Pollock, "Biaxial Testing of 2219-T87 Aluminum Alloy Using Cruciform Specimens," no. NASA Contractor Report 4782, 1997.

[37] W. . Hosford and R. . Caddell, *Metal forming mechanics and metallurgy*, 3rd ed. Cambridge: Cambridge University Press, 2007.

[38] A. K. Ghosh, "Strain Localization in the Diffuse Neck in Sheet Metal.," *Met. Trans*, vol. 5, no. 7, pp. 1607–1616, 1974.

[39] K. S. Raghavan, "A simple technique to generate in-plane forming limit curves and selected applications," *Metall. Mater. Trans. A*, vol. 26, no. 8, pp. 2075–2084, 1995.

[40] W. Hotz, M. Merklein, A. Kuppert, H. Friebe, and M. Klein, "Time dependent FLC determination - Comparison of different algorithms to detect the onset of unstable necking before fracture," *Key Eng. Mater.*, vol. 549, pp. 397–404, 2013.

[41] W. Volk and P. Hora, "New algorithm for a robust user-independent evaluation of beginning instability for the experimental FLC determination," *Int. J. Mater. Form.*, vol. 4, no. 3, pp. 339–346, 2011.

[42] J. D. Embury and J. L. Duncan, "Formability Maps," *Annu. Rev. Mater. Sci.*, vol. 11, no. 1, pp. 505–521, 1981.

[43] A. S. Korhonen and T. Manninen, "Forming and fracture limits of austenitic stainless steel sheets," *Mater. Sci. Eng. A*, vol. 488, no. 1–2, pp. 157–166, 2008.

[44] S. Bruschi *et al.*, "Testing and modelling of material behaviour and formability in sheet metal forming," *CIRP Ann. - Manuf. Technol.*, vol. 63, no. 2, pp. 727–749, 2014.

[45] J. Jeswiet, F. Micari, G. Hirt, A. Bramley, J. Duflou, and J. Allwood, "Asymmetric single point incremental forming of sheet metal," *CIRP Ann. - Manuf. Technol.*, vol. 54, no. 2, pp. 88–114, 2005.

[46] W. C. Emmens and A. H. van den Boogaard, "An overview of stabilizing deformation mechanisms in incremental sheet forming," *J. Mater. Process. Technol.*, vol. 209, no. 8, pp. 3688–3695, 2009.

[47] P. A. F. Martins, N. Bay, M. Skjoedt, and M. B. Silva, "Theory of single point incremental forming," *CIRP Ann. - Manuf. Technol.*, vol. 57, no. 1, pp. 247–252, 2008.

[48] C. Karadogan and M. E. Tamer, "Development of a new and simplified procedure for the experimental determination of forming limit curves," *CIRP Annals - Manufacturing Technology*, vol. 64, no. 1. pp. 265–268, 2015.

[49] H. Aretz, "Numerical analysis of diffuse and localized necking in orthotropic sheet metals," *Int. J. Plast.*, vol. 23, no. 5, pp. 798–840, 2007.

[50] D. Banabic, S. Comsa, P. Jurco, G. Cosovici, L. Paraianu, and D. Julean, "FLD theoretical model using a new anisotropic yield criterion," *J. Mater. Process. Technol.*, vol. 157–158, no. SPEC. ISS., pp. 23–27, 2004.

[51] P. A. F. Martins, N. Bay, A. E. Tekkaya, and A. G. Atkins, "Characterization of fracture loci in metal forming," *Int. J. Mech. Sci.*, vol. 83, pp. 112–123, 2014.

[52] A. G. Atkins, "Fracture in forming," *J. Mater. Process. Technol.*, vol. 56, no. 1–4, pp. 609–618, 1996.

[53] Y. Bao and T. Wierzbicki, "On fracture locus in the equivalent strain and stress triaxiality space," *Int. J. Mech. Sci.*, vol. 46, no. 1, pp. 81–98, 2004.

[54] D. Raabe, M. Sachtleber, Z. Zhao, F. Roters, and S. Zaefferer, "Micromechanical and macromechanical effects in grain scale polycrystal plasticity experimentation and simulation," *Acta Mater.*, vol. 49, no. 17, pp. 3433–3441, 2001.

[55] F. Delaire, J. L. Raphanel, and C. Rey, "Plastic heterogeneities of a copper multicrystal deformed in uniaxial tension: Experimental study and finite element simulations," *Acta Mater.*, vol. 48, no. 5, pp. 1075–1087, 2000.

[56] E. Héripré *et al.*, "Coupling between experimental measurements and polycrystal finite element calculations for micromechanical study of metallic materials," *Int. J. Plast.*, vol. 23, no. 9, pp. 1512–1539, 2007.

[57] P. Van Houtte, A. K. Kanjarla, A. Van Bael, M. Seefeldt, and L. Delannay, "Multiscale modelling of the plastic anisotropy and deformation texture of polycrystalline materials," *Eur. J. Mech. A/Solids*, vol. 25, no. 4, pp. 634–648, 2006.

[58] E. W. . Coenen, V. . Kouznetsova, and M. G. . Geers, "Multi-scale continuous-discontinuous framework for computational-homogenization-localization," *J. Mech. Phys. Solids*, vol. 60, pp. 1486–1507, 2012.

[59] S. A. Asgari, P. D. Hodgson, C. Yang, and B. F. Rolfe, "Modeling of Advanced High Strength Steels with the realistic microstructure-strength relationships," *Computational Materials Science*, vol. 45, no. 4. pp. 860–866, 2009.

[60] S. Nemat-Nasser and M. Hori, *Micromechanics: overall properties of heterogeneous materials*. Amsterdam: North-Holland Series in Applied Mathematics and Mechanics, Elsevier Science Publishers BV, 1993.

[61] B. Berisha, C. Raemy, C. Becker, M. Gorji, and P. Hora, "Multiscale modeling of failure initiation in a ferritic-pearlitic steel," *Acta Materialia*, vol. 100. pp. 191–201, 2015.

[62] X. Hu, D. S. Wilkinson, M. Jain, P. Wu, and R. K. Mishra, "Fuel cap stamping simulation of AA5754 sheets using a microstructure based macro-micro multi-scale approach," *Computational Materials Science*, vol. 98. pp. 354–365, 2015.

[63] S. Ravindran, B. Koohbor, and A. Kidane, "Experimental characterization of meso-scale deformation mechanisms and the RVE size in plastically deformed carbon steel," *Strain*, vol. 53, no. 1, pp. 12–20, 2017.

[64] Z. Zhao, M. Ramesh, D. Raabe, A. M. Cuitiño, and R. Radovitzky, "Investigation of three-dimensional aspects of grain-scale plastic surface deformation of an aluminum oligocrystal," *Int. J. Plast.*, vol. 24, no. 12, pp. 2278–2297, 2008.

[65] P. S. Bate and W. B. Hutchinson, "Grain boundary area and deformation," *Scr. Mater.*, vol. 52, no. 3, pp. 199–203, 2005.

[66] W. A. Counts, M. V Braginsky, C. C. Battaile, and E. A. Holm, "Predicting the Hall – Petch effect in fcc metals using non-local crystal plasticity," vol. 24, pp. 1243–1263, 2008.

[67] E. O. Hall, "The Deformation and Ageing of Mild Steel: III Discussion of Results," *Proc. Phys. Soc. Sect. B*, vol. 64, no. 9, pp. 747–753, Sep. 1951.

[68] N.J. Petch, "The Cleavage Strengh of Polycrystals," *J. Iron Steel Inst.*, vol. 174, pp. 25–28, 1953.

[69] T. Narutani and J. Takamura, "Grain-size strengthening in terms of dislocation density measured by resistivity," *Acta Metall. Mater.*, 1991.

[70] A. Acharya and A. J. Beaudoin, "Grain-size effect in viscoplastic polycrystals at moderate strains," *J. Mech. Phys. Solids*, vol. 48, no. 10, pp. 2213–2230, 2000.

[71] J. Kim and J. Whan, "Necking behavior of AA 6022-T4 based on the crystal plasticity and damage models," *Int. J. Plast.*, vol. 73, pp. 3–23, 2015.

[72] E. . Lehockey, G. Palumbo, K. . Aust, U. Erb, and P. Lin, "On the role of intercrystalline defects in polycrystal plasticity," *Scr. Mater.*, vol. 39, no. 3, pp. 341–346, 1998.

[73] S. Zaefferer, J. Kuo, Z. Zhao, M. Winning, and D. Raabe, "On the influence of the grain boundary misorientation on the plastic deformation of aluminum bicrystals," vol. 51, pp. 4719–4735, 2003.

[74] A. Ma, F. Roters, and D. Raabe, "On the consideration of interactions between dislocations and grain boundaries in crystal plasticity finite element modeling – Theory , experiments , and simulations," vol. 54, pp. 2181–2194, 2006.

[75] A. P. Zhilyaev, G. V. Nurislamova, B. K. Kim, M. D. Baró, J. A. Szpunar, and T. G. Langdon, "Experimental parameters influencing grain refinement and microstructural evolution during high-pressure torsion," *Acta Mater.*, vol. 51, no. 3, pp. 753–765, 2003.

[76] S. J. Vachhani, R. D. Doherty, and S. R. Kalidindi, "Studies of grain boundary regions in deformed polycrystalline aluminum using spherical nanoindentation," *Int. J. Plast.*, vol. 81, pp. 87–101, 2016.

[77] A. Krishna, P. Van Houtte, and L. Delannay, "Assessment of plastic heterogeneity in grain interaction models using crystal plasticity finite element method," *Int. J. Plast.*, vol. 26, no. 8, pp. 1220–1233, 2010.

[78] W. Z. Abuzaid, H. Sehitoglu, and J. Lambros, "Localisation of plastic strain at the microstructurlal level in Hastelloy X subjected to monotonic , fatigue , and creep loading : the role of grain boundaries and slip transmission," *Mater. High Temp.*, vol. 3409, no. September 2017, pp. 1–17, 2016.

[79] W. Z. Abuzaid, M. D. Sangid, J. D. Carroll, H. Sehitoglu, and J. Lambros, "Slip transfer and plastic strain accumulation across grain boundaries in Hastelloy X," *J. Mech. Phys. Solids*, vol. 60, no. 6, pp. 1201–1220, 2012.

[80] K. Cheong and E. P. Busso, "Effects of lattice misorientations on strain heterogeneities in FCC polycrystals," vol. 54, pp. 671–689, 2006.

[81] D. Raabe, Z. Zhao, and W. Mao, "On the dependence of in-grain subdivision and deformation texture of aluminum on grain interaction," *Acta Mater.*, vol. 50, no. 17, pp. 4379–4394, 2002.

[82] S. R. Kalidindi, A. Bhattacharyya, and R. D. Doherty, "Detailed analyses of grain-scale plastic deformation in columnar polycrystalline aluminium using orientation image mapping and crystal plasticity models," *Proc. R. Soc. A Math. Phys. Eng. Sci.*, vol. 460, no. 2047, pp. 1935–1956, 2004.

[83] X. Huang and G. Winther, "Dislocation structures. Part I. Grain orientation dependence," *Philos. Mag.*, vol. 87, no. 33, pp. 5189–5214, 2007.

[84] M. Moore and P. Bate, "Microstructural inhomogeneity and biaxial stretching limits in aluminium alloy AA6016," *J. Mater. Process. Technol.*, vol. 125–126, pp. 258–266, 2002.

[85] P. Chen *et al.*, "In-situ EBSD study of the active slip systems and lattice rotation behavior of surface grains in aluminum alloy during tensile deformation," *Mater. Sci. Eng. A*, vol. 580, pp. 114–124, 2013.

[86] E. Schmid and W. Boas, "Kristallplastizität: mit besonderer Berücksichtigung der Metalle," *J. Springer*, vol. 17, 1935.

[87] G. Sachs, "Zietschrift Verein," *Deut. Ing.*, vol. 72, pp. 734–736, 1928.

[88] R. Pokharel *et al.*, "Polycrystal Plasticity: Comparison Between Grain - Scale Observations of Deformation and Simulations," *Annu. Rev. Condens. Matter Phys.*, vol. 5, no. 1, pp. 317–346, 2014.

[89] G. I. Taylor, "Plastic strain in metals," *J. Inst. Met.*, vol. 62, pp. 307–324, 1938.

[90] J. W. Hutchinson, "Elastic- plastic behavior of polycrystalline metals and composites," *Proc Roy Soc Ser A Math Phys Sci*, vol. 319, no. 1537, pp. 247–272, 1970.

[91] W. Mao, "Intergranular mechanical equilibrium during the rolling deformation of polycrystalline metals based on Taylor principles," *Mater. Sci. Eng. A*, vol. 672, pp. 129–134, 2016.

[92] R. A. Lebensohn, C. N. Tomé, and P. P. Castañeda, "Self-consistent modelling of the mechanical behaviour of viscoplastic polycrystals incorporating intragranular field fluctuations," *Philos. Mag.*, vol. 87, no. 28, pp. 4287–4322, 2007.

[93]   P. Van Houtte, S. Li, M. Seefeldt, and L. Delannay, *Deformation texture prediction: From the Taylor model to the advanced Lamel model*, vol. 21, no. 3. 2005.

[94]   S. K. Mishra, P. Pant, K. Narasimhan, A. D. Rollett, and I. Samajdar, "On the widths of orientation gradient zones adjacent to grain boundaries," *Scr. Mater.*, vol. 61, no. 3, pp. 273–276, 2009.

[95]   N. Zhang and W. Tong, "An experimental study on grain deformation and interactions in an Al-0. 5%Mg multicrystal," *Int. J. Plast.*, vol. 20, no. 3, pp. 523–542, 2004.

[96]   F. Roters, P. Eisenlohr, L. Hantcherli, D. D. Tjahjanto, T. R. Bieler, and D. Raabe, "Overview of constitutive laws , kinematics , homogenization and multiscale methods in crystal plasticity finite-element modeling : Theory , experiments , applications," *Acta Mater.*, vol. 58, no. 4, pp. 1152–1211, 2010.

[97]   G. Zhu, X. Hu, J. Kang, R. K. Mishra, and D. S. Wilkinson, "Deformation inhomogeneity in large-grained AA5754 sheets," *Mater. Sci. Eng. A*, vol. 528, no. 12, pp. 4187–4198, May 2011.

[98]   A. Guery, F. Hild, F. Latourte, and S. Roux, "Slip activities in polycrystals determined by coupling DIC measurements with crystal plasticity calculations," *Int. J. Plast.*, vol. 81, pp. 249–266, 2016.

[99]   S. Kahl, R. L. Peng, M. Calmunger, B. Olsson, and S. Johansson, "In situ EBSD during tensile test of aluminum AA3003 sheet," *Micron*, vol. 58, pp. 15–24, 2014.

[100] A. Tatschl and O. Kolednik, "On the experimental characterization of crystal plasticity in polycrystals," *Mater. Sci. Eng. A*, vol. 342, no. 1–2, pp. 152–168, 2003.

[101] W. D. Callister, *Materials Science and Engineering, An Introduction*, 7th ed. New York: John Wiley & Sons Inc., 2007.

[102] H. J. Bunge and C. Esling, *Quantitative texture analysis*. Oberursel: DGM-Informationsgesellschaft, 1982.

[103] F. J. Humphreys and M. Hatherly, *Recrystallization and related annealing phenomena*, First Edit. Oxford: Elsevier Science Ltd., 1995.

[104] G. E. Dieter, *Mechanical Metallurgy*, SI Metric. Singapore: McGraw-Hill, 1988.

[105] T. Gladman, "Precipitation hardening in metals," *Mater. Sci. Technol.*, vol. 15, no. 1, pp. 30–36, 1999.

[106] L. S. Tóth, Y. Estrin, R. Lapovok, and C. Gu, "A model of grain fragmentation based on lattice curvature," *Acta Mater.*, vol. 58, no. 5, pp. 1782–1794, 2010.

[107] D. Raabe, Z. Zhao, S. J. Park, and F. Roters, "Theory of orientation gradients in plastically strained crystals," *Acta Mater.*, vol. 50, pp. 421–440, 2002.

[108] G. Winther, "Slip systems extracted from lattice rotations and dislocation structures," *Acta Mater.*, vol. 56, no. 9, pp. 1919–1932, 2008.

[109] L. Margulies, G. Winther, and H. F. Poulsen, "In situ measurement of grain rotation during deformation of polycrystals," *Science (80-.).*, vol. 291, no. 5512, pp. 2392–2394, 2001.

[110] H. F. Poulsen, L. Margulies, S. Schmidt, and G. Winther, "Lattice rotations of individual bulk grains. Part I: 3D X-ray characterization," *Acta Mater.*, vol. 51, no. 13, pp. 3821–3830, 2003.

[111] D. Raabe, M. Sachtleber, H. Weiland, G. Scheele, and Z. Zhao, "Grain-scale micromechanics of polycrystal surfaces during plastic straining," *Acta Mater.*, vol. 51, no. 6, pp. 1539–1560, 2003.

[112] A. Musienko, A. Tatschl, K. Schmidegg, O. Kolednik, R. Pippan, and G. Cailletaud, "Three-dimensional finite element simulation of a polycrystalline copper specimen," *Acta Mater.*, vol. 55, no. 12, pp. 4121–4136, 2007.

[113] R. Von Mises, "Mechanik der plastischen formänderung von kristallen," *Zeitschrift für Angew. Math. und Mech.*, vol. 8, pp. 161–185, 1928.

[114] T. R. Bieler *et al.*, "The role of heterogeneous deformation on damage nucleation at grain boundaries in single phase metals," *Int. J. Plast.*, vol. 25, no. 9, pp. 1655–1683, 2009.

[115] J. P. Chateau, *Mechanical Properties of Complex Intermetallics*. Singapore: World Scientific, 2010.

A. Determination of the orientation and the direction of grains by Bunge-Euler angles.

From the Bunge-Euler angle, the orientation matrix G is calculated as follows:

$G =$

$$\begin{matrix} \cos\varphi_1\cos\varphi_2 - \sin\varphi_1\sin\varphi_2\cos\phi & \sin\varphi_1\cos\varphi_2 + \cos\varphi_1\sin\varphi_2\cos\phi & \sin\phi\,\sin\varphi_2 \\ -\cos\varphi_1\sin\varphi_2 - \sin\varphi_1\cos\varphi_2\cos\phi & -\sin\varphi_1\sin\varphi_2 + \cos\varphi_1\cos\varphi_2\cos\phi & \sin\phi\,\sin\varphi_2 \\ \sin\varphi_1\sin\phi & -\cos\varphi_1\sin\phi & \cos\phi \end{matrix}$$

where the Bunge-Euler angle represented as (φ_1 ϕ φ_2) and the three columns of the orientation matrix indicate the Miller indices of the reference, transverse, and normal directions, respectively. The grain normal direction (specimen normal direction) with grain direction (with respect to loading direction) represented as {hkl}⟨uvw⟩, respectively.

B. Calculating the Schmid factor for each of 12 slip systems in a crystal.

The Schmid factor of slip systems is calculated as follows:

$$m = cos\phi\ \cos\lambda$$

where m is the Schmid factor, ϕ is the angle between normal to the slip plane and the applied loading direction, and λ is the angle between the slip and the loading directions.

The $\cos\phi$ and $\cos\lambda$ can be calculated as follows:

$$cos\phi \text{ or } \cos\lambda = \left(\frac{u_1u_2 + v_1v_2 + w_1w_2}{\sqrt{(u_1^2 + v_1^2 + w_1^2)(u_2^2 + v_2^2 + w_2^2)}} \right)$$

where ($u_1v_1w_1$) and ($u_2v_2w_2$) indices represent normal to the slip plane and the loading direction for calculating $\cos\phi$, and the slip and the loading directions for calculating $\cos\lambda$, respectively. Table A.1. shows the indices of slip systems used in this study.

Table A.1. *Notation of Slip Systems*

Slip system index	*Plane*	*Direction*
1	(-111)	[0-11]
2	(-111)	[101]
3	(-111)	[110]
4	(111)	[0-11]
5	(111)	[-101]
6	(111)	[1-10]
7	(11-1)	[011]
8	(11-1)	[101]
9	(11-1)	[1-10]
10	(1-11)	[011]
11	(1-11)	[-101]
12	(1-11)	[110]

C. Elsevier Permission License

D. Springer Permission License

SPRINGER NATURE LICENSE TERMS AND CONDITIONS

Jan 27, 2020

This Agreement between METU -- Baran Güler ("You") and Springer Nature ("Springer Nature") consists of your license details and the terms and conditions provided by Springer Nature and Copyright Clearance Center.

License Number	4757180417749
License date	Jan 27, 2020
Licensed Content Publisher	Springer Nature

Licensed Content Publication	Experimental Mechanics
Licensed Content Title	Large Strain and Small-Scale Biaxial Testing of Sheet Metals
Licensed Content Author	Y. Seymen, B. Güler, M. Efe
Licensed Content Date	Jan 1, 2016
Licensed Content Volume	56
Licensed Content Issue	9
Type of Use	Thesis/Dissertation
Requestor type	academic/university or research institute
Format	print and electronic
Portion	Text extract
Number of text extracts	2
Will you be translating?	no
Circulation/distribution	1 - 29
Author of this Springer Nature content	yes
Title	Microstructural Origins of Strain Heterogeneity in Formability of Aluminum Alloys
Institution name	Middle East Technical University
Expected presentation date	Jan 2020

Portions	Experimental Part
	METU
	METU, Department of Metallurgical and Materials Engineering
Requestor Location	
	Ankara, Ankara 06800 Turkey
	Attn: METU
Total	0.00 USD

Terms and Conditions

Springer Nature Customer Service Centre GmbH Terms and Conditions

This agreement sets out the terms and conditions of the licence (the **Licence**) between you and **Springer Nature Customer Service Centre GmbH** (the **Licensor**). By clicking 'accept' and completing the transaction for the material (**Licensed Material**), you also confirm your acceptance of these terms and conditions.

Grant of License

The Licensor grants you a personal, non-exclusive, non-transferable, world-wide licence to reproduce the Licensed Material for the purpose specified in your order only. Licences are granted for the specific use requested in the order and for no other use, subject to the conditions below.

The Licensor warrants that it has, to the best of its knowledge, the rights to license reuse of the Licensed Material. However, you should ensure that the material you are

requesting is original to the Licensor and does not carry the copyright of another entity (as credited in the published version).

If the credit line on any part of the material you have requested indicates that it was reprinted or adapted with permission from another source, then you should also seek permission from that source to reuse the material.

Scope of Licence

You may only use the Licensed Content in the manner and to the extent permitted by these Ts&Cs and any applicable laws.

A separate licence may be required for any additional use of the Licensed Material, e.g. where a licence has been purchased for print only use, separate permission must be obtained for electronic re-use. Similarly, a licence is only valid in the language selected and does not apply for editions in other languages unless additional translation rights have been granted separately in the licence. Any content owned by third parties are expressly excluded from the licence.

Similarly, rights for additional components such as custom editions and derivatives require additional permission and may be subject to an additional fee. Please apply to Journalpermissions@springernature.com/bookpermissions@springernature.com for these rights.

Where permission has been granted **free of charge** for material in print, permission may also be granted for any electronic version of that work, provided that the material is incidental to your work as a whole and that the electronic version is essentially equivalent to, or substitutes for, the print version.

An alternative scope of licence may apply to signatories of the STM Permissions Guidelines, as amended from time to time.

Duration of Licence

A licence for is valid from the date of purchase ('Licence Date') at the end of the relevant period in the below table:

Scope of Licence	Duration of Licence
Post on a website	12 months
Presentations	12 months
Books and journals	Lifetime of the edition in the language purchased

Acknowledgement

The Licensor's permission must be acknowledged next to the Licenced Material in print. In electronic form, this acknowledgement must be visible at the same time as the figures/tables/illustrations or abstract, and must be hyperlinked to the journal/book's homepage. Our required acknowledgement format is in the Appendix below.

Restrictions on use

Use of the Licensed Material may be permitted for incidental promotional use and minor editing privileges e.g. minor adaptations of single figures, changes of format, colour and/or style where the adaptation is credited as set out in Appendix 1 below. Any other changes including but not limited to, cropping, adapting, omitting material that affect the meaning, intention or moral rights of the author are strictly prohibited.

You must not use any Licensed Material as part of any design or trademark.

Licensed Material may be used in Open Access Publications (OAP) before publication by Springer Nature, but any Licensed Material must be removed from OAP sites prior to final publication.

Ownership of Rights

Licensed Material remains the property of either Licensor or the relevant third party and any rights not explicitly granted herein are expressly reserved.

Warranty

IN NO EVENT SHALL LICENSOR BE LIABLE TO YOU OR ANY OTHER PARTY OR ANY OTHER PERSON OR FOR ANY SPECIAL, CONSEQUENTIAL, INCIDENTAL OR INDIRECT DAMAGES, HOWEVER CAUSED, ARISING OUT OF OR IN CONNECTION WITH THE DOWNLOADING, VIEWING OR USE OF THE MATERIALS REGARDLESS OF THE FORM OF ACTION, WHETHER FOR BREACH OF CONTRACT, BREACH OF WARRANTY, TORT, NEGLIGENCE, INFRINGEMENT OR OTHERWISE (INCLUDING, WITHOUT LIMITATION, DAMAGES BASED ON LOSS OF PROFITS, DATA, FILES, USE, BUSINESS OPPORTUNITY OR CLAIMS OF THIRD PARTIES), AND WHETHER OR NOT THE PARTY HAS BEEN ADVISED OF THE POSSIBILITY OF SUCH DAMAGES. THIS LIMITATION SHALL APPLY NOTWITHSTANDING ANY FAILURE OF ESSENTIAL PURPOSE OF ANY LIMITED REMEDY PROVIDED HEREIN.

Limitations

BOOKS ONLY: Where **'reuse in a dissertation/thesis'** has been selected the following terms apply: Print rights of the final author's accepted manuscript (for clarity, NOT the published version) for up to 100 copies, electronic rights for use only on a personal website or institutional repository as defined by the Sherpa guideline (www.sherpa.ac.uk/romeo/).

Termination and Cancellation

Licences will expire after the period shown in Clause 3 (above).

Licensee reserves the right to terminate the Licence in the event that payment is not received in full or if there has been a breach of this agreement by you.

Appendix 1 — Acknowledgements:

For Journal Content:

Reprinted by permission from [**the Licensor**]: [**Journal Publisher** (e.g. Nature/Springer/Palgrave)] [**JOURNAL NAME**] [**REFERENCE CITATION** (Article name, Author(s) Name), [**COPYRIGHT**] (year of publication)

For Advance Online Publication papers:

Reprinted by permission from [**the Licensor**]: [**Journal Publisher** (e.g. Nature/Springer/Palgrave)] [**JOURNAL NAME**] [**REFERENCE CITATION** (Article name, Author(s) Name), [**COPYRIGHT**] (year of publication), advance online publication, day month year (doi: 10.1038/sj.[JOURNAL ACRONYM].)

For Adaptations/Translations:

Adapted/Translated by permission from [**the Licensor**]: [**Journal Publisher** (e.g. Nature/Springer/Palgrave)] [**JOURNAL NAME**] [**REFERENCE CITATION** (Article name, Author(s) Name), [**COPYRIGHT**] (year of publication)

Note: For any republication from the British Journal of Cancer, the following credit line style applies:

Reprinted/adapted/translated by permission from [**the Licensor**]: on behalf of Cancer Research UK: : [**Journal Publisher** (e.g. Nature/Springer/Palgrave)] [**JOURNAL NAME**] [**REFERENCE CITATION** (Article name, Author(s) Name), [**COPYRIGHT**] (year of publication)

For Advance Online Publication papers:

Reprinted by permission from The [**the Licensor**]: on behalf of Cancer Research UK: [**Journal Publisher** (e.g. Nature/Springer/Palgrave)] [**JOURNAL NAME**] [**REFERENCE CITATION** (Article name, Author(s) Name), [**COPYRIGHT**] (year of publication), advance online publication, day month year (doi: 10.1038/sj.[JOURNAL ACRONYM])

For Book content:

Reprinted/adapted by permission from [**the Licensor**]: [**Book Publisher** (e.g. Palgrave Macmillan, Springer etc) [**Book Title**] by [**Book author**(s)] [**COPYRIGHT**] (year of publication)

Other Conditions:

CURRICULUM VITAE

PERSONAL INFORMATION

Surname, Name	: Güler, Baran
Nationality	: Turkish
Date and Place of Birth	: 1 January 1989, Ankara
Phone	: +90 505 703 94 93
E-mail	: barangulerr@gmail.com

EDUCATION

Degree	Institution	Year of Graduation
PHD	METU Metallurgical and Materials Eng.	2020
BS	METU Metallurgical and Materials Eng.	2012
High School	Gazi Anatolian High School, Ankara	2007

WORK EXPERIENCE

Year	Place	Enrollment
2019-Present	Roketsan A.Ş.	Specialist Engineer
2013-2019	METU, Metallurgical and Materials Eng.	Teaching Assistant

FOREIGN LANGUAGES

Fluent English, Beginner German

PUBLICATIONS

1. Seymen Y., Güler B. and Efe M. "Large Strain and Small-scale Biaxial Testing of Sheet Metals", Experimental Mechanics, 56, 1519-1530 (2016)

2. Güler B., Efe M. "Forming and Fracture Limits of Sheet Metals Deforming Without a Local Neck", Journal of Materials Processing Technology, 252, 477-484 (2018)

PROCEEDINGS

1. Güler B., Efe M. "Large strain cruciform biaxial testing for FLC detection", AIP Conference Proceedings, 1896, 020018 (2017)

2. Güler B., Alkan K. and Efe M. "Formability analysis of sheet metals by cruciform testing", IOP Conf. Series: Journal of Physics: Conf. Series, 896, 012003 (2017)

3. Güler B., Şimşek Ü., Yalçınkaya T. and Efe M. "Grain-scale investigations of deformation heterogeneities in aluminum alloys", AIP Conference Proceedings, 1960, 170005 (2018)

4. Güler B., Efe M. "Multi-scale characterization of deformation in aluminum", ASME 2018 13th Int. Manufacturing Science and Engineering Conference, Volume 2: Materials; Joint MSEC-NAMRC-Manufacturing USA MSEC2018-6574, V002T04A027 (2018)

HOBBIES

Theatre, Reading, Chess, Football, Basketball, Tennis